



AFRL-RB-WP-TR-2012-0169

**STRUCTURAL TECHNOLOGY EVALUATION ANALYSIS
PROGRAM (STEAP)**

**Task Order 0029: Thermal Stability of Fatigue Life-Enhanced
Structures**

**Vijay K. Vasudevan, Dong Qian, S.R. Mannava, Gokul Ramakrishnan, Vibhor Chaswal,
Amrinder Gill, Zhong Zhou, and Sagar Bhamare**

University of Cincinnati

**JANUARY 2012
Final Report**

Approved for public release; distribution unlimited.

See additional restrictions described on inside pages

STINFO COPY

**AIR FORCE RESEARCH LABORATORY
AIR VEHICLES DIRECTORATE
WRIGHT-PATTERSON AIR FORCE BASE, OH 45433-7542
AIR FORCE MATERIEL COMMAND
UNITED STATES AIR FORCE**

NOTICE AND SIGNATURE PAGE

Using Government drawings, specifications, or other data included in this document for any purpose other than Government procurement does not in any way obligate the U.S. Government. The fact that the Government formulated or supplied the drawings, specifications, or other data does not license the holder or any other person or corporation; or convey any rights or permission to manufacture, use, or sell any patented invention that may relate to them.

This report was cleared for public release by the USAF 88th Air Base Wing (88 ABW) Public Affairs Office (PAO) and is available to the general public, including foreign nationals. Copies may be obtained from the Defense Technical Information Center (DTIC) (<http://www.dtic.mil>).

AFRL-RB-WP-TR-2012-0169 HAS BEEN REVIEWED AND IS APPROVED FOR PUBLICATION IN ACCORDANCE WITH THE ASSIGNED DISTRIBUTION STATEMENT.

**//Signature//*

KRISTINA LANGER
Program Manager
Analytical Mechanics Branch
Structures Division

//Signature//

MICHAEL J. SHEPARD, Chief
Analytical Mechanics Branch
Structures Division

//Signature//

DAVID M. PRATT, Technical Advisor
Structures Division
Air Vehicles Directorate

This report is published in the interest of scientific and technical information exchange, and its publication does not constitute the Government's approval or disapproval of its ideas or findings.

*Disseminated copies will show “//Signature//” stamped or typed above the signature blocks.

REPORT DOCUMENTATION PAGE				<i>Form Approved</i> OMB No. 0704-0188	
<p>The public reporting burden for this collection of information is estimated to average 1 hour per response, including the time for reviewing instructions, searching existing data sources, gathering and maintaining the data needed, and completing and reviewing the collection of information. Send comments regarding this burden estimate or any other aspect of this collection of information, including suggestions for reducing this burden, to Department of Defense, Washington Headquarters Services, Directorate for Information Operations and Reports (0704-0188), 1215 Jefferson Davis Highway, Suite 1204, Arlington, VA 22202-4302. Respondents should be aware that notwithstanding any other provision of law, no person shall be subject to any penalty for failing to comply with a collection of information if it does not display a currently valid OMB control number. PLEASE DO NOT RETURN YOUR FORM TO THE ABOVE ADDRESS.</p>					
1. REPORT DATE (DD-MM-YY) January 2012		2. REPORT TYPE Final		3. DATES COVERED (From - To) 27 August 2008 – 31 January 2012	
4. TITLE AND SUBTITLE STRUCTURAL TECHNOLOGY EVALUATION ANALYSIS PROGRAM (STEAP) Task Order 0029: Thermal Stability of Fatigue Life-Enhanced Structures				5a. CONTRACT NUMBER FA8650-04-D-3446-0029	
				5b. GRANT NUMBER	
				5c. PROGRAM ELEMENT NUMBER 62201F	
6. AUTHOR(S) Vijay K. Vasudevan, Dong Qian, S.R. Mannava, Gokul Ramakrishnan, Vibhor Chaswal, Amrinder Gill, Zhong Zhou, and Sagar Bhamare				5d. PROJECT NUMBER 2401	
				5e. TASK NUMBER	
				5f. WORK UNIT NUMBER AOFIOB	
7. PERFORMING ORGANIZATION NAME(S) AND ADDRESS(ES) By: University of Cincinnati College of Engineering and Applied Science 501ERC, P.O. Box 210012 Cincinnati, OH 45221-0012				For: General Dynamics Information 5100 Springfield Pike, Suite 509 Dayton, OH 45431	
9. SPONSORING/MONITORING AGENCY NAME(S) AND ADDRESS(ES) Air Force Research Laboratory Air Vehicles Directorate Wright-Patterson Air Force Base, OH 45433-7542 Air Force Materiel Command United States Air Force				8. PERFORMING ORGANIZATION REPORT NUMBER	
				10. SPONSORING/MONITORING AGENCY ACRONYM(S) AFRL/RBSM	
				11. SPONSORING/MONITORING AGENCY REPORT NUMBER(S) AFRL-RB-WP-TR-2012-0169	
12. DISTRIBUTION/AVAILABILITY STATEMENT Approved for public release; distribution unlimited.					
13. SUPPLEMENTARY NOTES PAO Case Number: 88ABW-2012-2314; Clearance Date: 17 Apr 2012. Report contains color.					
14. ABSTRACT This work combines process parameter variations, finite element (FE) modeling and simulations, characterization, and mechanical testing in a study of the effects of laser shock peening (LSP) on residual stress and microstructure evolution, thermal stability thereof, and fatigue behavior of high-temperature aerospace structural alloys (Ti-64, Ti-6242, IN718 SPF and IN718 Plus). The aim was to secure a quantified knowledge of the impact of process parameters and high-temperature exposures on the stability of residual stress, microstructure, and fatigue properties in laser peened high-temperature structural alloys. The results show that LSP induces deep compressive residual stresses and near-surface plasticity and hardening that are quite stable to relatively high temperatures specific for each alloy. Good agreement between experimental and FE simulation results for LSP-induced residual stress and thermal relaxation behavior was obtained. The various project results have shown that advanced surface treatments, such as LSP, can be effective for enhancing the fatigue life and the thermal stability of fatigue life in high-temperature aerospace structural alloys.					
15. SUBJECT TERMS laser shock peening, finite element, residual stress, microstructure, fatigue, thermal relaxation, microscopy					
16. SECURITY CLASSIFICATION OF:			17. LIMITATION OF ABSTRACT: SAR	18. NUMBER OF PAGES 112	19a. NAME OF RESPONSIBLE PERSON (Monitor) Kristina Langer 19b. TELEPHONE NUMBER (Include Area Code) N/A
a. REPORT Unclassified	b. ABSTRACT Unclassified	c. THIS PAGE Unclassified			

TABLE OF CONTENTS

Section	Page
SUMMARY	1
1.0 INTRODUCTION	2
2.0 METHODS, ASSUMPTIONS AND PROCEDURES	5
2.1 Materials and Processing.....	5
2.2 Laser Shock Peening	6
2.3 Microhardness and Nano-/Microindentation Measurements	6
2.4 Residual Stress Analysis	7
2.5 Thermal Stability Analysis	9
2.6 Static, Fatigue and Fatigue Crack Growth Testing.....	10
2.7 Microstructure and Fracture Characterization	11
2.8 Modeling and Simulation.....	12
3.0 RESULTS AND DISCUSSION.....	13
3.1 Experimental and Finite Element Modeling and Simulation of LSP-Induced Residual Stresses and Thermal Relaxation in IN718 SPF, Ti64 and Ti6242 Alloys.....	13
3.1.1 Experimental Results of Residual Stress and Thermal Relaxation	14
3.1.2 Finite Element Simulation Results of Residual Stress and Thermal Relaxation.....	30
3.2 LSP Process Simulations for Optimizing LSP Treatment and Effects on Fatigue Behavior of Ti6242 Alloy.....	40
3.2.1 Initial LSP Treatments and Three-Point Bend Fatigue Tests.....	40
3.2.2 Rationale for LSP Process Simulations for Optimizing LSP Treatment.....	42
3.2.3 LSP Modeling and Simulation Procedure	43
3.2.4 Simulation Results and Discussion.....	46
3.2.5 Static Tests and Properties	51
3.2.6 Fatigue Tests and Behavior	54
3.2.7 Fractography of Failed Fatigue Specimens and Fatigue Crack Growth.....	56
3.3 Results of LSP Effects on Residual Stress, Microstructure, Thermal Relaxation and Fatigue Behavior of IN718 Plus Alloy	60
3.3.1 Thermal Aging Effects on Precipitation Behavior	60
3.3.2 LSP Effects on Residual Stress and Thermal Relaxation.....	74
3.3.3 Mechanical Properties of Unpeened Alloy	80
3.3.4 LSP Effects on Fatigue Behavior	83
4.0 CONCLUSIONS.....	89
5.0 REFERENCES	92

LIST OF FIGURES

Figure		Page
1	An Illustration of the LSP Process	3
2	Photograph of the GEN I System at UC Used for the LSP Treatment of Test Coupons	6
3	Basic Principle of the Sin2 ψ XRD Method for Determination of Residual Stress: (a) Definition of the Coordinate System and the Angles ψ , ϕ and (b) Strain vs. the Sin2 ψ Plot (Stress is Obtained From the Slope of the Regression Fit and the X-Ray Elastic Constants)	8
4	Photographs of the (a) MTS 810 and (b) MTS 1000 Bionix Systems Used for the Static, Fatigue and Fatigue Crack Growth Tests	10
5	Photographs of the (a) Typical Test Samples and (b) ACPD System for Crack Length Measurements	11
6	Representative (a) OM and (b) OIM Micrographs of Microstructure of As-Received IN718 SPF Alloy	14
7	(a) Diffraction Peak FWHM and (b) Residual Stress vs. Depth From Peened Surface in IN718 SPF Coupons for Two Different Power Densities	17
8	(a) Residual Stress and (b) Diffraction Peak FWHM vs. Depth From Peened Surface of 9 GW/CM ² IN718 SPF Sample	18
9	(a) Residual Stress and (b) Diffraction Peak FWHM vs. Depth From Peened Surface of 16 GW/cm ² IN718 SPF Sample	19
10	(a) Residual Stress and (b) Diffraction Peak FWHM as Function of Depth for Various Aging Treatments in a Single Dimple LSP-Treated IN718 SPF Sample	20
11	Schematic of Determination of Thermal Relaxation Kinetic and Thermodynamic Parameters in the Avrami Approach (From Ref. [40])	21
12	Surface Residual Stress as a Function of Exposure Time for Different Temperatures LSP-Treated IN718 SPF SET 3 Samples	21
13	Plots of (a) $\log \ln(\sigma^{rs} / \sigma_0^{rs})$ vs. $\log t_a$ and (b) $\log t_a$ Corresponding to Specific Levels of Stress Relaxation vs. $1/kTa$ for Determination of the Activation Energy Associated with the Relaxation Process in the IN718 SPF Alloy	23
14	Representative (a) SE, (b) BSE Micrographs of Microstructure of As-received Ti6242 Alloy and (c), (d) SE Micrographs of As-Received Ti64 Alloy	24
15	Schematic Showing the Geometry and Dimensions, LSP Patch and Energy Conditions for the Ti6242 Coupons for (a) Establishing Base-Line Process Parameter Effects on Residual Stress and (b) Thermal Relaxation Studies	25
16	(a, c) Residual Stress and (b, d) Diffraction Peak FWHM in the X and Y Directions vs. Distance From Peened Surface of 8J, 8J (2 Hits) and 16 J Beam Energy LSP-treated Ti6242 Samples	27
17	Vickers Hardness of Unpeened, LSP-Treated and LSP-Treated + Thermally Aged (315, 482, 538°C) Ti6242 Samples	28
18	(a, c) Residual Stress and (b, d) Diffraction Peak FWHM in X and Y Directions vs. Distance from Peened Surface of 8J Beam Energy LSP-Treated Ti6242 Samples Aged at Different Temperatures (315, 482, 538°C) for Various Times	29
19	Plots of (a) $\log \ln(/)$ vs. $\log t$ and (b) $\log t$ Corresponding to Specific Levels of Stress Relaxation vs. $1/kTa$ for Determination of the Activation Energy Associated with the Relaxation Process in the Ti6242 Alloy	29

20	Flow Chart for LSP and Thermal Relaxation FE Simulations	30
21	Intensity and Pressure Temporal Profiles Calculated from Pressure Model	32
22	FE Mesh for LSP and Thermal Relaxation Simulation of IN718 and Ti-6Al-4V. during Thermal Relaxation Simulation, Thermal Loading Condition Was Applied at All Exposed Surfaces	33
23	As-Peened Residual Stress Comparison in IN718 SPF Alloy Single-Dimple Three-Shots Coupon	33
24	Comparison Between Experiment Data and Simulation Results of Thermal Relaxation of Residual Stress in LSP-Treated IN718 SPF	34
25	FE Simulation of Thermal Relaxation of Residual Stress in LSP-Treated IN718 SPF Alloy at (a) 600°C and (b) 650°C	34
26	As-Peened Residual Stress Comparison Ti64 Alloy Single-Dimple Three-Shots Coupon	35
27	Thermal Relaxation of Residual Stress Comparison in Ti64 Alloy Single-Dimple Three-Shots Coupon at (a) 315°C, (b) 400°C and (c) 450°C	36
28	Relaxed Residual Stress (at Surface, 100µm, and 200µm) at Different Beating Temperatures in Ti-6Al-4V	38
29	Simulation Results Showing Effect of Temperature and Time on Residual Stress Relaxation in LSP-Treated Ti-6Al-4V	38
30	FE Mesh for Simulation of LSP and Thermal Relaxation in the Ti6242 Alloy Coupons	39
31	Comparison of Experimental and FE Simulation Results of Thermal Relaxation of Residual in LSP-Treated Ti6242 Alloy at (a) 482C and (b) 538C	40
32	Geometry and Dimensions of Third Set of 3PB Test Coupons (2mm Thick) for Studying the Effects of LSP on the Fatigue Properties	41
33	Geometry and Dimensions of the Initial Sets of 3PB Test Coupons for Studying the Effects of LSP on the Fatigue Properties. Note: Coupon Has a 10mm X 10mm LSP-Treated Area in the Middle of the Bottom/Tensile Surface	41
34	Schematic of the Ti6242 Coupon Used for the LSP Simulations	43
35	Part of the Complete Mesh for the Ti6242 Coupon	44
36	Flowchart of LSP Simulation Procedure	44
37	Temporal Profile of the Pressure Pulse Generated Using the Pressure Model	45
38	LSP Spot Sequence for 12mm x 10mm Patch in Ti6242 Coupon	46
39	Contour Plot of the Axial Stresses. Note Build-Up of Tensile Residual Stresses Along the Edges of the Thin Ti6242 Coupon	47
40	Residual Stress Profiles Obtained From LSP Simulation of 12mm x 10mm Patch in Ti6242 Coupon	48
41	Spot Sequence I for 8mm x 5mm Patch in Ti6242 Coupon	49
42	Residual Stress Profiles Obtained From LSP Simulation of 8mm x 5mm Patch	49
43	Spot Sequence II for 8mm x 5mm Patch in Ti6242 Coupon	50
44	Residual Stress Profiles Obtained from LSP Simulation of 8 mm x 5 mm Patch With Modified Sequence and Laser Parameters of 2 J, 27 ns, 2 mm Spot Size	51
45	Residual Stress Profiles Obtained From LSP Simulation of 8 mm x 5mm Patch With Modified Sequence and Laser Parameters 3 J, 27 ns, 2 mm Spot Size	51
46	Load Versus Strain Data Recorded During a Tensile Test on As-Received Ti6242 Alloy Coupon	52

47	Photographs of the 3PB Static and Fatigue Test 60mm Long x 10mm Wide x 2mm Thick Showing the LSP-Treated Area and Details of the Notch	53
48	Load Versus Displacement Data Recorded During a Static 3PB Test on Unpeened and LSP-Treated Notched 60mm x 10mm x 2mm Thick Ti6242 Coupon	53
49	Plot of Applied Maximum Bending Stress Versus Number of Cycles to Failure From 3PB Fatigue Test on Unpeened, LSP-Treated and LSP-Treated + 482°C, 24b-Aged Ti6242 Alloy Coupons	56
50	SEM Micrographs Recorded From the Fracture Surface of a Fatigue Tested Unpeened Ti6242 Specimens at a Distance of (a) ~2mm and (b) ~4mm From the Notch Tip Showing Striations Characteristic of Stage II Fatigue Crack Growth	57
51	SEM Micrographs Recorded From the Fracture Surface of a Fatigue Tested LSP-Treated Ti6242 Specimens at a Distance of (a) ~2mm and (b) ~4mm From the Notch Tip Showing Striations Characteristic of Stage II Fatigue Crack Growth	58
52	SEM Micrographs Recorded From the Fracture Surface of a Fatigue Tested LSP-Treated +482C, 24 b-Aged Ti6242 Specimens at a Distance of (a) ~2mm and (b) ~4mm From the Notch Tip Showing Striations Characteristic of Stage II Fatigue Crack Growth	58
53	Plot of Crack Growth Rate, da/dN Versus Applied Stress Intensity Range, ΔK , Based on Measurement of Striation Spacings on Fracture Surfaces and Calculations for Unpeened, LSP-Treated and LSP-Treated +482°C, 24 b-Aged Ti6242 Alloy Coupons	59
54	TTT Curve of δ Phase Precipitation in IN718 Plus [75]	61
55	Microstructure of As-Received IN718 Plus Alloy: (a) OM, (b) EBSD/OIM Map and, (c) Grain Mis-orientation Map	61
56	Vickers and Knoop Hardness Evolution of IN718+ With Aging Time at Different Temperatures	62
57	TEM Micrographs Showing the Microstructure of As-Received IN718+ Alloy. a) BF Micrograph Showing η -Ni ₃ Ti Precipitates b) SAD Pattern Recorded From Region Containing γ Matrix and η and c) BF Micrograph Showing δ -Ni ₃ Nb Precipitates	63
58	Microstructure of IN718+ Alloy Aged at 650°C, 250 b (a) DF TEM Micrograph Showing Ultrafine (5-10 nm) γ Precipitates (Inset [001] SAD Pattern) and b) BF Micrograph Showing η -Ni ₃ Ti Precipitates	63
59	DF TEM Micrographs Recorded From IN718+ Alloy Aged at (a) 800C, 1000b, (b) 850°C, 15b and (c) 850°C, 200b Showing γ Precipitates	64
60	DF TEM Micrographs Recorded From IN718+ Alloy Aged at 750°C for (a) 250b (inset [011] γ // [011] γ' // [11-20] η -Ni ₃ Ti SAD Pattern) and (b) 500 b Showing γ' Precipitates Containing Faults, as Well as η -Ni ₃ Ti Plates Cutting Through the γ' (in "a")	64
61	DF TEM Micrographs Recorded From IN718+ Alloy Aged at 700°C for (a) 250b and (b) 500b Showing γ' Precipitates Insets [001] SAD Pattern	65
62	(a,c) Experimental and (b,d) Computer Simulated SAD Patterns Confirming the Plate-Shaped η -Ni ₃ Ti Precipitates. (a,b) [011] γ // [11-20] η and (c,d) [111] γ' // [0001] η	66
63	Manual Tracing for ' Size Measurement'	68
64	Maximum Entropy Thresholding For γ' Size Measurement	69
65	Difference in particle counting due to overlap between raw and corrected images for the same set of particles: (a) Overlapped and (b) separated	71

66	Variation of Cube of Diameter of γ' Precipitates With Aging Temperature and Time and (b) Plot of $\ln K$ Versus $1/T$ for Determining the Activation Energy for Coarsening	72
67	TTT Diagram for γ' Precipitation in IN718 by [75] With Simulated (solid) and Experimental (Dashed) Line	72
68	Plot $\ln K$ vs. $1/T$ for Determining Activation Energy for γ' as Per Ardell's [82] Square Law Formulation	74
69	(a) LSP Specimen Dimensions, Geometry and Experimental Setup and (b) Information Relating to Analysis of In-Plane and Out-Of-Plane Strains in the Peened Samples From the Diffraction Pattern	74
70	Plots of Diffraction Strain Versus Asimuth (a) as LSP-Treated In718 Plus and (b) LSP-Treated + Aged 700°C, 1b/750°C, 1b	76
71	In-Plane Residual Strains as a Function of Distance From the Surface of In718 Plus Alloy (a) As LSP-Treated and (b) LSP-Treated + AGed700C, 1b/750C, 1b	77
72	In-Plane Residual Strains as a Function of Distance Across the LSP-Treated Surface of IN718 Plus Alloy Before and After Aging	78
73	In-Plane Residual Strains as a Function of Distance From the Surface of IN718 Plus Alloy (a) As LSP-Treated and (b) LSP-Treated + AGed 700C, 1b/750C, 1b	79
74	Hardness Across LSP-Treated Surface of IN718 Plus Alloy Before and After Aging	80
75	Tensile Stress-Strain Curve for As-Received + Standard Aged IN718 Plus Alloy	81
76	3PB Compression Stress-Strain Curve for As-Received + Standard Aged IN718 Plus Alloy	82
77	3PB Fatigue S-N Curve for As-Received + Standard Aged IN718 Plus Alloy	82
78	Optical Micrographs of Transgranular Fatigue Crack Growth in IN718 Plus (a) One Surface, (b) Opposite Surface, (c) Montage	83
79	Crack Deflection During Fatigue Crack Growth Upon Entering the LSP-Treated Single Dimple (center) in IN718 Plus (a) Side 1 and (b) Side 2 Surface of Test Coupon	84
80	3-D Profile of Crack Tip in LSP-Treated IN718 Plus	84
81	Fatigue Crack Growth Data for Non-LSP-Treated IN718+ Alloy. (a,b) COD Data, (c) Crack Length vs. Number of Cycles From ACPD Measurements and (d) da/dN vs. ΔK Curve From ACOD Data	85
82	Fatigue Crack Growth Data for LSP-Treated IN718+ Alloy (a,b) Crack Length and Crack Growth Rate vs. Number of Cycles From ACPD Measurements, (c) COD vs. Load and (d) da/dN vs. ΔK Curve From ACPD Data	86
83	(a) Low Magnification and (b) High Magnification SEM Micrographs of Fracture Surface of Failed LSP-Treated FCG Sample. Note Transition Band as the Crack Enters the LSP-Treated Region	87
84	Tensile Fatigue S-N Curve for Unpeened and LSP-Treated IN718 Plus Alloys at Room Temperature and at 650°C	88

LIST OF TABLES

Table		Page
1	Nominal Chemical Compositions (in Wt.%) of Ti6242 and Ti64 Alloys	5
2	Chemical Compositions (in Wt.%) of IN718 SPF and IN718 Plus Alloys	5
3	Details of Experimental Conventional XRD Measurements of Residual Stress in LSP-Treated IN718 SPF Alloy	15
4	Details of Experimental Conventional XRD Measurements of Residual Stress in LSP-Treated Ti6242 and Ti64 Alloys	26
5	Results of 3PB Fatigue Tests on Unpeened, LSP-Treated and LSP-Treated = Aged Ti6242 Alloy Coupons	55
6	Activation energy for γ' coarsening from present study compared with Literature [78]	73
7	Residual Stress Versus Depth in LSP-treated IN718 Plus Before and After Aging	80

ACKNOWLEDGMENTS

Financial support for this research from the Air Force Research Laboratory (AFRL) and General Dynamics Information Technology (GDIT) under contract # FA-8650-04-D-3446, Sub-contract # USAF-34446-29-SC-001, Task Order #29, with program monitor Mr. Kevin Hunt (GDIT) and technical monitor Dr. Kristina Langer (AFRL/RBSM), is deeply appreciated. The authors also wish to thank Dr. Michael Shepard (AFRL/RBSM) for many helpful discussions, attendance of review meetings and encouragement during the course of this work. The authors are grateful to Dr. Erin T. McDevitt from Allvac for providing the IN718 Plus alloy material for this project, as well as to Mr. Curtis Fox (UC) for his help with setting-up the ACPD system for fatigue crack growth monitoring. The authors also wish to thank Drs. Mike Uchic, Dennis Dimiduk and Allan Smith from the AFRL Materials and Manufacturing Directorate for their help with the micropillar compression testing. The help from Dr. Yang Ren from the Advanced Photon Source at the Argonne National Laboratory in the synchrotron x-ray diffraction work is deeply appreciated. We would also like to deeply thank the Ohio Department of Development Third Frontier Program for funding the *Ohio Center for Laser Shock Processing for Advanced Materials and Devices* at the University of Cincinnati (UC), which provided state-of-the-art characterization and testing equipment that was instrumental for performing the work in the present project. Finally, we would like to thank the Advanced Materials Characterization Center at the UC for providing the necessary facilities for materials characterization.

SUMMARY

The present work combines process parameter variations, finite element (FE) modeling and simulations, characterization, and mechanical testing in a study of the effects of laser shock peening (LSP) on residual stress and microstructure evolution, thermal stability thereof, and fatigue behavior of high-temperature aerospace structural alloys (Ti-6Al-4V, Ti-6Al-2Sn-4Zr-2Mo, IN718 SPF and IN718 Plus). The aim was to secure a quantified knowledge of the impact of process parameters and high-temperature exposures on the stability of residual stress, microstructure, and fatigue properties in laser peened high-temperature structural alloys. The results show that LSP induces deep compressive residual stresses and near-surface plasticity and hardening that are quite stable to relatively high temperatures specific for each alloy. Good agreement between experimental and FE simulation results for LSP-induced residual stress and thermal relaxation behavior was obtained. Through analytical modeling of the kinetics of thermal relaxation of residual stress, good agreement was obtained (in the activation enthalpy determined both experimentally and by simulation with reported literature values) for self or solute diffusion in each of the sets of alloys. FE simulations were successfully used to develop optimum LSP processing conditions for three-point bend and axial fatigue testing of coupons. The results indicated that optimally configured LSP enhances fatigue behaviors in both the Ti6242 and IN718 Plus alloys. This improvement was partially retained even after thermal exposure of the LSP-treated coupons to high temperatures characteristic of expected service temperatures for the alloys. The stress intensity range required to achieve a particular fatigue crack growth rate was higher after LSP treatment when compared with the unpeened condition, pointing to the beneficial effects of LSP in improving ambient and high-temperature fatigue properties. The various project results have shown that advanced surface treatments, such as LSP, can be effective for enhancing the fatigue life and the thermal stability of fatigue life in high-temperature aerospace structural alloys.

1.0 INTRODUCTION

There is a continuing demand for improved high-temperature engineering materials and processes for applications in advanced aerospace structures and other transportation systems. It has become increasingly clear that while the development of new, higher temperature alloys is desirable, significant near-term progress in increasing aircraft performance for increased efficiency and power generation is more likely to come from the development of new processes to enhance the properties and resistance to damage of current materials during typical operating conditions than from the design of new alloys. In this context, development of new surface engineering processes is one of the critical pacing technologies [1].

Several surface enhancement processes such as shot peening (SP), laser shock peening (LSP) [2-4] and low plasticity burnishing (LPB) [5-7] are used in industry to enhance the fatigue strength of manufactured components under service operating conditions. The primary purpose of these processes is to introduce compressive residual stresses which mitigate any tensile stresses resulting from component design or operating service conditions. Even though these processes generate compressive residual stresses, the intensity and depth of the compression, the associated cold work, surface roughness, microstructure, and temperature-induced relaxation effects differ greatly for each set of process parameters. Thus, each process has its advantages and disadvantages for a given application.

Shot peening is a well-established process [1] and is used to benchmark the capabilities of other, newly-emerging technologies such as LSP [2-4] and LPB [5]. While the shot peening process imparts high magnitude compressive stresses on the surface of a component, the depth of compression is usually restricted to about 75-250 μm , depending upon the peening intensity. Furthermore, SP can also introduce severe surface damage/roughness and large amounts of cold work. As a consequence, residual stresses can become unstable and most of the process-induced compressive stresses are lost quickly at elevated temperatures [1], thereby limiting the use of this method for high-temperature applications.

The shortcomings associated with SP have led to the development of advanced mechanical surface treatment technologies such as LSP [2-4] and LPB [5-7] to enhance the service lives of critical metal parts, ranging from aircraft engine fan and compressor blades and structures fabricated from Ti and Ni-base alloys to human hip joints to golf clubs. The LSP technology, which was first introduced by Battelle Laboratories and Wagner Laser Technologies in the 1970s [8-12], is beginning to be used extensively by the major aero engine companies (General Electric, Pratt & Whitney and Rolls-Royce) to enhance the fatigue properties of fan and compressor blades in Foreign Object Damage (FOD) environments. Indeed, studies to date have revealed that LSP leads to a dramatic improvement in the fatigue strength, life, and resistance to crack propagation in materials and parts [2,3,12-17]. The LPB process, which was patented and developed by Lambda Research [5] and is based on the principal of roller and ball burnishing used originally for refinement of surface finishes, has similar effects on enhancing the fatigue properties and corrosion resistance of a variety of materials [5-7].

In the LSP process (Figure 1), an absorbing opaque tape or black paint ablative layer is first applied to the sample or part surface over which a layer of water is passed. Upon incidence of the high energy pulsed laser, the tape material vaporizes and the explosively expanding plasma that is created is confined by the water layer, generating powerful shock waves that propagate into the substrate. The intensity of the resulting pressure pulse on the surface of the sample, which lasts < 50 ns and can approach up to 10 GPa, leads to plastic deformation at the surface and to a depth at which the peak pressure no longer exceeds the metal's Hugoniot elastic limit (HEL). The HEL is

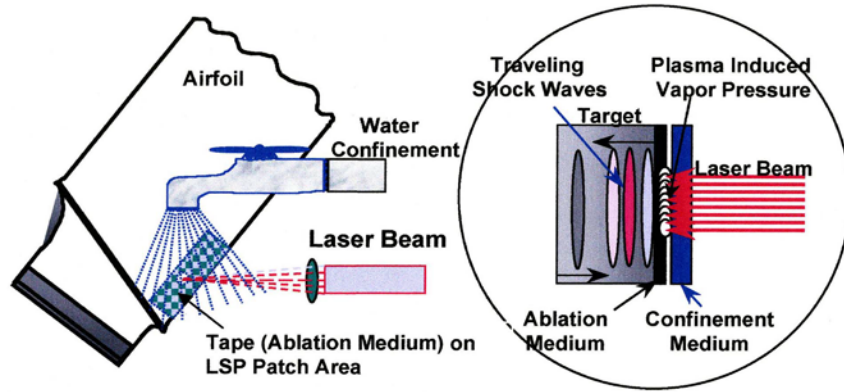


Figure 1: An Illustration of the LSP Process

related to the dynamic yield strength at high strain rates, σ_y^{dyn} and Poisson's' ratio, ν , according to [18]:

$$HEL = \frac{1 - \nu}{1 - 2\nu} \sigma_y^{dyn} \quad (1)$$

Associated with these plastic deformations is the production of a deep compressive residual stress layer extending from the surface to depths of up to 2 mm, depending on the energy density and material.

Typical application of the LSP process utilizes a pulsed Nd:Glass laser ($\lambda = 1.07 \mu\text{m}$) providing energy in the range of 1 to 100 J per pulse with pulse durations ranging from 5-50 ns. The key to success of LSP is to confine the plasma generated when the laser beam interacts with the materials surface, against the surface, which, in turn, has the effect of increasing the pressure developed by the plasma on the surface up to ten times over that developed when the plasma is unconfined. A recent trend in the industry is to utilize lower power Nd: glass lasers operating at higher frequencies, but since these lasers operate at <10 J per pulse, the spot sizes are much smaller [17, 19, 20]. The laser beam can be directed either to one side of the component or simultaneously to the same location on two opposite sides (double-sided processing) of the component. The latter is the preferred practice for thin sections to minimize distortion and avoid bulging.

A number of process variables, including laser shock intensity (energy/power density or fluence), spot size, multiple laser shots, overlapping of laser spots, etc., are available to control the depth of residual stress, surface roughness and distortion, and many studies of the influence of these parameters have been conducted [2-4,17]. The intensity of LSP is primarily controlled by the power density (power per unit area) applied to the laser peened spot, and increasing this quantity increases both the magnitude and depth of the compressive residual stresses. The depth of compression can also be increased at a given energy by applying multiple impacts to the same location [2-4, 17].

There is evidence that shows that improvements in fatigue life through LSP are brought about by the shock wave-induced generation of deep compressive residual stresses in the material extending from the surface to the interior [2-4, 8, 9]. The increased compressive depth effectively improves the fatigue life by a factor of three to five times over that provided by conventional peening treatments. In fact, tests on deliberately nicked (and hence weakened) Ti and Ni fan and compressor blades show that LSP will actually render these parts stronger than new, unflawed—but not laser-peened—blades, which points to improved resistance to FOD. Indeed, LSP has also been used to negate the high mean stresses of blisks, to restore design margins for vibration, and to

enhance erosion, corrosion and fretting properties of rotating components [17]. In addition, there are indications that creep performance at elevated temperatures may also be enhanced.

While the LSP and LPB technologies have been applied with great success to fan and compressor blades operating at ambient/low temperatures, there is a growing realization that the properties and performance of other aircraft parts such as rotors, disks, gears and shafts, as well as those operating at elevated temperatures, could also be improved appreciably. Work to date indicates that unlike shot peening, both LSP and LPB generate deep compressive stresses with relatively low cold work [2-7] and there is also evidence showing that these compressive stresses and microstructure stability could be retained even after high temperature exposure [6,14], accompanied by improved fatigue behavior. If a comprehensive understanding can be established of the thermal stability of the residual stresses, microstructures, and fatigue properties over a wider range of process conditions and temperatures through fundamental research, the use of processes like LSP and LPB could be extended to high-temperature alloys typically used in hot sections of aerospace structures, including exhaust-washed components and hypersonic platforms. The benefits derived from such applications could be enormous, including extension of the service lifetimes of critical parts operating at high temperatures and potentially billions of dollars of savings to the aerospace industry. However, several basic questions must be answered before the application of these advanced surface treatment processes to high temperature parts can emerge from the realm of theory to the reality of practical application and, consequently, considerable fundamental research and development (R&D) will be required to develop these processes for high-temperature materials applications and study the related effects on materials behavior to optimize both process and materials performance.

The goal of the proposed research program, which was conducted in close collaboration with the Air Force Research Laboratory (AFRL), was to develop a fundamental understanding of the thermal relaxation behavior of residual stresses and material structures at micro- and nano-scales and fatigue in high-temperature structural alloys induced by advanced mechanical surface treatments, via process development, residual stress measurements, microstructural analysis, thermomechanical relaxation behavior, fatigue tests, and multiscale modeling and simulation. The LSP process was chosen for the study, as UC has the required equipment for the work as well as access to the LSP equipment at General Electric Aircraft Engines (GEAC) and LSP Technologies (LSPT) and, furthermore, the results will be applicable to other emerging technologies like LPB [5-7], which also produces deep compressive residual stresses with relatively less cold work and displays similar thermal response. Specifically, the project involved the following: (1) development of the LSP process for selected Ti and Ni-base alloys that experience high temperatures in aerospace structures; (2) measurement and mapping of surface and sub-surface macro and micro residual strains/stresses and microstructural changes as a function of LSP process parameters using novel methods; (3) determination of thermal relaxation of residual stresses (macro and micro), microstructure evolution with time at elevated temperatures typical of turbine engine operating conditions, and modeling of the kinetics of relaxation; (4) evaluation of the effects of residual stress, near surface microstructure, and temperature on fatigue properties and mechanisms of fatigue crack nucleation and growth; and (5) development of a robust modeling and simulation approach for determining the effects of LSP on residual stress, microstructure evolution, thermal stability, and fatigue life.

2.0 METHODS, ASSUMPTIONS AND PROCEDURES

2.1 Materials and Processing

The materials studied in this project included the Ti-base alloys Ti-6Al-2Sn-4Zr-2Mo (Ti6242) and Ti-6Al-4V (Ti64) and the nickel-base superalloys IN718 SPF (super-plastically formed) and IN718 Plus. The Ti6242 material was obtained from AFRL/RBSM (Dr. Kristina Langer) in the form of an L-shaped plate approximately 300 mm long x 125 mm wide x 4.3 mm thick. The Ti64 coupons were obtained from GE Aviation in the form of coupons 35 mm² square x 2 mm thick. Both the Ti6242 and Ti64 alloys were in the mill annealed condition and their nominal compositions are given in Table 1. The IN718 SPF material was obtained from Special Metals in the form of a hot-rolled and then solution annealed sheet having dimensions of 300 mm x 300 mm x 2 mm thick. Coupons cut from the sheet were aged at 750°C for 5h. The IN718 Plus material was obtained from ATI Allvac in the form of 250 mm x 250 mm square sheets of various thicknesses, namely 1.875 mm, 5 mm and 12.5 mm. These plates had been hot-rolled and then heat-treated at 953°C for 0.5h followed by air-cooling. The chemical compositions of IN718 SPF and the IN718 Plus alloys are given in Table 2.

Table 1. Nominal Chemical Compositions (in Wt.%) of Ti6242 and Ti64 Alloys

Alloy	Ti	Al	V	Sn	Zr	Mo	O	Si
Ti6242	Bal	6.0	-	2.0	4.0	2.0	0.1	0.1
Ti64	Bal	6.0	4.0	-	-	-	0.1	-

Table 2. Chemical Compositions (in Wt.%) of IN718 SPF and IN718 Plus Alloys

Alloy	Ni	Cr	Co	Fe	Al	Ti	Nb	Mo	W	C	P	B
IN718 SPF	Bal	17.90	0.16	18.8	0.49	1.01	5.22	2.86	0.03	0.025	0.008	0.004
IN718 Plus	Bal	17.42	9.13	9.66	1.46	0.71	5.48	2.72	1.04	0.028	0.013	0.005

2.2 Laser Shock Peening

The LSP treatments of the test coupons were largely conducted using the Gen I system (Nd-doped glass) at UC shown in Figure 2, with tape as the ablative medium and water as the confining medium. Laser beam energies ranged from 2 to 8 J with a pulse width of 25-30 ns and rise time of 3-5 ns. Beam energy measurements were calibrated using a Scientech laser calorimeter. Pulse

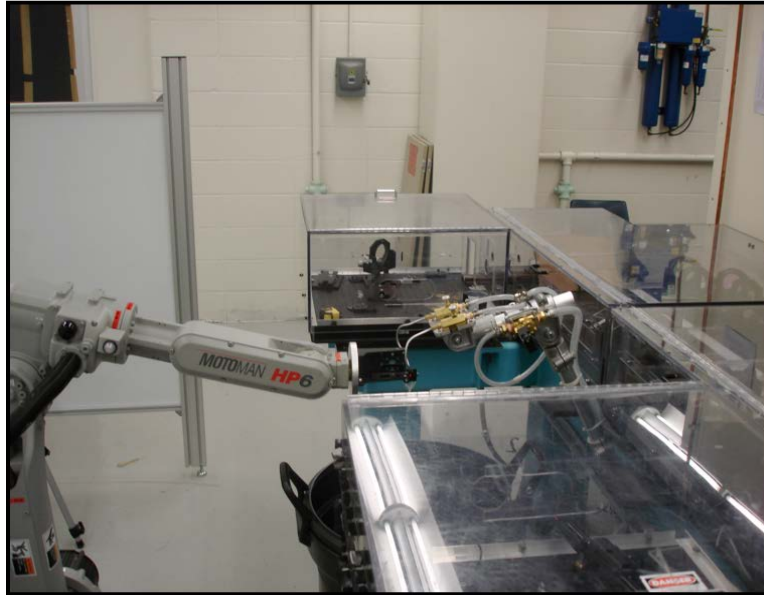


Figure 2: Photograph of the GEN I System at UC Used for the LSP Treatment of Test Coupons

waveforms were acquired using a Tektronix TDS640, 2 Ghz oscilloscope and the output data for each shot was stored on a computer interfaced to the oscilloscope for later use. An LSP spot diameter of 2 mm was used, which gave a range of power densities from 5 to 16 GW/cm². Prior to the LSP treatment, the test coupons were polished to a mirror finish, using colloidal silica in the final step. A series of LSP treatments involving single dimple, as well as overlapped patterns with single/multiple impacts, coupled with experimental measurements and finite element (FEM) simulations of the LSP residual stresses were conducted to arrive at appropriate conditions to use for the coupons for studying the thermal relaxation and fatigue behavior. The topography and geometrical features of single and overlapped LSP-generated dimples were studied using a Veeco optical scanning probe. Some coupons of the IN718 plus alloy were also LSP-treated using the facilities at LSP Technologies (Dublin, OH). Details of the coupon geometries, dimensions and LSP treatment are provided in the Results and Discussion section pertaining to each alloy.

2.3 Microhardness and Nano-/Microindentation Measurements

To evaluate property changes due to LSP and thermal treatments, microhardness testing using both Vickers and Knoop indenters were conducted using a Leco tester. For the Vickers hardness tests, a load of 0.5-1 kg and a hold time of 15s was used, whereas for the Knoop hardness tests a load of 50 g and hold time of 15s was used. Measurements were made at particular distances from the peened surface and repeated along different rows and the average at each distance was computed. In addition, nano- and micro-indentation tests were conducted using a CSM Instruments

Model NHT device. Both load-controlled and depth-controlled modes were used and arrays of measurements were made inside and outside the peened areas. The load-displacement curves were analyzed using the instrument software to determine the hardness and modulus.

2.4 Residual Stress Analysis

Both conventional (CXRD) and high-energy synchrotron (SXRD) x-ray diffraction techniques were utilized to determine the residual stresses generated in the samples from the LSP-treatment and those in the treated coupons after thermal annealing/aging. For the CXRD measurements, a dedicated Proto LXR instrument was used with the standard $\text{Sin}^2\psi$ technique, which is described here briefly, though more detailed descriptions are available in published literature [21-23]. The energies of conventional X-rays used are small (20-40 KeV) and hence the diffraction data is obtained from the region closest to the surface (<20 μm). This shallow penetration depth can be coupled with electrolytic layer removal to obtain a high resolution through -the-depth measurement of stresses. At this shallow depth, plane stress conditions are assumed, i.e. two principal stresses (σ_1 and σ_2) exist in-plane and the out-of-plane σ_3 stress is assumed to be zero, although a strain component ϵ_{33} exists as a consequence of the Poisson effect caused by the two in-plane stresses. Figure 3 illustrates the basic principle and geometry of conventional XRD measurements. The definitions of the terms are as follows:

- ψ (psi): Defines the sample surface orientation and is the angle between the normal of the surface and the incident and diffracted beam bisector, which is also the angle between the normal to the diffracting lattice planes and the sample surface
- ϕ (Phi): Angle between a fixed direction in the plane of the sample and the projection in that plane of the normal of the diffracting plane
- $d_{\phi\psi}$: Interplanar spacing at given ψ and ϕ
- $\epsilon_{\phi\psi}$: Strain measured in the direction of measurement defined by the angles ψ and ϕ
- σ_1, σ_2 : Principal stresses acting in the principal directions
- σ_ϕ : Stress acting in a chosen direction, i.e. at an angle ϕ to σ_1

Consider tensile stress being applied to a body. The planes parallel to the surface experience a contraction due to Poisson's effect and hence the interplanar spacing in those planes becomes smaller. These planes can be sampled at $\psi = 0$. Meanwhile the planes that are oriented at a high angle to the surface experience different loading and an increase in interplanar spacing ($d_{\phi\psi}$). In order to get these planes to diffract the sample surface has to be tilted by the angle ψ , which allows measurement of strain in different directions at the same point.

The measured strain at different ψ can be related to stress by:

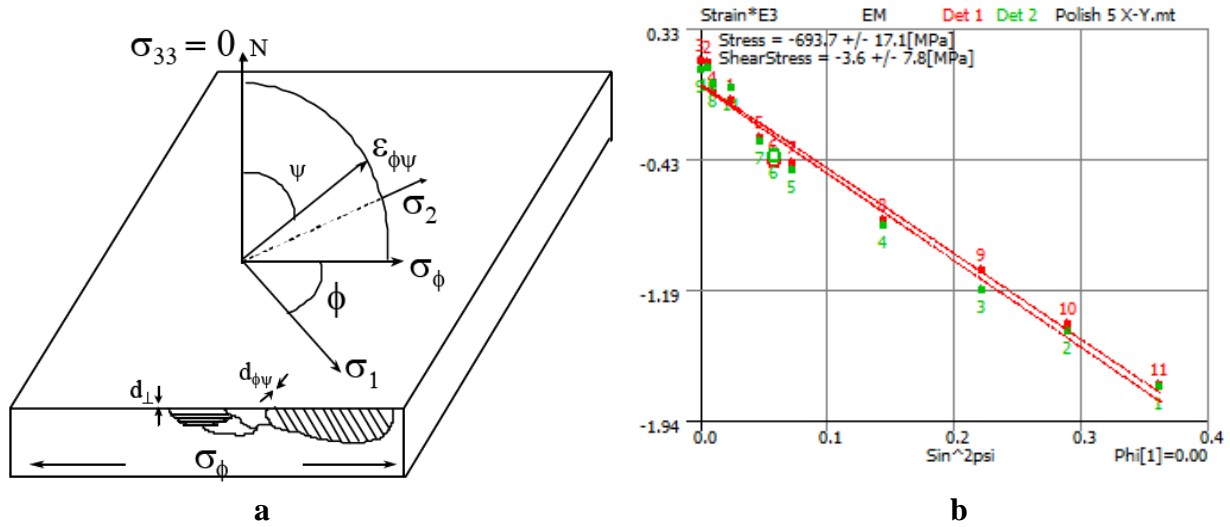


Figure 3: Basic Principle of the Sin2 ψ XRD Method for Determination of Residual Stress: (a) Definition of the Coordinate System and the Angles ψ , ϕ and (b) Strain vs. the Sin2 ψ Plot (Stress is Obtained From the Slope of the Regression Fit and the X-Ray Elastic

$$\frac{d_{\phi\psi} - d_0}{d_0} = \frac{1+\nu}{E} \sigma_{\phi} \sin^2 \psi - \frac{\nu}{E} (\sigma_{11} + \sigma_{22}) \quad (2)$$

$$s_1^{hkl} = \left(-\frac{\nu}{E} \right)^{hkl} \frac{1}{2} s_2^{hkl} = \left(\frac{1+\nu}{E} \right)^{hkl} \quad (3)$$

where s_1 and s_2 are plane specific X-ray elastic constants (XEC). These constants can be determined experimentally or by calculation, and are also available in the published literature and/or in the instrument software for the alloys of interest. The full derivation of the equation above, relating diffraction strain to the stress, is available in the published literature [21-23].

The Proto LXRD instrument used in the residual stress analysis contains two position sensitive detectors, allowing for data collection at two ψ tilts simultaneously. The instrument was calibrated using a stress-free sample standard and the alignment of the instrument was checked using reference standard samples in accordance with ASTM E915-96. Five such measurements were performed before each set of actual measurements to ensure proper alignment of the instrument. For residual stress analysis in the Ti6242 and Ti64 alloys, Cu K-alpha x-rays was used, with the {213} alpha-Ti peak for strain measurements, whereas for the IN718 SPF and IN718 Plus alloys, both Cu K-alpha x-rays with the {331} f.c.c. peak as well Mn K-alpha x-rays with the {311} f.c.c. peak were utilized. Measurements of the relevant diffraction peaks were made at five different values of $\pm\psi$. The peaks were fitted using a Pearson VII function to determine the interplanar spacing (d) and hence strain and the strain values were plotted as a function of $\text{Sin}^2\psi$. A regression fit to the d vs $\text{Sin}^2\psi$ data (example in Figure 3(b)) and x-ray diffraction elastic constants available in the software

module and/or literature were used to determine the in-plane residual stress. Measurements were conducted in two orthogonal in-plane directions ($0^\circ/X$, $90^\circ/Y$). In addition, the full-width at half maximum (FWHM) intensity, which is a measure of plastic strain, was determined. The residual stress as a function of depth from the peened surface was determined by sequentially electropolishing the surface of the peened samples using a Buehler electropolisher and then repeating the CXRD measurements. For electropolishing, a solution composed of 12.5% sulfuric acid-87.5% was used at room temperature, with voltage and flow rate appropriate for obtaining a mirror finish and controlled rates of material removal. The measured residual stress was corrected for stress gradients and relaxation due to layer removal using the standard Moore and Evans procedure available in the instrument software.

The SXRD characterization of residual stress was performed at the Advanced Photon Source at the Argonne National Laboratory (ANL) in beamline 11-ID-C. The residual stress distributions in LSP-treated samples of the IN718 Plus alloy and in those subjected to post-LSP thermal treatments were characterized. Details of the experiments, setup, and analysis are presented in the results and discussion section.

2.5 Thermal Stability Analysis

The LSP-treated samples were aged at temperatures and times appropriate for each alloy to study the relaxation of the LSP residual stresses using CXRD and SXRD and to model the kinetics. The aging temperatures used for the Ti6242 and Ti64 alloys were 316°C (600°F), 482°C (900°F) and 538°C (1000°F), whereas temperatures of 600°C , 650°C , 700°C , and 750°C were used for the IN718 SPF and IN718 Plus alloys. The aging times varied from a few minutes to 100 h at each temperature. The residual stress relaxation during initial heating to the selected temperature was also determined. Samples containing both single dimples and overlapped dimples were studied. In the case of the single-dimple samples, the residual stress relaxation at a given temperature was measured on the same dimple as a function of time, with separate single-dimple samples for each temperature. In the case of samples with overlapped LSP-induced dimples, separate samples were used for each temperature and time combination. The thermal aging behavior in non-LSP treated samples of the IN718 Plus alloy over the temperature range of 650 to 850°C was also studied to better understand the evolution and kinetics of formation of second-phase precipitates and hardening. Details of the procedures for the latter are described in the results and discussion section pertaining to the IN718 Plus alloy. The various thermal treatments were conducted either in evacuated and Argon back-filled quartz capsules or in a vacuum using an MRF high-temperature vacuum furnace. The kinetics of thermal relaxation of the LSP-induced residual stress were modeled and simulated using FEM and a Zener-Wert-Avrami formulation. Details of the methodologies used are described later in the results and discussion section.

2.6 Static, Fatigue and Fatigue Crack Growth Testing



a



b

Figure 4: Photographs of the (a) MTS 810 and (b) MTS 1000 Bionix Systems Used for the Static, Fatigue and Fatigue Crack Growth Tests

Static tensile and three-point bend (3PB) tests were conducted to determine basic properties, such as the yield strength, of the alloys that were studied. These tests were conducted using 100 kN MTS 810 and 25 kN MTS 1000 Bionix servohydraulic systems; photographs of these systems are shown in Figure 4. Tensile and axial fatigue testing were carried out using an MTS 810 machine, whereas both the MTS 810 and Bionix systems were used system for 3PB static and fatigue tests. The samples of specified geometry and dimensions were prepared by EDM and the surfaces generally polished to a mirror finish prior to LSP treatment and testing. A number of sample designs were attempted towards ensuring repeatability and minimizing data scatter. Some of the typical samples used are shown in Figure 5(a) below; further details of the specimen geometry and dimensions in the tests on the various alloys are provided later in the results and discussion Section.

For the axial static tests, both an extensometer as well as a strain gage affixed to the sample surface were used to measure strain, whereas only the latter was used in the 3PB tests. Fatigue and fatigue crack growth (FCG) tests were carried as per ASTM recommendations. Tests were carried out under load control using a sinusoidal waveform with load ratio (R) of 0.1 and frequency of 15 Hz. Unpeened, LSP-treated and LSP-treated + thermally aged samples were tested at room temperature. The bulk of the 3PB fatigue tests were conducted on notched samples. The notches were made by EDM on both unpeened, LSP-treated and LSP-treated + thermally aged samples. The notch tip had a radius of $170\ \mu\text{m}$ and a depth of $250\ \mu\text{m}$ from the bottom/tensile side under load of the unpeened and peened sample edges.

The crack length (a) was determined by an elastic unloading compliance technique using a high sensitivity MTS clip-on gage for measuring load-line displacement, as well as a home-built alternating current potential drop (ACPD) based lock in amplifier unit interfaced to a PC (Figure 5(b)). High-resolution load (P) and displacement (v) data were acquired periodically using MTS online data acquisition software with a PC. Crack closure values were determined by the compliance method and validated with ACPD. FCG rate (da/dN) and ΔK values were calculated following ASTM E 647 from the P - v data and the number of cycles (N). Stepwise K -decreasing and constant amplitude tests were performed during FCG pre-cracking and testing respectively. For the load shedding technique, before a load reduction (by not more than 10%) was made, it was ensured that in the previous stage, the crack increment was greater than $2(\Delta r_p)$, where Δr_p , is the current cyclic plastic zone size, is given by:

$$\Delta r_p = \frac{1}{4\pi} \left(\frac{K_{\max}}{\sigma_y} \right)^2 \quad (4)$$

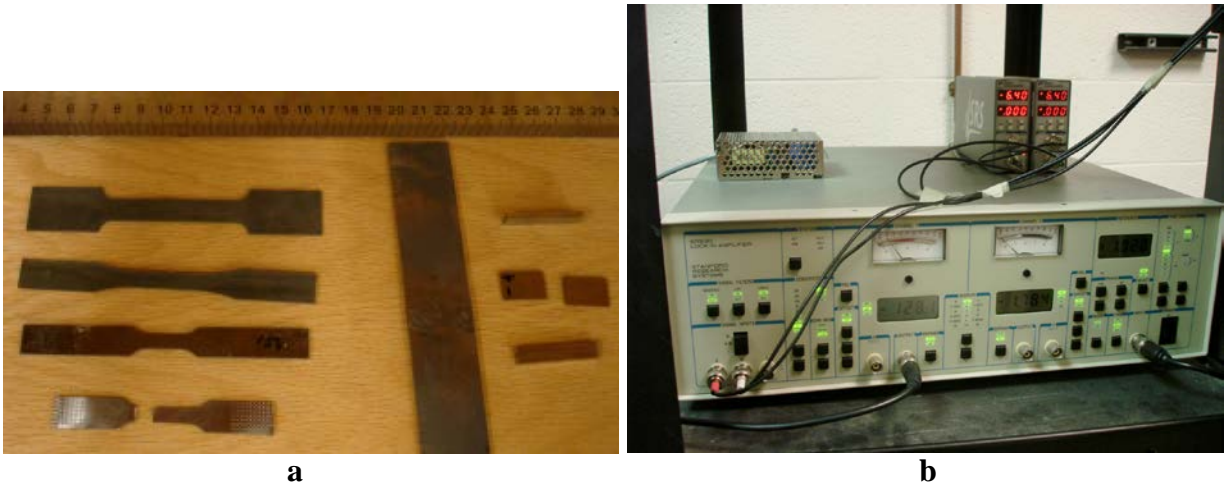


Figure 5: Photographs of the (a) Typical Test Samples and (b) ACPD System for Crack Length Measurements

Here, K_{\max} is the maximum stress intensity factor corresponding to the previous stage and σ_y is the yield strength. This was done to avoid the plastic zone of the previous stage influencing the FCG behavior in the subsequent stages after load shedding. The frequency ranges employed were 20 - 30 Hz for near-threshold testing and 2 – 20 Hz in the Paris regime.

2.7 Microstructure and Fracture Characterization

The microstructures of the unpeened, aged, LSP-treated and LSP-treated + thermally aged samples of the Ti6242, Ti64, IN718 SPF, and IN718 Plus alloys studied herein were characterized principally by optical microscopy (OM), scanning electron microscopy (SEM) and transmission electron microscopy (TEM). The OM observations were conducted on metallographically prepared unetched and etched samples using a Keyence VHX 600 digital optical microscope with micrographs recorded at a range of magnifications. Kroll's reagent (92 ml Distilled water, 6 ml HNO₃, 2 ml HF) was used as an etchant for the Ti6242 and Ti64 alloy samples, whereas a solution composed of 5% HCl + 1% H₂O₂ in ethanol was used for the IN718 SPF and IN718 Plus alloy

samples. Both unetched and etched samples were also observed in an FEI XL-30 ESEM utilizing secondary electron (SE) and back scatter electron (BSE) imaging, with photographs digitally recorded at appropriate magnifications. Energy dispersive x-ray spectroscopy (EDS) analysis was performed to ascertain the chemical compositions of phases present in the samples using an EDAX Genesis 4000 thin-window EDS system attached to the XL-30 SEM. Orientation imaging microscopy (OIM)/electron backscatter diffraction (EBSD) observations of polished sections were also conducted, using a TSL 4000 system attached to the XL-30 SEM, to ascertain texture, characterize grain boundary types and sub-grains, and to obtain evidence for LSP-induced plasticity. Fracture surfaces of the failed fatigue-tested samples were also observed using the same SEM to characterize fracture initiation, features, modes, and the presence of striations for evaluating crack growth rates. The finer details of the microstructures of the unpeened, aged, LSP-treated, and LSP-treated + aged samples of the alloys, particularly the nature of second phase precipitates, their structure, size, distribution, morphology, volume fraction, chemistry, and interface with the matrix, grain boundaries, and dislocation structures were studied by TEM and selected area electron diffraction, coupled with the ancillary techniques of EDS, and weak-beam dark field (WBDF) imaging. Thin foils for TEM were prepared by punching 3 mm discs from the unpeened, peened (plane as well as cross-section), and thermally aged samples, polished to a thickness of $\sim 100 \mu\text{m}$, followed by twin-jet electro polishing of the 3 mm discs to perforation in a Fischione unit using a solution of 10% perchloric acid in ethanol at -30°C . The foils were observed in a FEI CM20 TEM operated at 200 kV and photographs were recorded under bright field (BF), dark field (DF), WBDF selected area diffraction (SAD), and convergent beam electron diffraction (CBED) modes. Chemical compositions of the phases present were analyzed using an EDAX Genesis 2000 thin-window EDS system attached to the same TEM.

2.8 Modeling and Simulation

The objective of the modeling and simulation (M&S) effort was to develop robust models and simulation codes for predicting and verifying thermal-mechanical stabilities associated with the LSP process. The M&S work was focused on studying the evolution of residual stresses induced by LSP and the thermal stability of these stresses, and the results obtained were correlated with the experimental data to establish a comprehensive understanding of the relations among the process parameters and residual stress evolution. Specifically, the following areas were addressed:

1. Modeling the pressure load generated by LSP.
2. Performing FEM simulations with appropriate material constitutive behavior models to study the effects of processing parameters (pulse input energy, pressure, spot size, duration) and specimen configurations (size, shape, boundary conditions) on the residual stress distributions in the near-surface regions.
3. Performing FEM to study the thermal relaxation of LSP-induced residual stresses, validation with experimental data, and predictions of long-term behavior.
4. Analytical modeling of the kinetics of residual stress relaxation from the experimental and simulation results.

Detailed descriptions of the methodologies employed and the findings are presented in the results and discussion section.

3.0 RESULTS AND DISCUSSION

The results of this project are described in the following sub-sections in the form of plots, tables, micrographs and simulations.

3.1 Experimental and Finite Element Modeling and Simulation of LSP-Induced Residual Stresses and Thermal Relaxation in IN718 SPF, Ti64 and Ti6242 Alloys

The relaxation of the compressive residual stress in surface treated titanium and nickel-base turbine engine alloys due to thermo-mechanical loading can significantly affect their fatigue life and hence the performance of engine and aerospace structures, since the beneficial effect of surface treatment stems from the compressive residual stress at and near the surface region [24-26]. Hence, understanding the relaxation of residual stress is critically important in the prediction of the service life of components. The relaxation behavior is primarily caused by three mechanisms: mechanical, thermal, and thermomechanical. The latter relaxation is a complex process and generally the combination of thermal and mechanical effects. When studying the residual stress relaxation behavior of AISI 4140 steel under conventional fatigue at elevated temperatures, Holzapfel et al. [27] found that the thermal and mechanical relaxation can be regarded as independent processes, which was also confirmed Lee and Mall [28] in the investigation of high-temperature fretting fatigue of shot-peened Ti-6Al-4V. Therefore, a good understanding of the thermomechanical relaxation behavior of residual stress requires a fundamental study of each of the thermal and mechanical mechanisms and their interaction. Mechanical relaxation occurs when the superposition of applied stress and residual stress reach the yield strength of material. The important factors are temperature, applied stress, loading frequency, and number of cycles.

In contrast, thermal relaxation of residual stress at elevated temperatures is essentially attributed to the annihilation and reorganization of meta-stable crystalline defects induced by a peening process [29], creep-controlled dislocation rearrangement, and material softening at elevated temperatures, etc. For thermal relaxation, numerous studies have shown that the temperature, exposure time, and level of initial cold work (plastic deformation) are the primary parameters. Vöhringer et al. [30] found no relaxation of SP residual stress at the surface at 300°C in Ti-6Al-4V, and progressively greater relaxation at higher temperatures (from 400°C up to 600°C). Lee and Mall [28] found about 94% relaxation of residual stresses in shot peened Ti-6Al-4V exposed to 370°C for 24 h, compared with 11% relaxation at 100°C for 24 h. They also observed the relaxation rate (stress relaxation/time) increased with increasing temperature. Khadhraoui et al. [31] conducted experimental investigations of thermal stress relaxation in IN718 after different exposure times at 600°C and 650°C and found that the higher the test temperature, the greater the stress relaxation. The test temperature had no significant effect on the pattern of the depth profile of residual stress. The effects of exposure time were also addressed by several researchers [32-34], and these studies indicated that a large portion of total relaxation occurred in the initial period of exposure, followed by a stabilization of stress. Prevey et al. [24] studied the thermal relaxation of the compressive layer produced by SP, gravity peening, and LSP in engine alloys Ti-6Al-4V and IN718 at engine temperatures. Initial thermal relaxation of highly cold worked surfaces can be extremely rapid in both alloys, and can result in 50% loss in less than 10 minutes even at moderate engine temperatures (400~500°C). However, for laser shock peened coupons, only a small relaxation near the surface occurred in Ti-6Al-4V and no thermal stress relaxation was found in IN718 at even the highest temperature studied (475°C for Ti-6Al-4V and 670°C for IN718), from which it was concluded that LSP is more resistant to thermal relaxation than conventional SP due to less cold working generated at the surface. Later on, Buchanan [35] argued that the depth of plastic strain and not just the

surface value contribute to the relaxation of residual stresses induced by surface treatments. It must be emphasized that the thermal stability of peening residual stresses is dependent on several critical peening parameters, including intensity, coverage, and the resulting cold work. Therefore, the individual experimental results cited here cannot be regarded as a general case.

Compared to the extensive experimental studies cited here on thermal stability of peening residual stresses, very limited analytical work [36-38] has been done on this topic by via FEM. The experimental investigation is necessary, but expensive, and sometimes unreliable due to the factors arising from setting up the LSP process and residual stress measurement. As a robust mathematical method, FE simulation can provide guidance for performing better experiments and also serve for obtaining good predictions of physical phenomena in the absence of experimental data. Motivated by the importance of this subject, effort has been made in this project to study the stability of LSP-induced residual stress in the IN718 SPF, Ti64 and Ti6242 alloys under thermal relaxation by experiments and FE simulation. The experimental results are presented first and then followed with the FE simulation results.

3.1.1 Experimental Results of Residual Stress and Thermal Relaxation

3.1.1.1 IN718 SPF Alloy. This alloy was obtained from Special Metals Corporation in sheet form with a thickness of 2 mm. The as-received sheet was annealed and heat-treated as per AMS 5950 specification and then aged at 750°C for 5 hours to precipitate harden it. An OIM micrograph of the microstructure of the alloy is shown in Figure 6. Two sets of coupons, measuring 38 mm x 38 mm and 14 mm x 14 mm, were sectioned using electrodischarge machining (EDM). Coupons were LSP-treated at UC using a GEN I Nd:Glass laser ($\lambda=1052$ nm). Two different laser energy conditions were used:

1. Energy= 8J, pulse width = 28.6 ns, spot size (diameter) = 2 mm, power density = 9 GW/cm².
2. Energy= 16J, pulse width = 25.3 ns, spot size (diameter) = 2 mm, power density = 16 GW/cm².

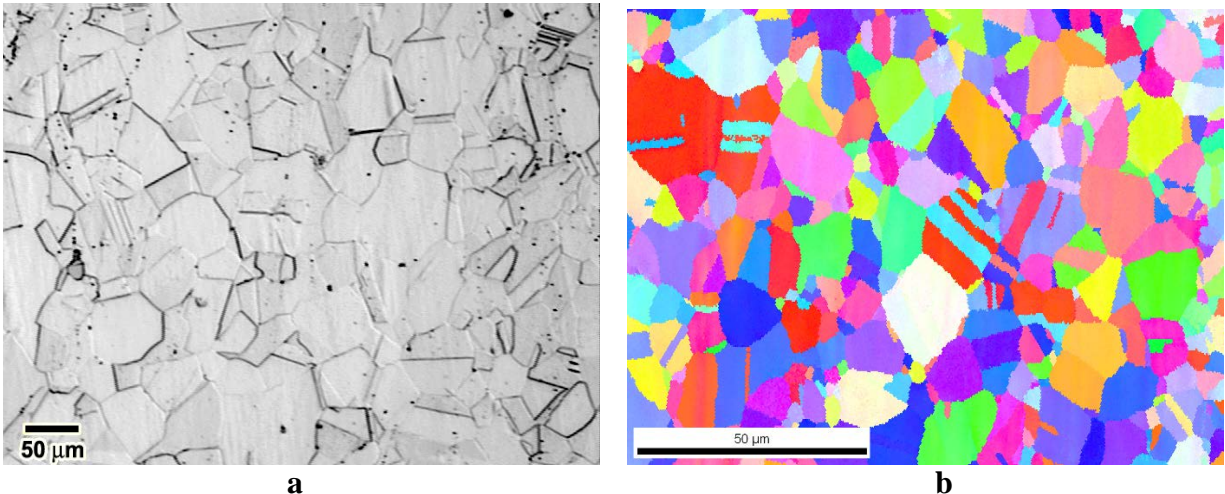


Figure 6: Representative (a) OM and (b) OIM Micrographs of Microstructure of As-Received IN718 SPF Alloy

Three sets of LSP-treated coupons were made:

Set 1: 38 mm x 38 mm coupons: A patch of 10 mm x 10 mm was peened with a 50 % overlap with both energy conditions

Set 2: 14 mm x 14 mm coupons: 2 mm diameter single spot was peened with 3 impacts at the same spot with power density of 9 GW/cm²

Set 3: 38 mm x 38 mm coupons: A patch of 10 mm x 10 mm was peened with a 50 % overlap with power density of 9 GW/cm²

The LSP-treated coupons were aged as follows: For those in Set 1, one sample was peened for each temperature- time condition of 600°C 1 h; 650°C (1 h, 24 h, 100 h); and 700°C (1 h, 24 h) and the through thickness residual stresses were measured in each of the samples. For those in Set 2, one sample was peened for each temperature-time condition of 600°C (10 mins, 1 h, 24 h) and 650°C (10 mins, 1 h, 24 h) and the through thickness residual stresses were measured in each of the samples. For those in Set 3, one sample was peened for each temperature of 550°C (5 mins, 10 mins, 20 mins, 40 mins, 1 h, 2 h, 5 h); 650°C (5 mins, 10 mins, 20 mins, 40 mins, 1 h, 2 hrs, 5 hrs); 700°C (5 mins, 10 mins, 20 mins, 40 mins, 1 h, 2 h, 5 h); and only the surface residual stresses were measured.

Conventional XRD using a Proto LXR system with electro polishing was used to obtain residual stresses from different depths in the as-LSP-treated and LSP-treated + thermally aged samples. Details are provided in the Table 3 below. All specimens were electro polished using 125mL H₂SO₄:875mL CH₃OH solution to remove layers of the material in the peened region. Residual stresses were measured at each depth. Strain gradient and layer removal corrections were performed to determine the actual residual stress profile through the depth.

Table 3. Details of Experimental Conventional XRD Measurements of Residual Stress in LSP-Treated IN718 SPF Alloy

<u>Item</u>	<u>Condition</u>
Equipment	Proto LXR
Detector	PSSD (Position sensitive scintillation detector), 20° 2θ range
Power	25 KV and 25 mA
Radiation	Mn Kα ₁ (λ = 2.10314Å)
Tilt axis and angles	Ω Angles: 0°, 2.58°, 9.07°, 12.45°, 18.8°, 23.0° (Equal steps of sin ² ψ)
Plane(Bragg's Angle)	{311} set of planes. Bragg's angle: 152°
X-ray elastic constant	S2/2: 7.14 x 10 ⁻⁶ MPa ⁻¹

Set 1: The results of residual stress and diffraction peak FWHM in the as-peened 9 GW/cm² and 16 GW/cm² power density coupons are shown in Figure 7, whereas the same data after aging the counterpart coupons at 600°C, 650°C, and 700°C for various times are displayed in Figures 8 and 9 respectively. The compressive residual stresses were larger in the near-surface regions to a

distance of 100 μm in the 16 GW/cm^2 peened sample compared with the 9 GW/cm^2 peened sample, but were more or less the same at distances beyond 100 μm ; the residual stresses became tensile eventually at distances beyond ~ 500 μm in both cases. Likewise, the diffraction peak FWHM and hence plastic strain in the near-surface regions of 16 GW/cm^2 peened sample was greater than that in the 9 GW/cm^2 peened samples to a distance of ~ 350 μm and became more or less the same at larger distances. Post-aging of the peened samples led to relaxation in the residual stress both at the surface and sub-surface, with the magnitude of reduction being greater at higher temperatures and/or longer times and also being dependent on the initial peening energy and distance below the peened surface (Figures 8(a), 9(a)).

The strong effects of temperature and time can be noticed, but it is significant that $\sim 20\%$ of the initial compressive residual stress is retained after aging at 700°C for 24 h. The changes in the near-surface plastic strains as manifested by the diffraction peak FWHM with aging temperature and time appear to be more complex and these strains seem to be more resistant to relaxation than the macro (elastic) residual stresses. Indeed, following aging at 650°C for 24 h and 100 h, the FWHM values at the surface drop only slightly compared with the as-peened condition and remain high and nearly constant through the distance from peened surface. This may be associated with coherency strains caused by new precipitation of γ'' or γ' during the aging, but more work is required to fully understand this behavior.

Set 2: Figure 10 shows the residual stress vs. depth profile for single dimple samples. Again, most of the relaxation takes place at the surface (initial 100 μm or so from the peened surface), with higher temperatures or longer times leading to more relaxation. The sub surface stresses are not affected much even at longer times and higher temperatures.

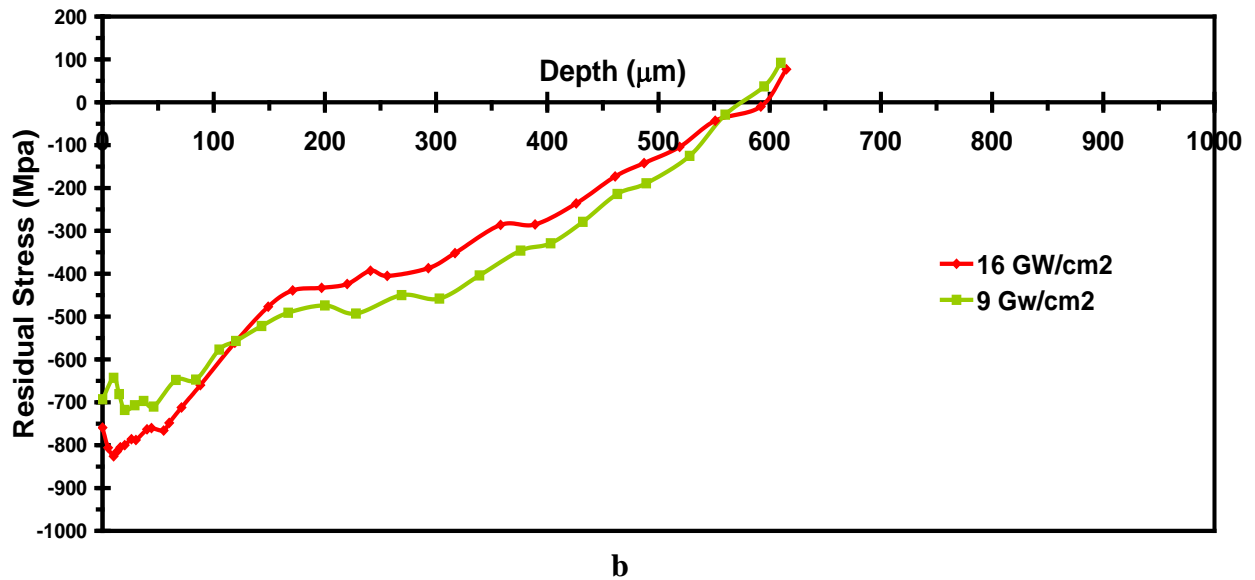
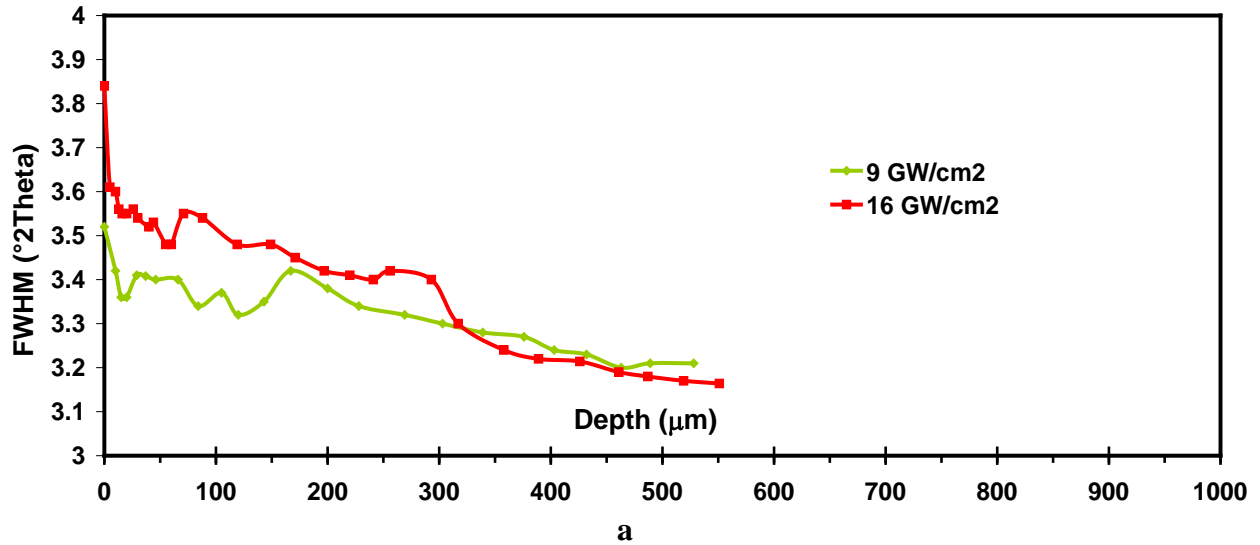
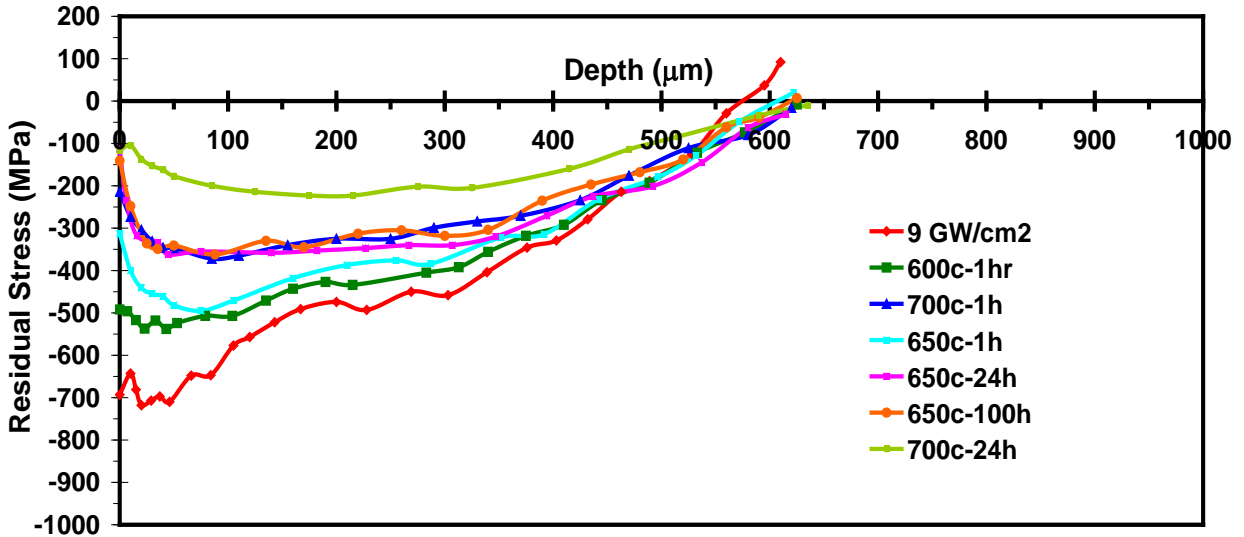
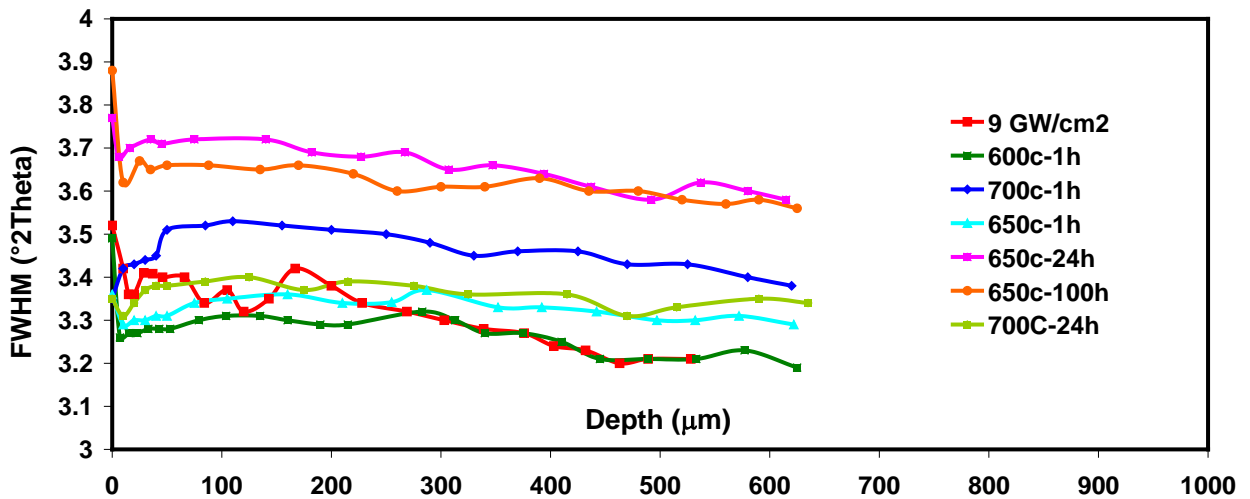


Figure 7: (a) Diffraction Peak FWHM and (b) Residual Stress vs. Depth From Peened Surface in IN718 SPF Coupons for Two Different Power Densities

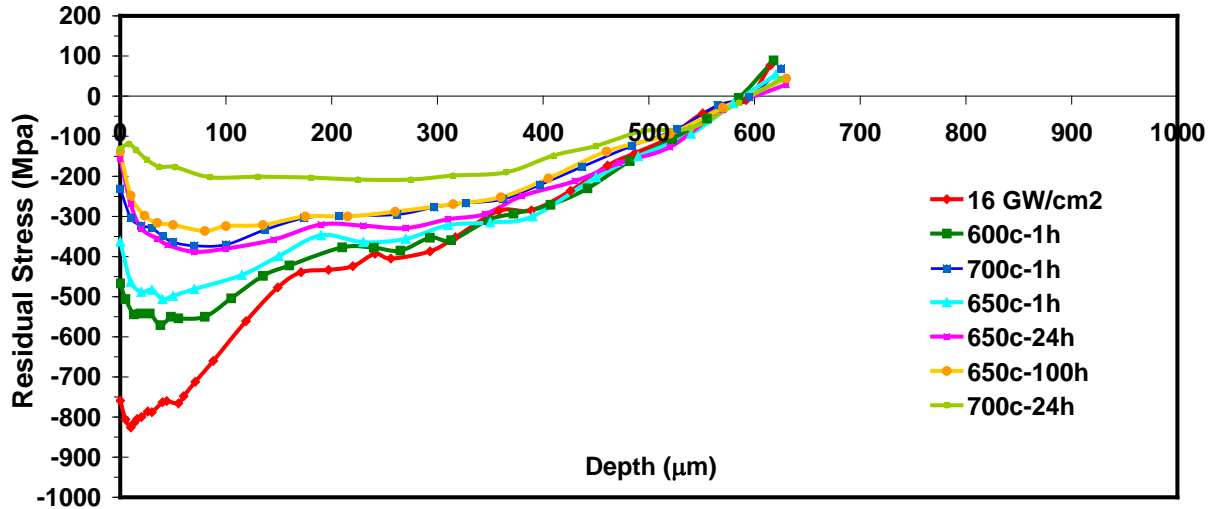


a

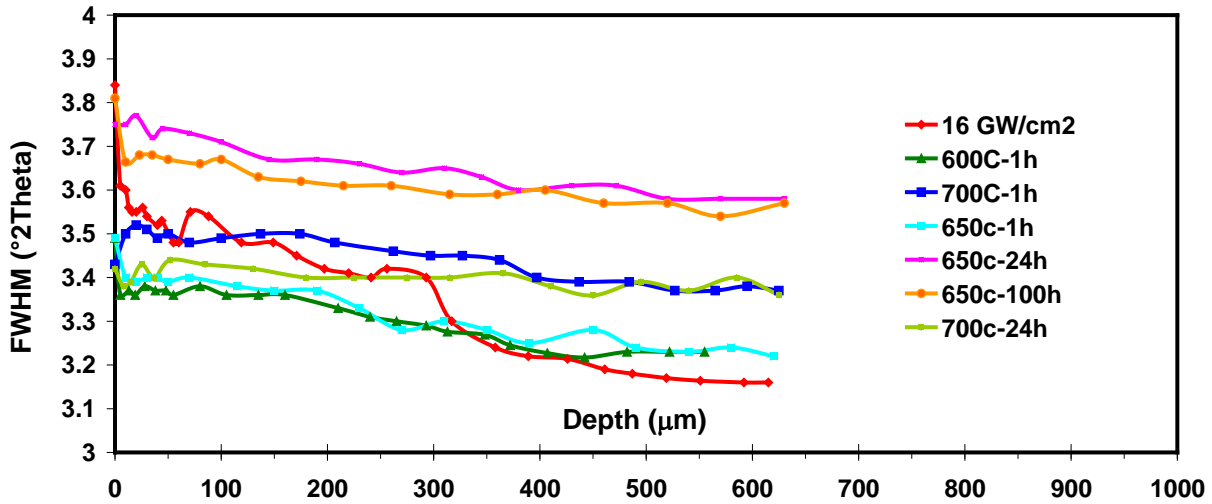


b

Figure 8: (a) Residual Stress and (b) Diffraction Peak FWHM vs. Depth From Peened Surface of 9 GW/CM² IN718 SPF Sample



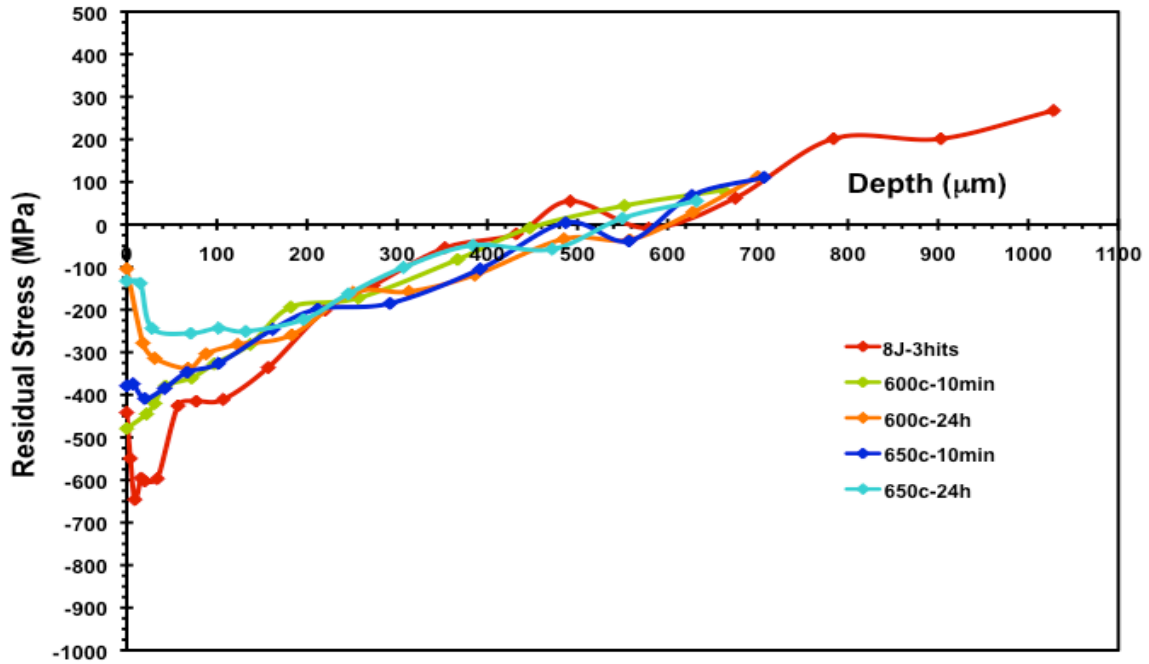
a



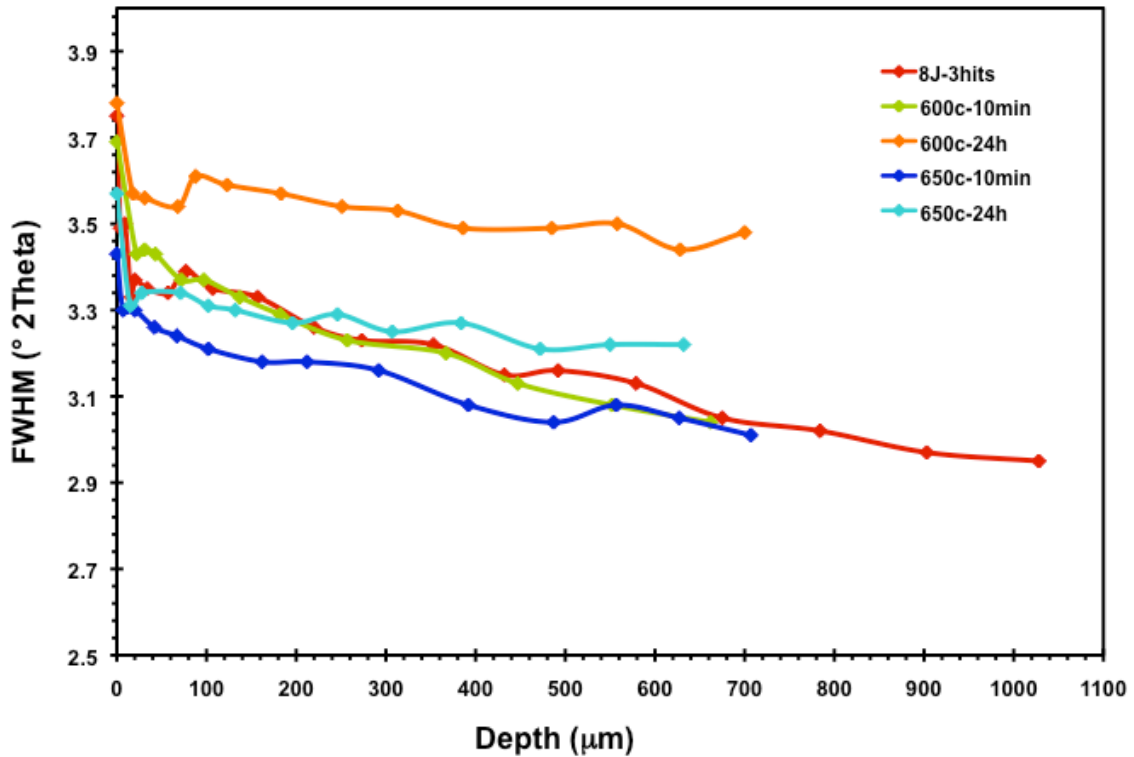
b

Figure 9: (a) Residual Stress and (b) Diffraction Peak FWHM vs. Depth From Peened Surface of 16 GW/cm² IN718 SPF Sample

Set 3: At all temperatures, the residual stresses at the surface show the highest rate of relaxation during the initial heating period. The rate of relaxation slows down after the initial 10 minutes or so. Figure 11 shows the surface residual stress as a function of time for different temperatures. In the case of 550°C, 15% of the residual stress is relaxed in the first 10 minutes and is then more or less stable for up to 5 h, where it then relaxes up to ~22% of the original stress levels. At 600°C, ~10% of the relaxation happens in the first 5 minutes. The stresses drop by ~30% after 20 minutes and to ~40% after 40 minutes, after which there is little or no relaxation until 120 minutes. On further exposure (5 h), the stresses relax to ~70% of the initial value. At 650°C, rapid relaxation occurs (~30%) within the first 5 minutes of exposure. No further relaxation occurs until 20 minutes and after 40 minutes exposure the stress drop to ~40% of the initial value. No further relaxation takes place until 2 hours, but after 5 hours, the stresses are reduced to ~70% of the original level.



a



b

Figure 10: (a) Residual Stress and (b) Diffraction Peak FWHM as Function of Depth for Various Aging Treatments in a Single Dimple LSP-Treated IN718 SPF Sample

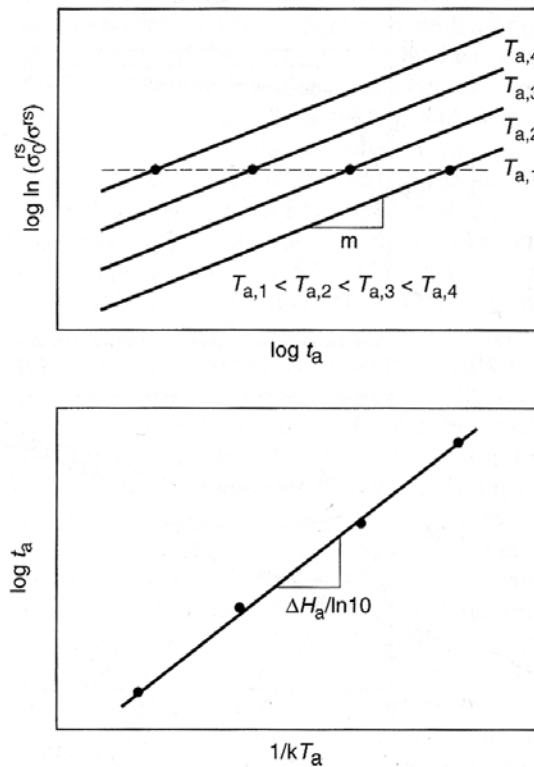


Figure 11: Schematic of Determination of Thermal Relaxation Kinetic and Thermodynamic Parameters in the Avrami Approach (From Ref. [40])

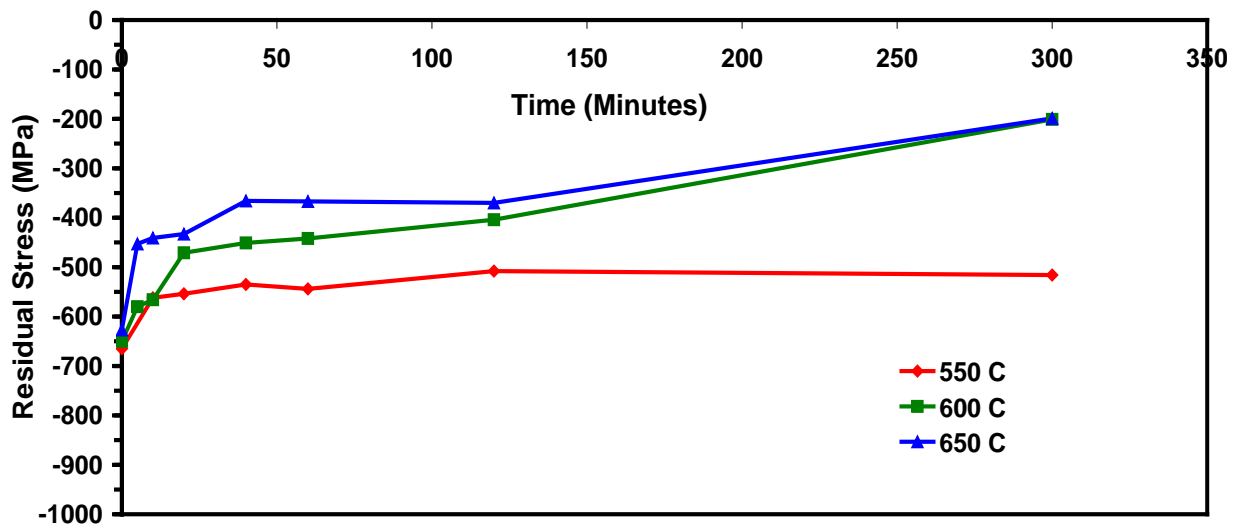


Figure 12: Surface Residual Stress as a Function of Exposure Time for Different Temperatures LSP-Treated IN718 SPF SET 3 Samples

The data from the residual stress thermal relaxation measurements were used to perform a kinetic analysis of the relaxation process and to identify the rate controlling factors. As shown in previous

studies in shot-peened steels [40], the effect of time on residual stress relaxation can be linearized with the help of a Zener-Wert-Avrami function [41] to:

$$\frac{\sigma^{rs}}{\sigma_0^{rs}} = \exp\left[-(At_a)^m\right] \quad (5)$$

where σ^{rs} is the macro residual stress at a given time t_a at temperature T_a , σ_0^{rs} is the initial (298K) macro stress prior to annealing, m is a numerical term dependent on the dominant relaxation mechanism, and A is a function dependent on material and temperature according to:

$$A = B \exp\left[-\frac{\Delta H}{kT_a}\right] \quad (6)$$

where B is a constant, k is the Boltzmann constant, and ΔH is the activation enthalpy for the relaxation process in the t_a - T_a range under consideration. It follows from equation (5) that

$$\log \ln\left(\frac{\sigma^{rs}}{\sigma_0^{rs}}\right) = m \log t_a + m \log A \quad (7)$$

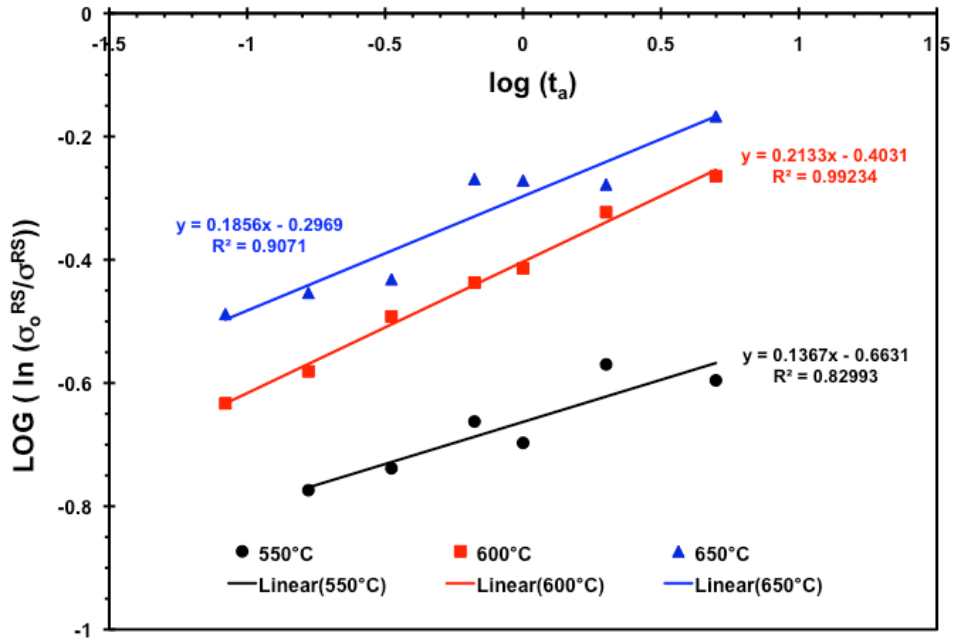
with the result that for a constant annealing temperature T_a , a plot of $\log \ln(\sigma^{rs}/\sigma_0^{rs})$ versus $\log t_a$ gives a straight line (see Figure 12). Corresponding annealing temperatures and times for constant $\sigma^{rs}/\sigma_0^{rs}$ can be derived from such plots, as illustrated schematically in Figure 12 in the $\log t_a$ versus $1/kT_a$ plot, where it can be seen that the values for constant $\sigma^{rs}/\sigma_0^{rs}$ lie on a straight line based on equations (5) and (6); this line results in:

$$\log t_a = \text{constant} + \frac{\Delta H}{\ln 10 \cdot kT_a} \quad (8)$$

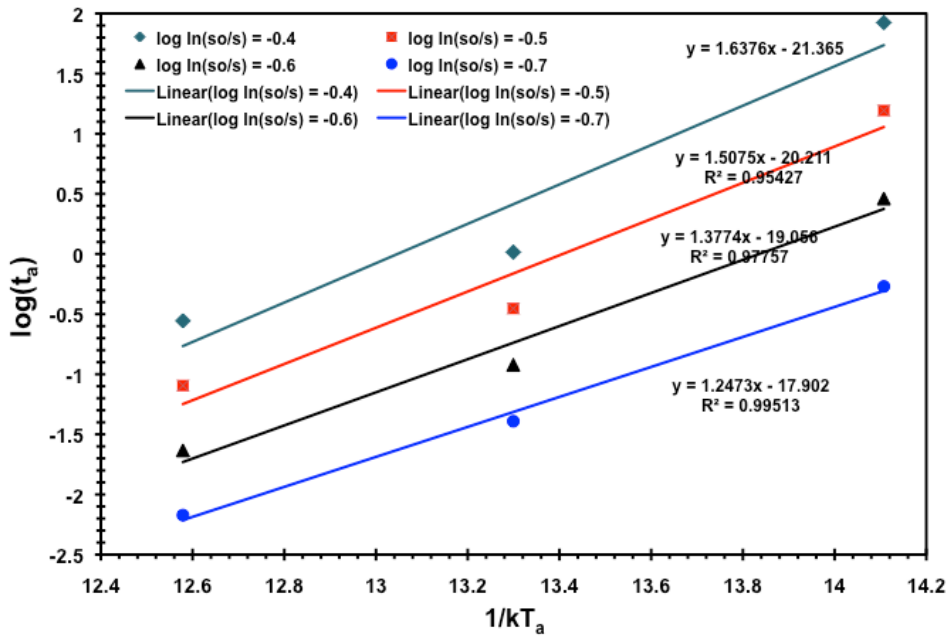
$$t_a = t_0 \exp\left(\frac{\Delta H}{kT_a}\right) \quad (9)$$

where t_0 is a time constant. The slope of the $\log t_a$ versus $1/kT_a$ plot in Figure 12 yields the activation enthalpy, ΔH , for the residual stress relaxation.

The data from the surface stress measurements in samples from Set 3 that had been peened and aged at different temperatures and times was analyzed as per the above procedures. A plot of $\log \ln(\sigma_0^{rs}/\sigma^{rs})$ vs $\log t_a$ is shown in Figure 13(a), from which it is evident that reasonable linear fit to the data at each temperature is obtained; the value of the slope m at 550°C (~ 0.14) is somewhat lower than those at 600 ($m \approx 0.21$) and 650°C ($m \approx 0.19$), which points to sluggish kinetics of relaxation at the lowest temperature. A plot of $\log t_a$ to attain a given constant value of $\log \ln(\sigma^{rs}/\sigma_0^{rs})$ (of -0.7, -0.6, -0.5, and -0.4, corresponding to stress relaxation to a level of 82, 78, 72, and 67% of the initial value) is shown plotted vs $1/kT$ in Figure 13(b). A reasonable linear fit to each data set is obtained, especially for those corresponding to the shorter times, giving an activation enthalpy, ΔH , corresponding to the above of 239, 264, 289, and 314 kJ/mole (i.e., 2.87 to 3.77 eV). These values are in the range of 224 to 315 kJ/mole (2.689-3.271 eV) reported for volume diffusion of Al and self-diffusion of Ni in Ni-base alloys from the literature [42, 43]. These results suggest that the



a



b

Figure 13: Plots of (a) $\log \ln(\sigma_0^{RS}/\sigma^{RS})$ vs. $\log t_a$ and (b) $\log t_a$ Corresponding to Specific Levels of Stress Relaxation vs. $1/kT_a$ for Determination of the Activation Energy Associated with the Relaxation Process in the IN718 SPF Alloy

residual stress relaxation is caused by a creep-like mechanism involving rearrangement and annihilation of dislocations by climb. It should be noted that after the initial stress relaxation, subsequent relaxation becomes considerably lower (much higher activation energies) because the driving force is reduced and the stress levels may have dropped to levels below the creep strength of the alloy at temperature.

3.1.1.2 Ti6242 and Ti64 Alloys.

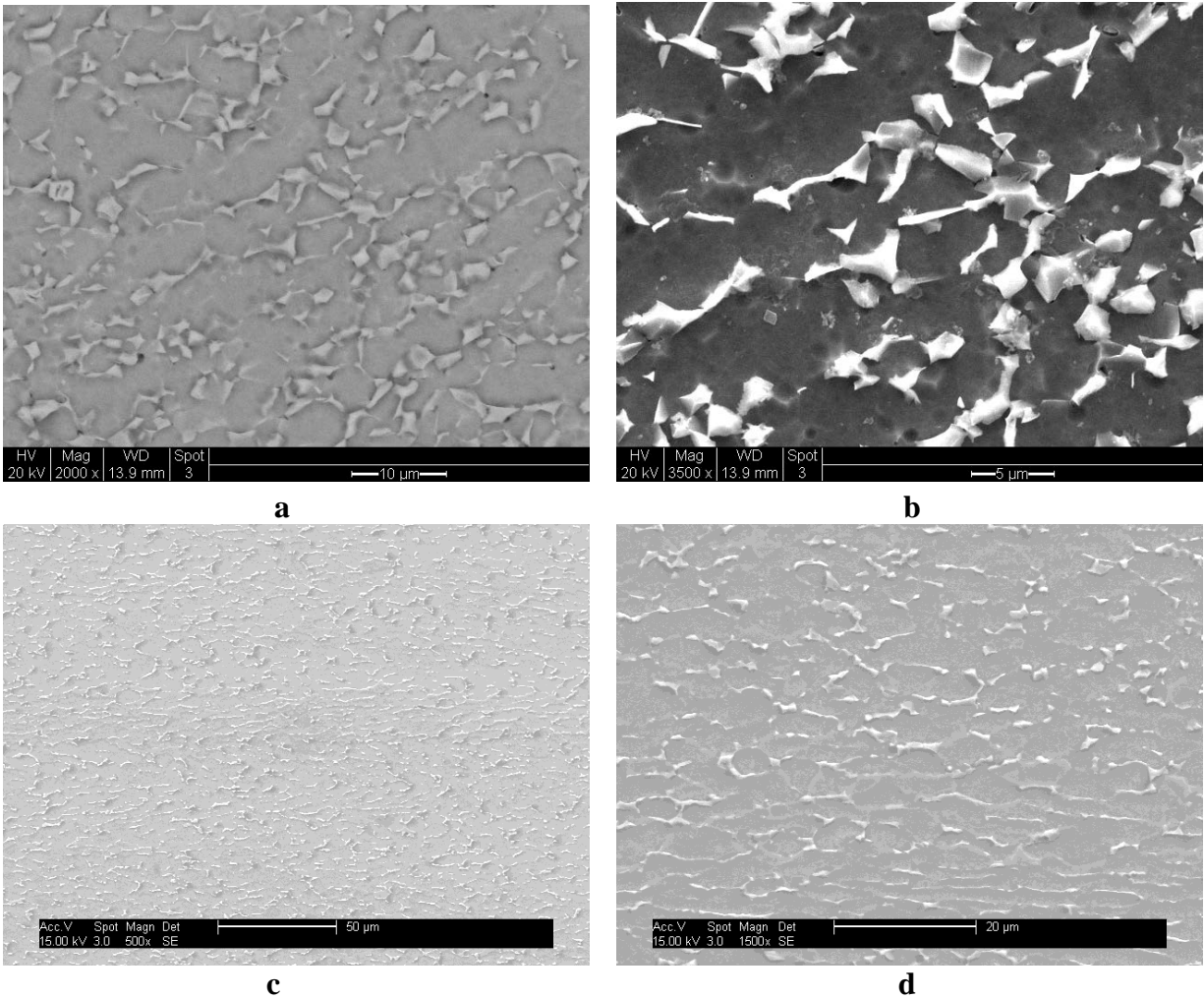


Figure 14: Representative (a) SE, (b) BSE Micrographs of Microstructure of As-received Ti6242 Alloy and (c), (d) SE Micrographs of As-Received Ti64 Alloy

The Ti6242 material was obtained from AFRL/RBSM (Dr. Kristina Langer) in the form of an L-shaped plate approximately 300 mm long x 125 mm wide x 4.3 mm thick, whereas the Ti64 coupons were obtained from GE Aviation in the form of coupons 35 mm² square x 2 mm thick. Both the Ti6242 and Ti64 alloys were in the mill-annealed condition. The secondary electron (SE) and backscattered electron (BSE) images of the microstructure of the as-received materials are shown in Figure 14, which in both cases is composed of irregularly-shaped retained β particles in an mostly α matrix having a grain size of \sim 5 μ m.

The majority of the work was focused on the Ti6242 alloy, with a limited set of single-dimple LSP treatments being conducted on the Ti64 alloy for calibration and comparison with the FE modeling and simulation. Initially, two types of LSP-treated coupons were studied for establishing base-line process parameter effects and for following the thermal relaxation behavior. A schematic of the first set of Ti6242 coupons is shown in Figure 15(a). Details are as follows:

1. Coupon dimensions of 90 mm long x 10 mm wide x 4.2 mm thick;

2. One LSP patch of 10 mm x 10 mm with 3 energy conditions (2 mm spot size, 32 ns pulse width and 8J single patch, 16 J single patch, 8J double-patch/layers); and

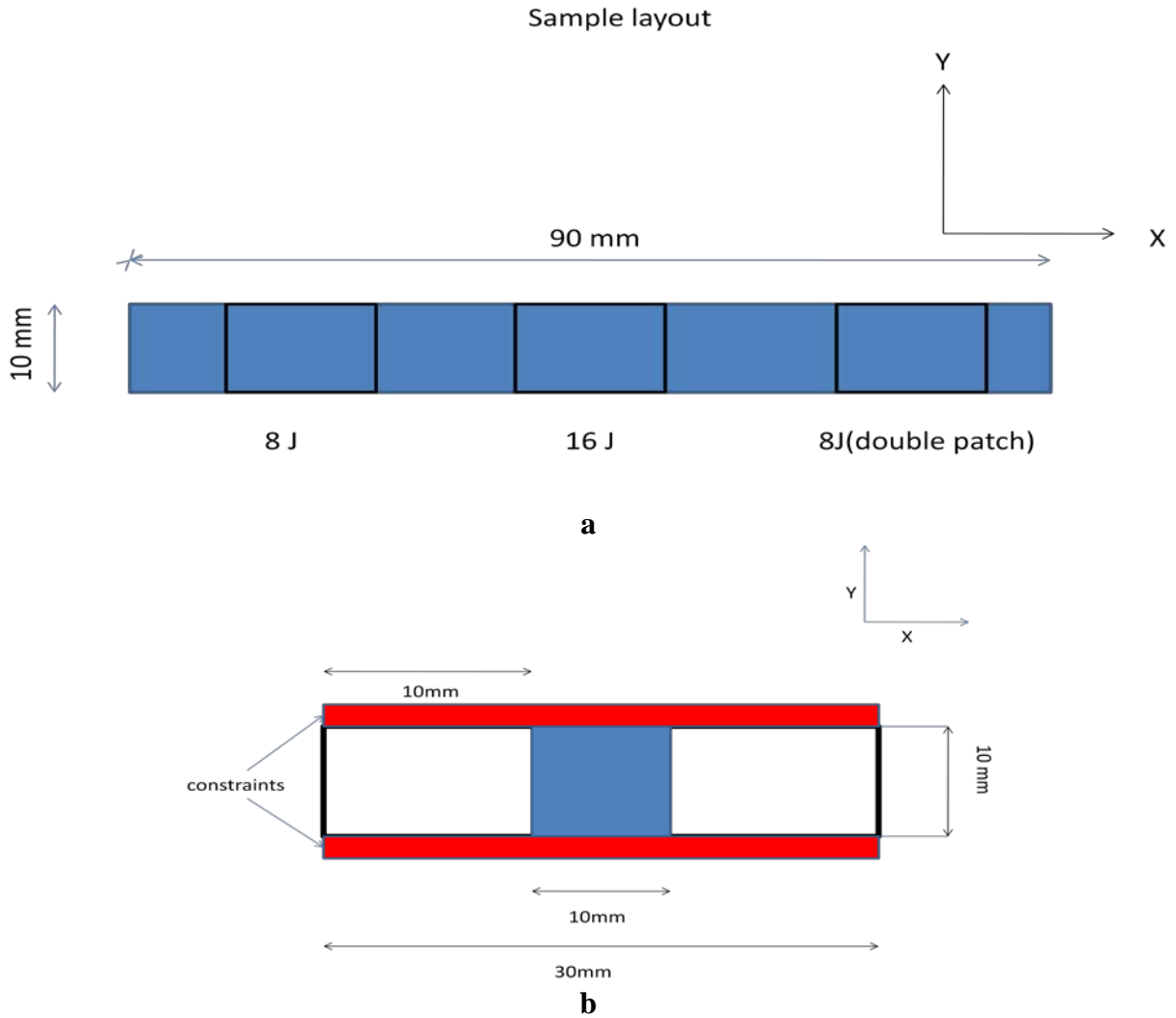


Figure 15: Schematic Showing the Geometry and Dimensions, LSP Patch and Energy Conditions for the Ti6242 Coupons for (a) Establishing Base-Line Process Parameter

3. Dual side peening with simultaneous shots on both sides. The corresponding power densities are 7.95 J/cm^2 and 15.9 J/cm^2 . Every peening sequence contained 9 shots and there were 9 such sequences. Dimensional and other details for the second set of coupons for the thermal relaxation studies is shown in Figure 15(b). In this case, the coupon had a length of 30 mm x width of 10 mm x thickness of 4.2 mm and a single 10 mm x 10 mm, double sided- LSP treated area was produced, with beam energy of 8J, 2 mm spot size and 32 ns pulse width (power density of 7.95 J/cm^2).

Conventional XRD using a Proto LXR system with electro polishing was used to obtain residual stresses from different depths in the as-LSP-treated and LSP-treated + thermally aged samples. The aging treatments were conducted at temperatures of 315°C (600°F), 482°C (900°F) and 538°C (1000°F) for times from 1 to 1440 minutes. Microhardness of the LSP-treated and LSP-treated + thermally aged samples was measured. Details of the conditions for the XRD

measurements are provided in the Table 4 below. All specimens were electro polished using 12.5% H₂SO₄ - 87.5% CH₃OH solution to remove layers of the material in the peened region. Residual stresses were measured at each depth. Strain gradient and layer removal corrections were performed to determine the actual residual stress profile through the depth.

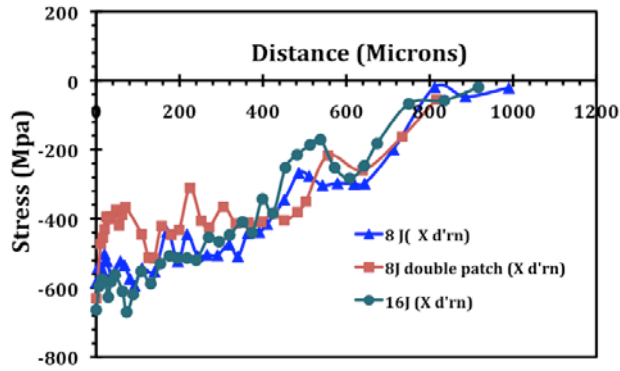
Table 4. Details of Experimental Conventional XRD Measurements of Residual Stress in LSP-Treated Ti6242 and Ti64 Alloys

<u>Item</u>	<u>Condition</u>
Equipment	Proto LXR D
Detector	PSSD (Position sensitive scintillation detector), 20° 2θ range
Power	25 KV and 25 mA
Radiation	Cu Kα ₁ (λ = 1.5412Å°)
Tilt axis and angles	Ω Angles: 0°, 1.59°, 6.04°, 12.22°, 19.0°, 23.0° (Equal steps of sin ² ψ)
Plane(Bragg's Angle)	{213} set of planes. Bragg's angle: 142°
X-ray elastic constant	S ₁ : 2.83 x 10 ⁻⁶ MPa ⁻¹ ; S ₂ /2: 11.89 x 10 ⁻⁶ MPa ⁻¹

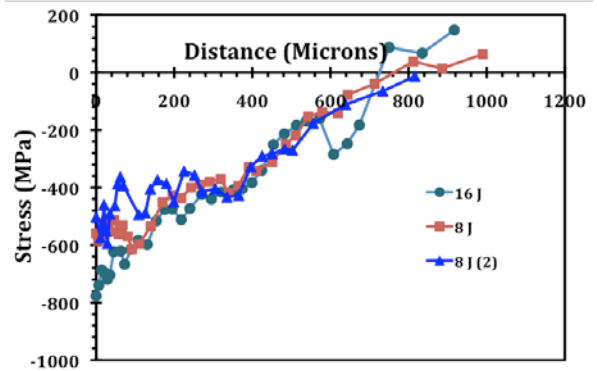
The residual stress and diffraction peak FWHM as functions of distance from the peened surface in the first set of coupons along two in-plane orthogonal directions X and Y for various beam energies are shown in Figures 16(a,b) and 16 (c,d), respectively. As can be seen, relatively high compressive residual stresses, with levels approaching -800 MPa at the surface, are present and diminish in magnitude with distance from the peened surface to ~700 microns before becoming slightly tensile in nature. The near-surface compressive residual stress values are slightly higher in the 16 J peened sample compared with the 8J peened samples (single and double hits), but the values more or less overlap within the depth, which points to a saturation type effect of the laser beam energy. The FWHM values, which are a measure of plastic strain, are high at the surface, especially in the 16J peened samples and decrease to a more or less constant value at distances beyond about 100 microns.

The results from the second set of coupons of the effects of the thermal aging on the micro-hardness changes is shown in Figure 17, whereas those of residual stress and FWHM (i.e. plastic strain) relaxation in two in-plane orthogonal directions X and Y are shown in Figures 18(a,b) and 18(c,d), respectively. The hardness data shows that the LSP-treatment leads to ~14% increase in the hardness over that of the unpeened material. There is little to no change/decrease in the hardness following aging of the peened samples at 315°C, whereas aging at 482°C and 538°C leads to ~5-7% decrease in the hardness, but the values still remain higher than that of the unpeened sample.

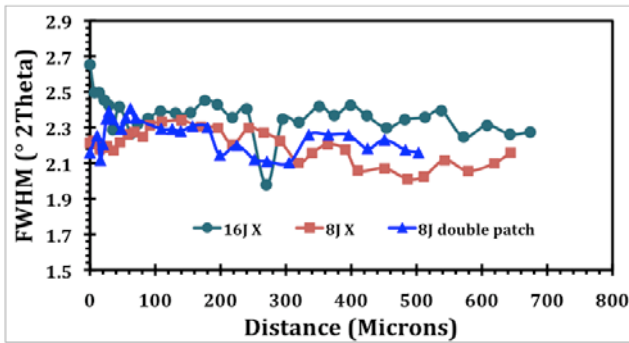
The residual stress data (Figure 18) reveals that there is only a small amount of stress relaxation in the near-surface and through-the-depth residual stress even after 100 h at 315°C. At 482°C, the stresses relax to about half of the initial value in 10 mins, but do not change further for longer times up to 100 h. The stresses also relax after aging at 538°C within an hour to more or less the same levels as the 482°C, 10 mins sample and then to about a third of the initial value after 24h. The near-surface FWHM in the aged samples remain more or less the same as the initial as-peened value at all temperature-time combinations, including 24 h at 538°C. This result suggests that the near-surface LSP-induced plastic strains are quite resistant to thermal relaxation.



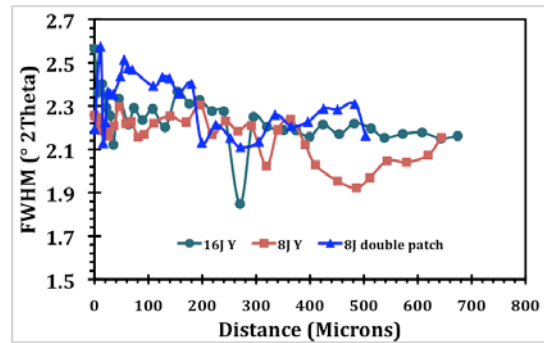
a



c



b



d

Figure 16: (a, c) Residual Stress and (b, d) Diffraction Peak FWHM in the X and Y Directions vs. Distance From Peened Surface of 8J, 8J (2 Hits) and 16 J Beam Energy LSP-treated Ti6242 Samples

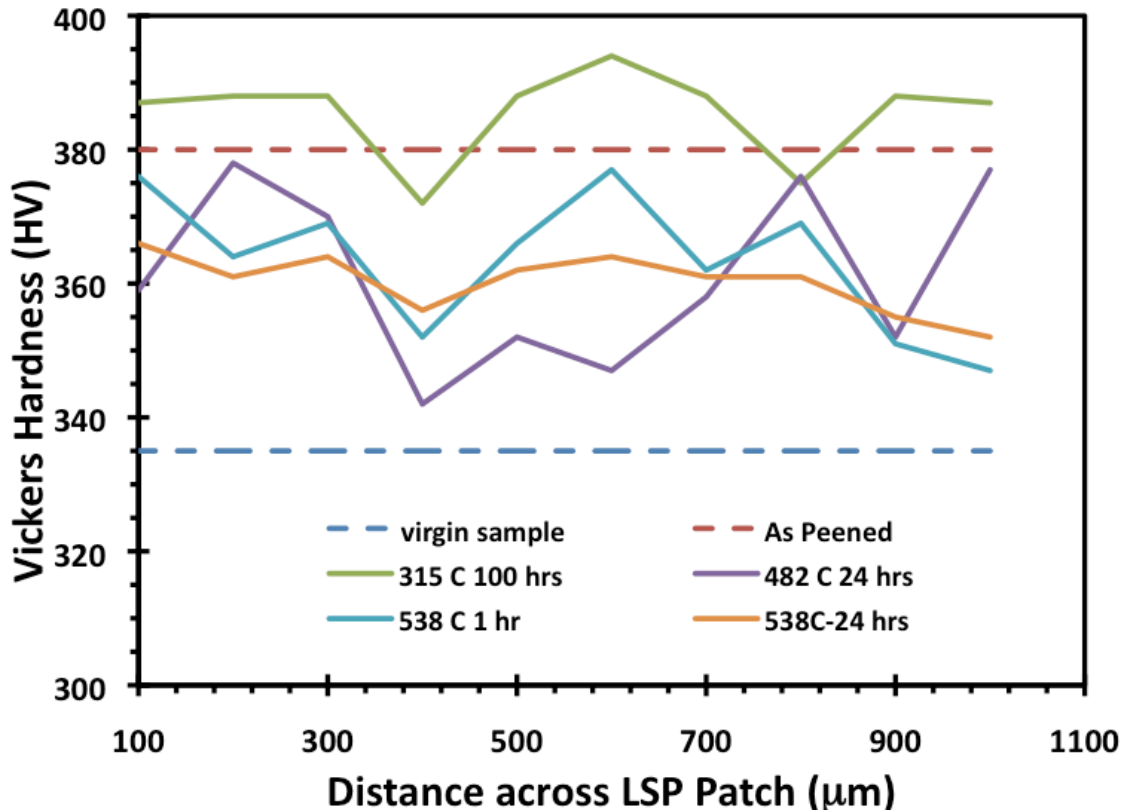


Figure 17: Vickers Hardness of Unpeened, LSP-Treated and LSP-Treated + Thermally Aged (315, 482, 538°C) Ti6242 Samples

The stress relaxation data from the Ti6242 alloy (Figure 18) were analyzed using the same Zener-Wert-Avrami formalism that was used in the case of the LSP-treated IN718 SPF alloy described earlier. The corresponding plot of $\log \ln(\sigma_o^{rs}/\sigma^s)$ (X direction data) vs $\log t_a$ in Figure 19(a) reveals a reasonable linear fit to the data at each temperature (though the number of data points at each temperature is limited; the value of the slope m at 315°C ($m \approx 0.14$) is somewhat lower than those at 482°C ($m \approx 0.3$) and 538°C ($m \approx 0.34$), which points to the sluggish kinetics of relaxation at the lowest temperature. A plot of $\log t_a$ to attain a given constant value of $\log \ln(\sigma^s/\sigma_o^{rs})$ is shown plotted vs $1/kT$ in Figure 19(b). A good linear fit to each data set is obtained, giving an activation enthalpy, ΔH of 114 kJ/mole (i.e. 1.37 eV). Similar analysis of the Y-direction residual stress data gave a ΔH value of 98.5 kJ/mole (or 1.185 eV). These values of ΔH are in the range of 90 to 160 kJ/mole reported for self-diffusion of Ti in Ti-base alloys from the literature. These results suggest that the residual stress relaxation in the LSP-treated Ti6242 alloy is caused by a creep-like mechanism involving rearrangement and annihilation of dislocations by climb.

LSP treatment of the Ti64 alloy was conducted to produce a number of single-dimple coupons in order to help in the finite element modeling and simulations of the thermal relaxation of the LSP-induced residual stresses. In this case, a beam energy of 3 J with three impacts at the same location were used. The surface and through-the-depth residual stresses were measured before and after thermal aging at 315°C, 350°C, 400°C, and 482°C for various exposure times. The experimental results are presented in the next sub-section with the FE analysis and simulations.

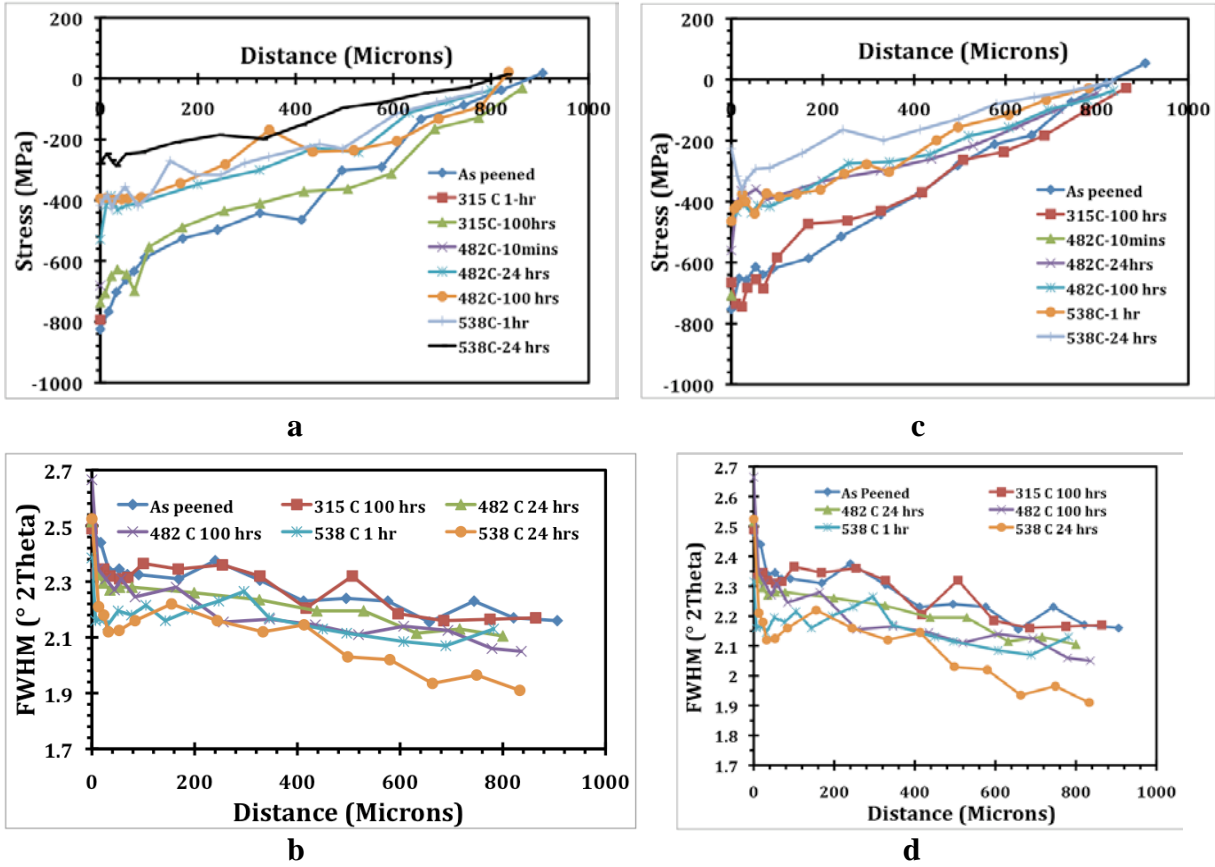


Figure 18: (a, c) Residual Stress and (b, d) Diffraction Peak FWHM in X and Y Directions vs. Distance from Peened Surface of 8J Beam Energy LSP-Treated Ti6242 Samples Aged at Different Temperatures (315, 482, 538°C) for Various Times

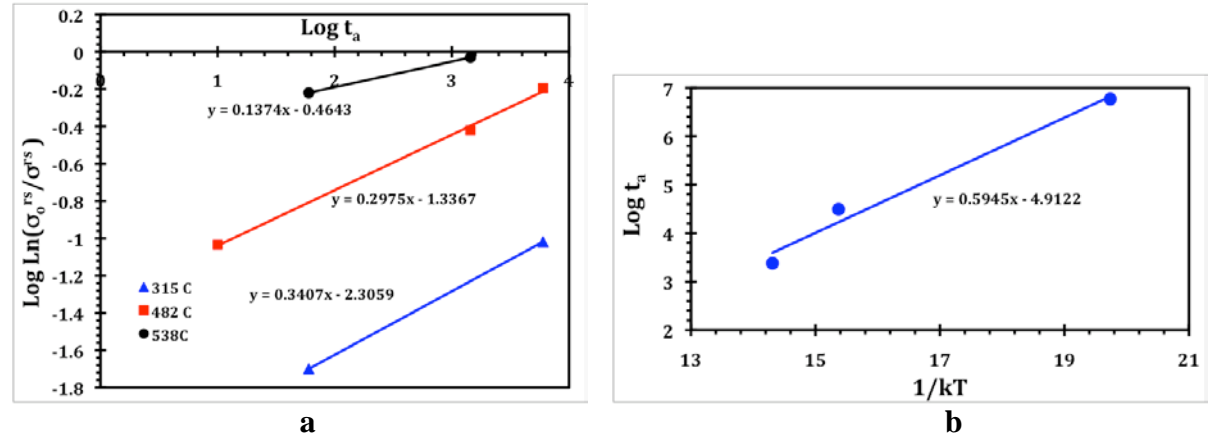


Figure 19: Plots of (a) $\log \ln(\sigma_0^{rs}/\sigma^{rs})$ vs. $\log t_a$ and (b) $\log t_a$ Corresponding to Specific Levels of Stress Relaxation vs. $1/kT_a$ for Determination of the Activation Energy Associated with the Relaxation Process in the Ti6242 Alloy

widely used for studying impact applications, and also available in many material model libraries in commercial FEM codes such as LS-DYNA that is used for this study. The JC model expresses the flow stress as,

$$\bar{\sigma} = [A + B\bar{\epsilon}^n][1 + C \ln(\dot{\bar{\epsilon}}^p / \dot{\epsilon}_0)][1 - T^{*m}] \quad (10)$$

where $\bar{\sigma}$ is the flow stress, $\bar{\epsilon}^p$ is the effective plastic strain, $\dot{\bar{\epsilon}}^p$ is the effective plastic strain rate, and $\dot{\epsilon}_0$ is reference strain rate. A , B , C , n and m are experimentally determined constants.

$T^* = (T - T_r) / (T_m - T_r)$, where T is the temperature in Kelvin and T_r , T_m are room temperature and melting temperature, respectively. The so-called ‘‘physically based’’ ZA model is based on crystal structure and dislocation mechanics. The flow stress has different expressions in terms of crystal structures (body centered cubic (BCC), face centered cubic (FCC), hexagonal closely packed (HCP)). The original expression for BCC metals is,

$$\bar{\sigma} = c_1 + c_2 e^{-(c_3 - c_4 \ln \dot{\bar{\epsilon}}^p)T} + c_5 (\bar{\epsilon}^p)^n \quad (11)$$

in which c_1 , c_2 , c_3 , c_4 , c_5 and n are model constants.

FE simulation of the LSP process using LS-DYNA is separated into two steps: In the first step, dynamic analysis is performed in which the laser shock loading is simulated until the plastic deformation terminates, typically in a few hundred nanoseconds. In the second step, static equilibrium analysis is carried out in which the state from the dynamic analysis is transferred into a restart analysis with a relatively larger time step and a suitable damping parameter to obtain a steady residual stress field.

3.1.2.2 FE Thermal Relaxation Simulation Procedure. After the steady residual stress field is obtained, mechanical loading is removed. Then the thermal loading condition is applied to the same FE model with the residual stress distribution from LSP as an initial condition, and thus the thermal relaxation process is simulated. This is achieved through a coupled thermal-structure analysis using LS-DYNA, using the implicit algorithm for both the thermal and structure analyses. The purely thermal loading condition is simulated by a convection boundary condition $\dot{q}'' = h(T - T_\infty)$, where \dot{q}'' is heat flux across the boundary, h is heat transfer coefficient of air, and T_∞ is the ambient temperature. The initial temperature of the specimen before thermal loading was taken to be room temperature.

As discussed previously, thermal relaxation of residual stress is essentially attributed to many different yet relevant mechanisms. Among them, the material softening at elevated temperatures is one key mechanism, especially for short-term thermal relaxation. As such, the material model must be able to capture the high-temperature effect on flow stress. The temperature dependencies of flow stress are different in the ZA model and the JC model. Some consider the ZA model to be a better description of the material behavior than the JC model because the mathematical form more accurately fits the material's strain rate hardening behavior, including the thermal coupling [58]. However, the ZA model is not recommended for temperatures above about one-half of the absolute melting temperature (965K). More importantly, since thermal relaxation is a quasi-static process, the ZA model with material constants determined from high strain rate high-temperature experimental data is not suitable to describe the temperature effect on flow stress at a quasi-static loading condition. As an example, the reduction in flow stress of Ti-6Al-4V at 10^{-4} /s strain rate is roughly 500 MPa when temperature increases from room temperature to 550°C [52], but from the ZA model (Equation (11)) it is only 30 MPa. On the other hand, although the JC model is a

phenomenological model, it is able to better represent the temperature dependence at both high and low strain rates. Therefore, the JC material model will be used in these thermal relaxation simulations, to keep the material model consistent during the switching from LSP simulation to thermal relaxation simulation. It is also adopted in LSP simulation.

3.1.2.3 IN718 SPF Alloy. The experimental details and results were described earlier. In the implementation for IN718 SPF the coupons with dimensions of 14 mm (length) \times 14 mm (width) \times 2 mm (thickness) were peened on a single side with three repetitions at the same location. The peening parameters were beam energy of ~ 8 J, ~ 2 mm spot diameter, and ~ 25 -30 ns pulse width for every shot. After peening, the coupons were exposed to 600°C and 650°C for times of 10 min, 1 hour, and 24 hours. Both as-peened and thermally relaxed residual stress distributions were measured at the spot center area with an x-ray beam diameter of 1 mm.

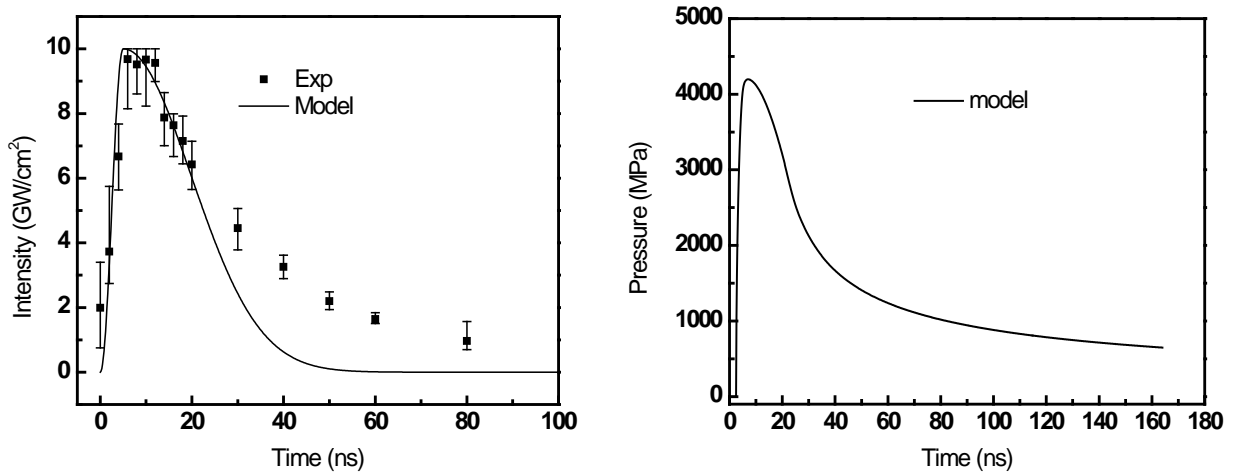


Figure 21: Intensity and Pressure Temporal Profiles Calculated from Pressure Model

The recorded laser intensity data during the LSP processing are shown in Figure 21, which are scaled to the same peak intensity ($8 \text{ J}/25 \text{ ns}/(\pi \times 0.01 \text{ cm}^2) \approx 10 \text{ GW}/\text{cm}^2$) for each shot, with error bars showing the variation. The SRT intensity profile assuming $10 \text{ GW}/\text{cm}^2$ peak and 5 ns rise time agrees well with the experimental data. The resulting pressure pulse calculated from the pressure model is also plotted in Figure 21, which is applied to the FE model (Figure 22) by assuming a uniform spatial distribution to simulate the LSP process. The FE model contains 115,002 nodes and 106,692 constant stress 8-noded solid elements. The whole LSP process is simulated through one dynamic analysis and one static equilibrium analysis for one shot, followed by another shot until all three shots are completed.

The as-peened residual stress from both FE simulation and experimental measurement are plotted in Figure 23. We can see that both the maximum residual stress and the compression depth are comparable, and that the stress distributions along the depth follow the same trend. The only discrepancy between simulation and experiment is that at the near-surface region (down to depth of 0.2 mm), the simulated residual stress profile is a little wider than experiment data. By simulation of LSP, we have also calibrated the parameters in the JC model for IN718. The original JC model parameters ($A = 1241 \text{ MPa}$, $B = 622 \text{ MPa}$, $n = 0.6522$, $c = 0.0134$) are taken from Ahmed et al. [59]. These parameters are usually determined using a Hopkinson bar test at strain rates up to $\sim 10^4/\text{s}$, which is much lower than the typical strain rate in an LSP process ($\sim 10^6/\text{s}$). Therefore such JC parameters (n , c) associated with the hardening effects have not accurately reflected the material response during LSP. After carefully adjusting the constants n and c , we were able to obtain

consistent residual stress as experiment data. The calibrated parameters for LSP simulation of IN718 are $A=1241$ MPa, $B=622$ MPa, $n=0.5$, and $c=0.035$. For thermal softening of flow stress, the parameter m was calibrated as 0.5 to match the high-temperature flow stress of IN718 at a quasi-static strain rate ($10^{-3}/s$) [60,61].

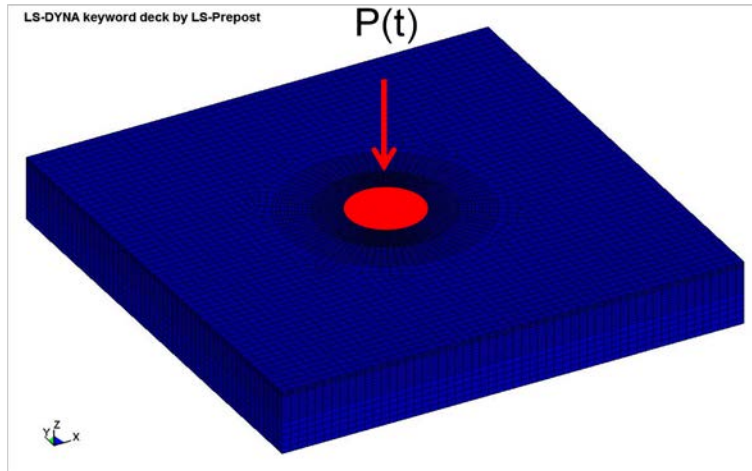


Figure 22: FE Mesh for LSP and Thermal Relaxation Simulation of IN718 and Ti-6Al-4V. during Thermal Relaxation Simulation, Thermal Loading Condition Was Applied at All Exposed Surfaces

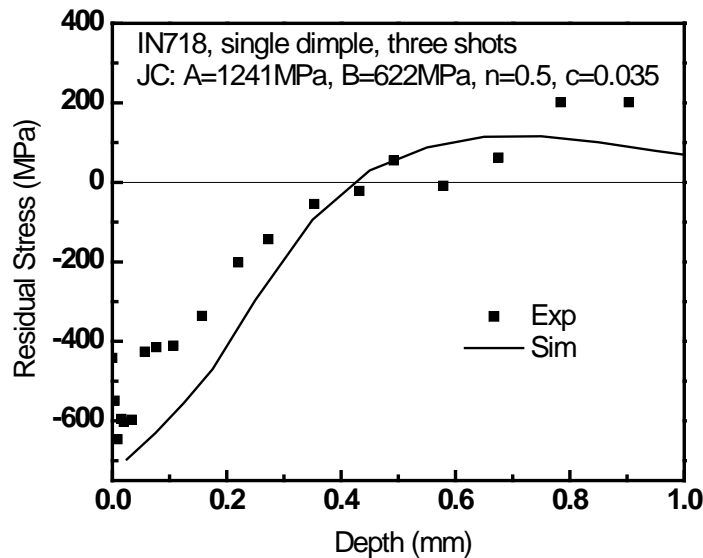


Figure 23: As-Peened Residual Stress Comparison in IN718 SPF Alloy Single-Dimple Three-Shots Coupon

Based on the results from the LSP simulations, thermal relaxation of residual stress due to high-temperature heating has been investigated. The comparison between experimental measurement and simulation results are illustrated in Figure 24. After 1 h exposure, the simulated maximum stress was relaxed from 697 MPa to 410 MPa and 376 MPa, at 600°C and 650°C, respectively. The magnitude of relaxation is similar to experiment data, in which the maximum stress was relaxed from 646 MPa to 470 MPa (600°C) and 496 MPa (650°C). Both experiment and simulation indicate that no obvious

relaxation was observed when the magnitude of residual stress was lower than ~ 300 MPa. After thermal relaxation, the depth distribution of residual stress becomes more uniform compared with the as-peened distribution. Thermal relaxation in IN718 as a function of exposure time at 600°C and

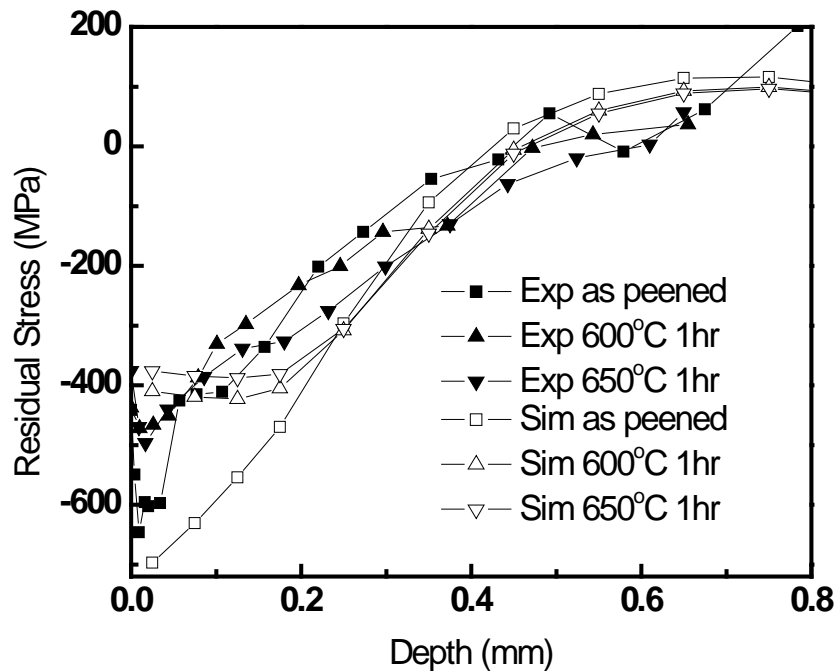


Figure 24: Comparison Between Experiment Data and Simulation Results of Thermal Relaxation of Residual Stress in LSP-Treated IN718 SPF

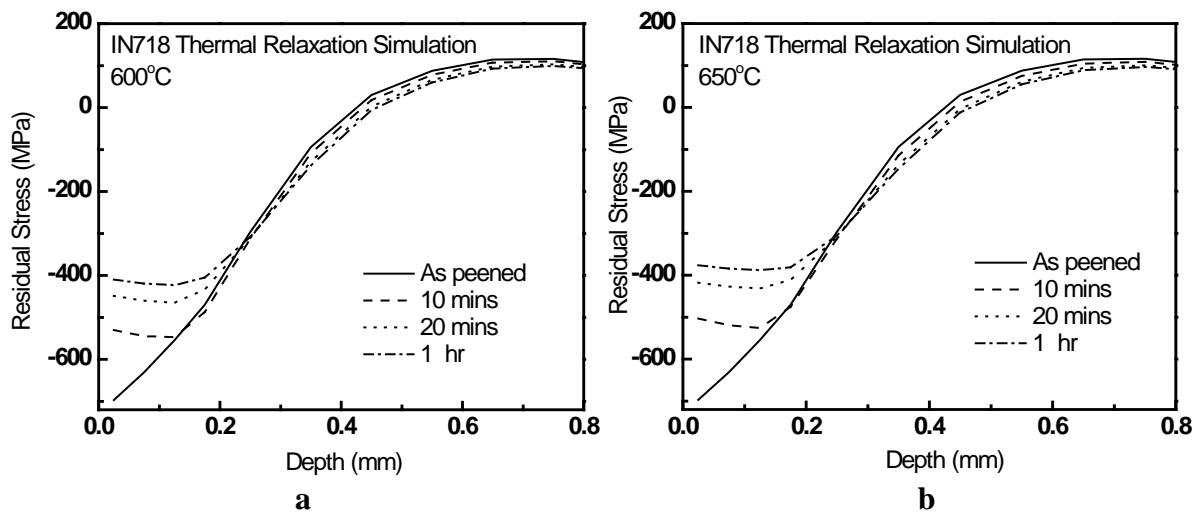


Figure 25: FE Simulation of Thermal Relaxation of Residual Stress in LSP-Treated IN718 SPF Alloy at (a) 600°C and (b) 650°C

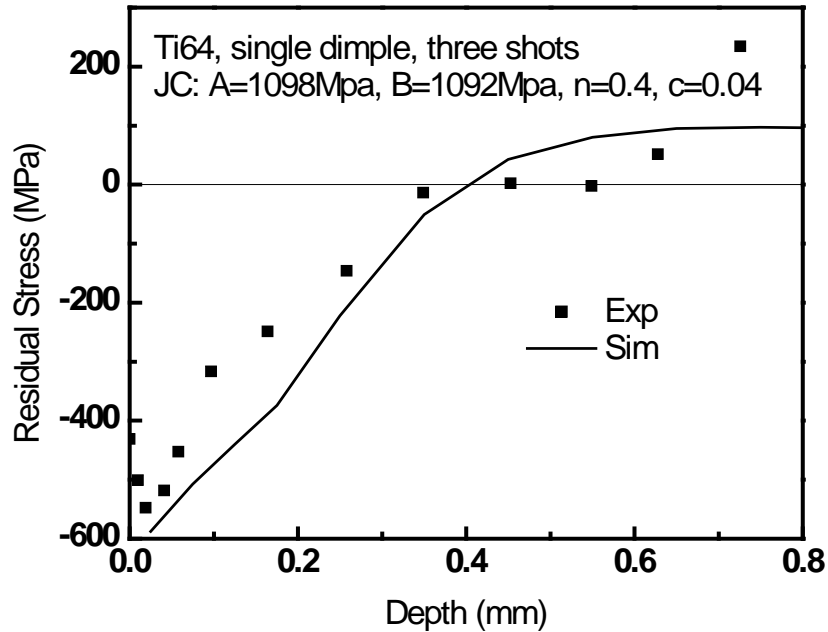
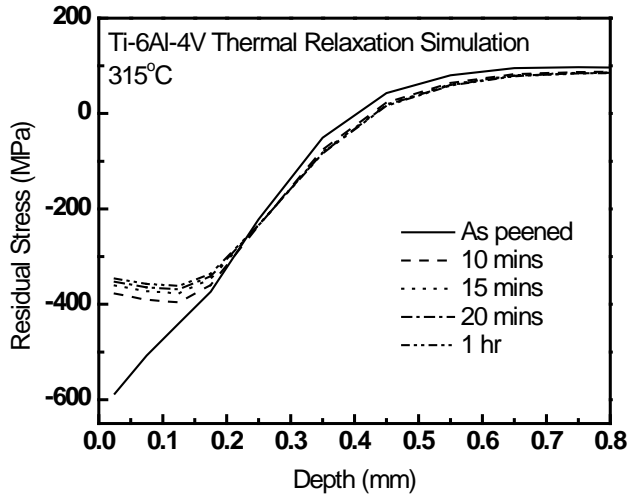


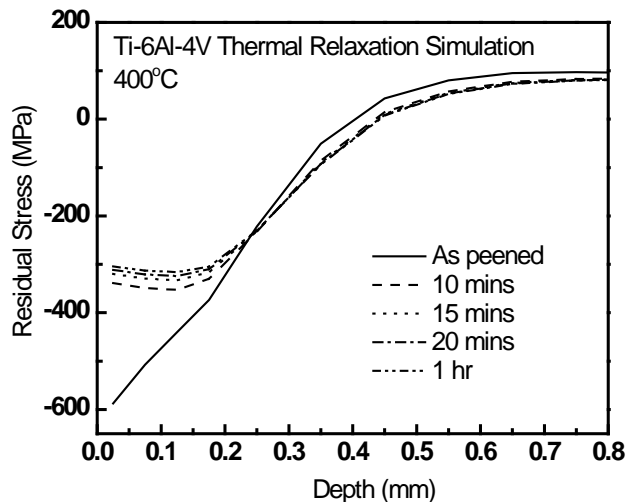
Figure 26: As-Peened Residual Stress Comparison Ti64 Alloy Single-Dimple Three-Shots Coupon

650°C are shown in Figure 25. It is observed that stress relaxation mainly occurs before 20 min, after that the residual stress tends to stabilize for a longer exposure time and thermal relaxation stops. It is consistent with the work of previous researchers [30,33,34], who found that a large proportion of the total relaxation occurred in the initial exposure period, normally between 3 min and 1h, followed by a stabilization of stress. In principle, more thermal relaxation is expected when the applied temperature is higher because the intrinsic yield stress becomes lower. In this study of IN718 SPF, the two temperatures investigated (600°C and 650°C) are very close, therefore the temperature effect is not very significant. However, we do find a little larger magnitude of relaxation at 650°C, as is evident when comparing Figure 25(b) with 25(a) and also in Figure 24.

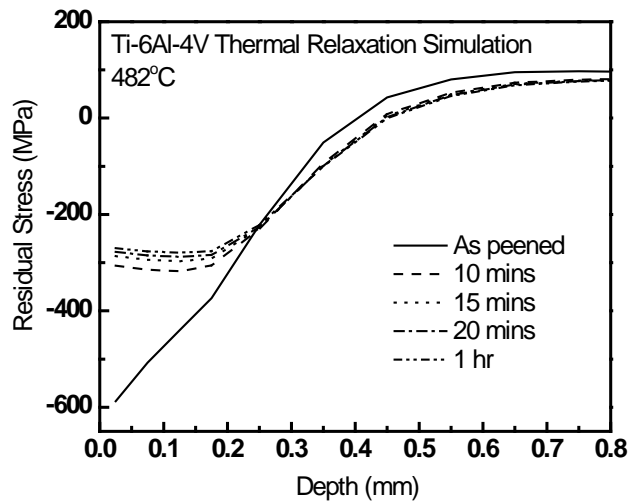
3.1.2.4 Ti-6Al-4V Alloy. The experimental procedure and processing parameters for the thermal relaxation studied in Ti-6Al-4V is the same as for IN718 SPF, except that the heating temperature was lower (315°C, 400°C and 482°C for Ti-6Al-4V). The pressure history and FEM model shown in Figures 21 and 22, respectively, were also used for Ti-6Al-4V. The as-peened residual stress from the FE simulation is plotted in Figure 26 along with the experiment data, from which a good agreement between simulation and experiment is achieved. The as-peened residual stress is a little lower than that of IN718. Following the same procedure as we did for IN718, the JC model parameters for Ti-6Al-4V are calibrated as $A=1098$ MPa, $B=1092$ MPa, $n=0.4$, $c=0.04$ and $m=0.2$, which are based on the original parameters taken from Lesuer [52].



a



b



c

Figure 27: Thermal Relaxation of Residual Stress Comparison in Ti64 Alloy Single-Dimple Three-Shots Coupon at (a) 315°C, (b) 400°C and (c) 450°C

The as-peened residual stresses induced by LSP and their relaxation as a function of exposure time at different temperatures is shown in Figure 27 (a-c). The maximum compressive residual stress, ~ 587 MPa, is observed at the surface, and the compressive layer induced by LSP is approximately 0.4 mm in this case. From Figure 26(a), we can see that maximal thermal relaxation occurred at the surface, i.e., the location of maximum residual stress. Approximately 36% of the peak residual stress was relaxed after 10 min exposure to 315°C. For laser shock peened Ti-6Al-4V, Vöhringer et al. [31] found no relaxation at the surface at 300°C, and progressively greater relaxation at higher temperatures ranging from 400°C up to 600°C. Lee and Mall [29] found about 11% relaxation at 100°C for 24 h, compared with 94% relaxation on exposure to 370°C for 24 h, at the specimen surface. Similar temperature effects are obvious for LSP-treated Ti64 specimens in this study. With an increase of temperature, the magnitude of surface stress relaxation is increased to 42% at 400°C (Figure 27(b)), and 48% at 482°C (Figure 27(c)).

The observed residual stress relaxation is thought to take place due to two main reasons: material softening at elevated temperatures and non-uniform distribution of as-peened residual stresses. When temperature increases, the intrinsic yield stress of Ti-6Al-4V becomes lower. As a result, the as-peened residual stresses with initial value far beyond this reduced yield stress will decrease to lower values closer to the reduced yield stress. It is expected that more thermal relaxation occurs when the applied temperature is higher leading to a more significant reduction in the yield stress, which is apparent from the comparison among Figure 27 (a) to (c). At the same time, regions with low as-peened residual stresses are not subjected to relaxation. From Figure 26, we see that the stress relaxation is negligible in the region deeper than ~ 0.25 mm where the initial residual stress is lower than ~ 250 MPa. Such that the thermal relaxation process rearranges the residual stress into a more uniform distribution as is most clear in Figure 27(c), however, the pattern of stress profiles are not influenced by relaxation. Figure 28 depicts the relaxed residual stress as a function of heating temperature. Square, circular, and triangular symbols represent residual stress at the surface, 0.1 mm depth, and 0.2 mm depth, respectively. Similar conclusions can be drawn: higher temperatures lead to more stress relaxation; lower initial stress is subjected to less stress relaxation; and relaxed stress exhibits more uniform spatial distribution.

From this study, we also find that stress relaxation mainly occurs before 10 min, after that residual stress tends to stabilize for a longer exposure time and thermal relaxation stops. It is also consistent with the work of [30,33,34] and the thermal relaxation behavior in IN718.

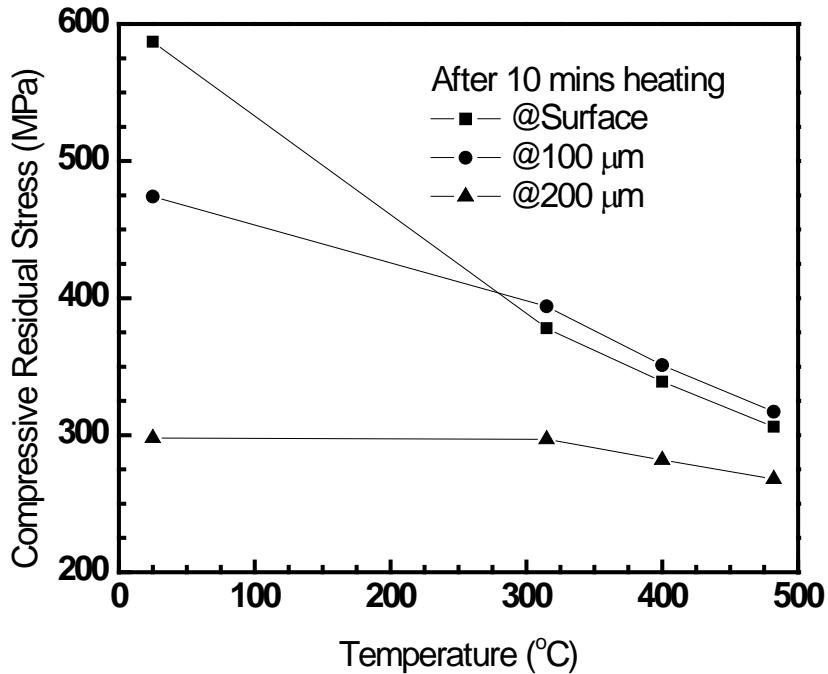


Figure 28: Relaxed Residual Stress (at Surface, 100μm, and 200μm) at Different Beating Temperatures in Ti-6Al-4V

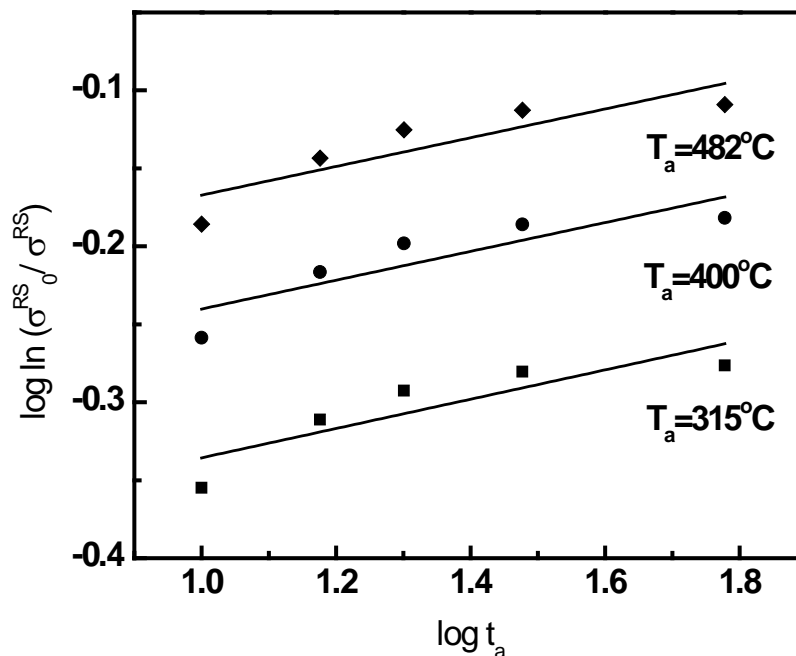


Figure 29: Simulation Results Showing Effect of Temperature and Time on Residual Stress Relaxation in LSP-Treated Ti-6Al-4V

To analytically describe thermal relaxation of residual stress, the Zener–Wert–Avrami model, which has been widely used in many studies for various materials, such as aluminum alloy AA6610 [62], nickel alloy IN718 [39,63], and titanium alloy TC4-DT [35], was used to analyze the residual stress

relaxation data in the LSP-treated IN718 SPF and Ti6242 alloys and was described earlier. The same approach was used for the Ti64 alloy data. Thus, Figure 29 shows a plot of $\log \ln(\sigma_0^{RS} / \sigma^{RS})$ versus $\log t_a$ at a given aging temperature T_a , which gives a straight line with slope m and intercept $m \log A$ and in which the data points are calculated from the simulation results. The m value resulting from the data fit at different temperature gives an identical value of 0.093. The intercepts of these straight lines give the values of A as a function of T_a , such that it is possible to estimate the activation enthalpy for the relaxation process by fitting A values to the equivalent form of Equation (6), $\ln A = \ln B - \Delta H / kT_a$. The activation enthalpy of the relaxation process for laser shock peened Ti-6Al-4V was determined from a plot of $\log t_a$ to achieve a certain level of relaxation as a function of $1/kT_a$ as $\Delta H = 1.0$ eV (83.14 kJ/mole), which is close to the reported value of 1.1 eV for thermal relaxation in Timetal 21S titanium alloy, and 1.4 eV for diffusion of Ti in β -Ti-20wt%V at 900°C [64]. The activation enthalpy of Ti-6Al-4V obtained here is much lower than 3.45 eV for IN 718 which was determined in our published work [39].

3.1.2.5 Ti6242 Alloy. FE simulations of thermal relaxation of residual stress in the LSP-treated Ti-6242 coupons with overlapped peening on dual side simultaneously was carried out. Details can be found in the experimental results described earlier. The dimension of the coupon is 30 mm \times 10 mm \times 4.2 mm. The LSP patch of 10 mm \times 10 mm is located at center, containing 81 shots. The peening parameters are ~ 8 J, ~ 2 mm spot diameter, and ~ 32 ns pulse width. The FE model shown in Figure 30 contains 72,409 nodes and 66,492 constant stress 8-noded solid elements, and the LSP patch location is represented by the fine mesh. In the simulation, a JC model is used for the Ti-6242 target material and the material parameters calibrated for Ti-6Al-4V are adopted since these two Titanium alloys have similar mechanical properties.



Figure 30: FE Mesh for Simulation of LSP and Thermal Relaxation in the Ti6242 Alloy Coupons

Thermal relaxation results from LSP-treated Ti-6242 are summarized in Figure 31. The simulated as-peened residual stress agrees well with experimental data, except for the point at the surface. A possible reason for this difference is that the experimental data was measured exactly at the surface while the simulation result was averaged at the surface FE element with a certain thickness. Both experiment and simulation results exhibit remarkable relaxation due to high-temperature heating. From Figure 30(b), we can see that the simulation results after 1h at 538°C are close to the experimental data, especially at the near-surface region. However, the simulation result

for 24 h heating (not shown since it is the same as 1 h heating result) is not consistent with experimental data. From the discussion above for IN718 and Ti-6Al-4V, it appears that after certain exposure time (usually 30 min to 1h), thermal relaxation due to material softening mechanism at elevated temperatures will stop and stress stabilization is achieved. In contrast, experimental data still shows a certain relaxation after 1 h, although not very significant. This long-term relaxation is thought to be dominated by creep-controlled mechanism, which may not be described appropriately by the material model adopted here. For short term thermal relaxation, the FE simulation presented here using the JC model is justifiable, whereas for fully understanding thermal relaxation accounting for long term relaxation ($t \gg h$), a new material model including both material softening and creep relaxation should be developed in future work.

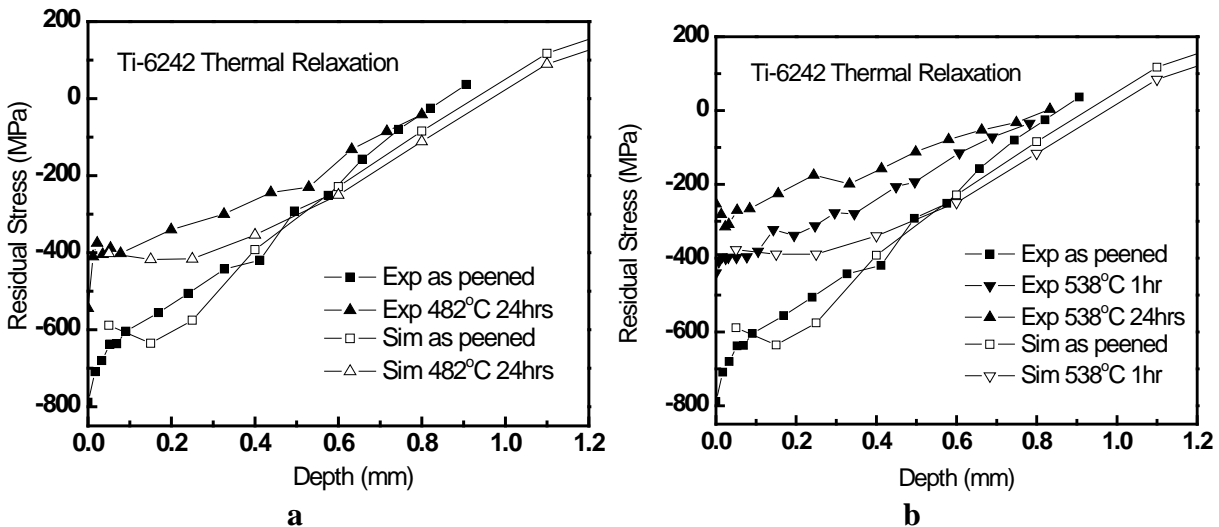


Figure 31: Comparison of Experimental and FE Simulation Results of Thermal Relaxation of Residual in LSP-Treated Ti6242 Alloy at (a) 482C and (b) 538C

3.2 LSP Process Simulations for Optimizing LSP Treatment and Effects on Fatigue Behavior of Ti6242 Alloy

3.2.1 Initial LSP Treatments and Three-Point Bend Fatigue Tests

As described in Section 4.1.1.2, LSP treatments on the Ti6242 alloy were conducted for characterizing and modeling the thermal relaxation of residual stress. Characterizing the fatigue behavior of surface-treated materials presents a special challenge because these properties can be affected not just by the state of residual stress, microstructure, and other features at the surface, but also by the presence of balancing tensile residual stresses in the interior of the material. Three- or four-point bending fatigue tests have an advantage, because the impact of near-surface residual stresses (compressive or tensile) and microstructure can be assessed more easily. However, special considerations must to be given to the design of suitable coupons. Thus, initially two types of coupons were fabricated for three-point bending (3PB) tests to study the effect of LSP and post-LSP thermal aging on the fatigue properties. The first set of coupons were 60 mm long x 10 mm wide x 4.2 mm thick (Figure 32) with an LSP-treated (power density 8 GW/cm²) patch measuring 12 mm x 10 mm was produced on one surface. The static and fatigue properties (S-N curve) were determined on unpeened and peened samples with the LSP-treated surface on the side opposite to

the direction of central loading, i.e. the tensile side. The second set of coupons were made the same way, but had a thickness of 2 mm. The static and fatigue properties of these were also determined.

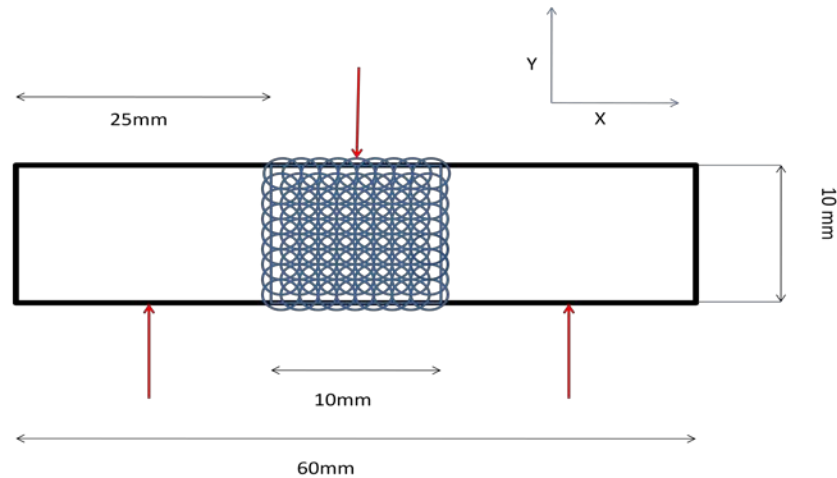


Figure 32: Geometry and Dimensions of Third Set of 3PB Test Coupons (2mm Thick) for Studying the Effects of LSP on the Fatigue Properties

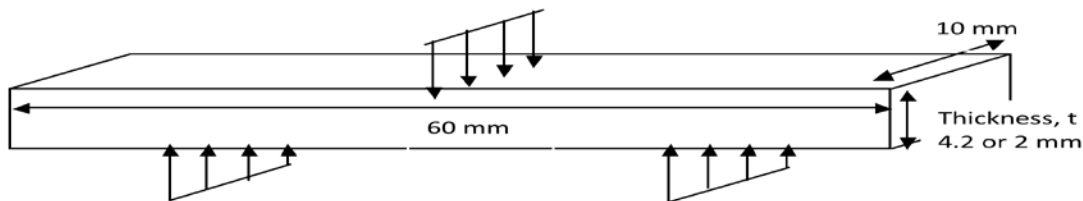


Figure 33: Geometry and Dimensions of the Initial Sets of 3PB Test Coupons for Studying the Effects of LSP on the Fatigue Properties. Note: Coupon Has a 10mm X 10mm LSP-Treated Area in the Middle of the Bottom/Tensile Surface

Fatigue tests on these coupons at the range of load/stress levels to generate S-N curves revealed that the LSP-treated coupons generally failed, surprisingly, after a shorter number of cycles compared with the unpeened coupons. Examination of the failed samples revealed that, in a few cases, premature failure was related to the presence of bad/naked spots (caused by blowing-off of the ablative tape) on the LSP-treated surface, where cracking was initiated. In other cases, the reasons for premature failure were not obvious. It was thought that perhaps the peening sequence used may have produced localized tensile residual stresses on the surface and along the edges of the coupons, where early crack initiation would be facilitated. Subsequently, we decided to focus on 2 mm thick coupons, LSP-treated on both surfaces, with the specimen resting on the bottom rollers along the thickness edge and the sample width and applied load parallel to the peened surfaces. Details of the geometry, dimensions, and 3PB test configuration are shown in Figure 33.

Three-point bend fatigue tests on the coupons with the above geometry (Figure 33) again showed that the number of cycles to failure were lower in the LSP-treated coupons compared with the unpeened coupons. It was thought that perhaps the through-thickness compressive residual stresses sought by double-sided peening were not achieved and early crack initiation and growth occurred by a tunneling process because of the presence of the balancing tensile residual stresses in the central portion of the coupons adding-up to the tensile stresses from the applied load along the bottom surface. Thereafter, a fourth set of 60 mm long x 10 mm wide x 2 mm thick coupons

similar to those in Figure 33, but with an EDM-generated notch of radius $\sim 170\ \mu\text{m}$ and $250\ \mu\text{m}$ depth along the middle of bottom edge into the LSP-treated area were fabricated. The purpose of the notch was to ensure that crack nucleation occurred at the middle of the bottom edge of the sample. Fatigue tests on notched unpeened and peened coupons were conducted at a range of stress levels and the S-N curve established. Based on the results that were obtained, which are described in a subsequent section, it was felt that LSP process simulations needed to be performed to optimize the LSP treatment parameters for improved fatigue life, as described below.

3.2.2 Rationale for LSP Process Simulations for Optimizing LSP Treatment

LSP is an engineered process, in that a large number of parameters have to be optimized to achieve the sought after improvements in component fatigue life. The most important process parameters include the diameter and energy of the laser beam, pulse width, the number of successive impacts, and the sequence of impacts used to generate a treated region with overlapped spots. The magnitude of the generated residual stresses and their depth is governed by the LSP parameters and the mechanical properties of the material undergoing LSP. Also, the geometrical constraints of the component affect the distribution of the residual stresses. To obtain improvement in fatigue life, distribution of the LSP induced residual stresses is very important as it controls fatigue crack initiation and propagation. Considering the amount of time required for LSP processing and fatigue testing of LSP-treated components, it makes sense to perform simulations of the LSP process to predict the residual stress distribution. This type of simulation can guide designers to choose the ideal processing parameters.

As mentioned previously, LSP simulation can be effectively performed using FEM. Braisted et al. [44] reported the first simulation of LSP using FEM. In recent years, few authors have reported simulation of LSP keeping the goal of process parameter optimization. Arif et al. [8] developed a non-linear finite element model and coupled it with a wave propagation algorithm to calculate LSP induced residual stresses. Yang et al. [66] performed LSP simulation on 7050-T7451 aluminum alloy using software package ABAQUS [67]. Warren et al. [49], performed massive parallel simulations of LSP to study the effect of spot diameter, laser energy and the number of LSP passes on residual stresses generated in single-shot experiments. Recently, Singh et al. [68], applied optimization techniques to obtain LSP parameters given a desired residual stress profiles.

However, most of the previous studies have focused on optimizing the performance at a single LSP spot location. For industrial applications, LSP is performed in patches, which constitute multiple laser shots performed with some overlap percentage. Overlap is necessary to obtain a uniform residual stress distribution [69]. For thin components, geometry effects play an important role in the final residual stress distribution. Dual side peening on thin components might generate tensile stresses on the edges, which is also called an edge effect (this is shown later in this section). The sequence in which multiple shots are applied can dramatically affect the residual stress distribution, which eventually determines the fatigue life. If the processing is not done properly, the fatigue life may be less than the untreated sample. Therefore, it is important to have an optimized set of laser parameters as well as the sequence in which LSP is performed to obtain desired improvement in fatigue life. None of the reported literature has dealt with optimal sequence of shots for the LSP patch. The goal herein is to obtain the optimal patch sequence for a given loading condition, material and geometry.

This goal is realized by performing 3D non-linear finite element simulations of the LSP patch. Focus is on the Ti-6242 alloy thin coupon, subjected to 3-point bending loads. Different sequences are used in simulations to study the residual stress distribution on the surface as well

through the thickness of the thin coupon. Through thickness residual stress distribution is important to prevent crack initiation and propagation. Finally, an optimal set of laser parameters and patch sequence is presented, which gives the maximum surface compressive stresses while maintaining the through thickness compression.

3.2.3 LSP Modeling and Simulation Procedure

In the following, the coupon geometry and dimensions utilized are first described, followed by a detailed description of the LSP modeling and simulation procedure used for predicting the residual stress distributions within and outside the treated area of the coupon.

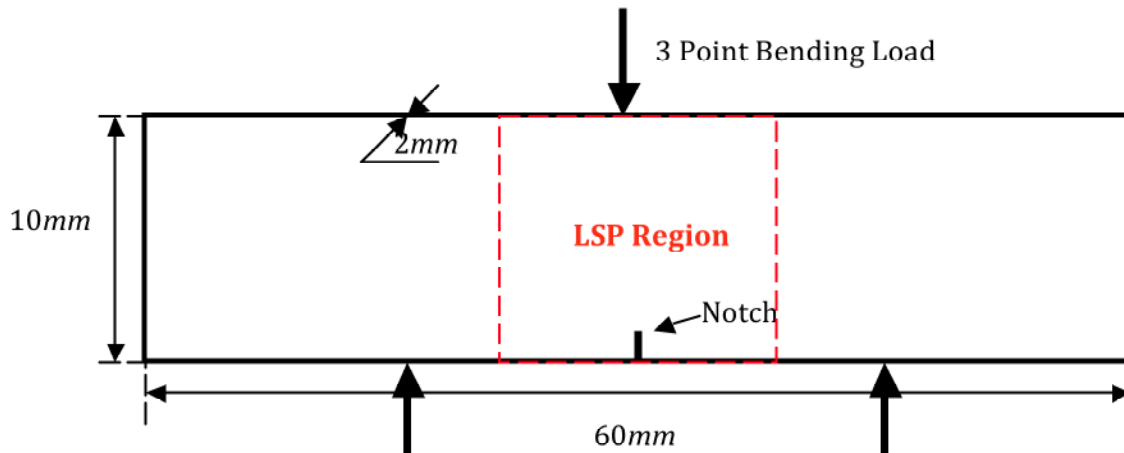


Figure 34: Schematic of the Ti6242 Coupon Used for the LSP Simulations

3.2.3.1 FE Model. Simulations are carried out on a coupon (see Figure 34) with dimensions 60 mm (length) \times 10 mm (width) \times 2 mm (thickness). The coupon is supposed to be tested under a 3 point bending fatigue load at an R ratio of 0.1 with a notch machined using wire EDM after the LSP processing. Considering the nature of the 3-point bend loading and stress concentration induced by the notch, LSP should be performed in the region indicated in Figure 34. Based on this, an FE mesh is generated using the commercial package HyperMesh, which is shown in Figure 35.

□ LS-DYNA keyword deck by LS-PrePost

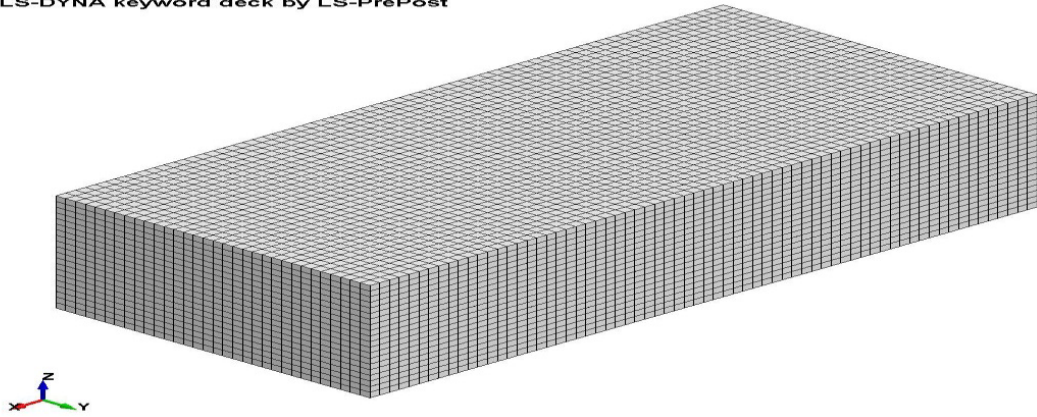


Figure 35: Part of the Complete Mesh for the Ti6242 Coupon

To reduce the computational time, very fine element size (0.1 mm by 0.1 mm) is restricted to the region of LSP. The mesh resolution was gradually increased away from the LSP region. The complete mesh has 377,800 8-noded brick elements and 402,381 nodes.

3.2.3.2 LSP Simulation. The LSP simulation procedure using FEM is illustrated in Figure 36.

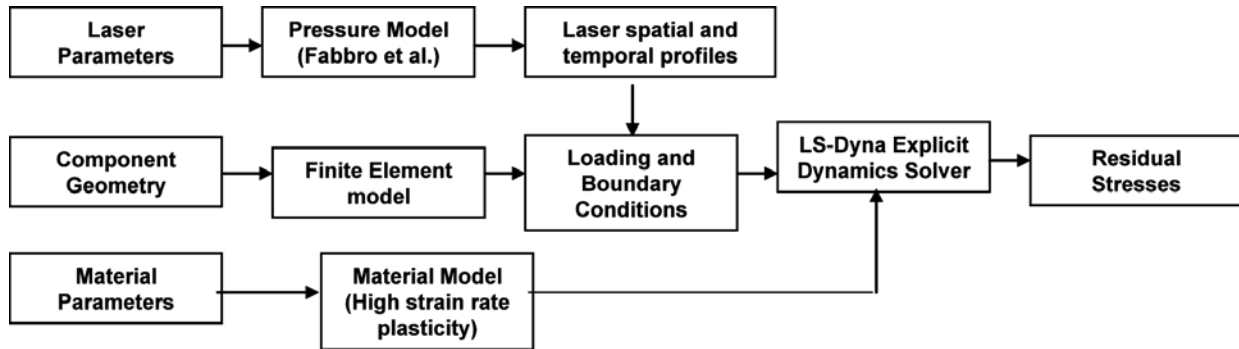


Figure 36: Flowchart of LSP Simulation Procedure

3.2.3.2.1 Pressure Model. In LSP, laser energy is converted into mechanical pressure through complex interactions between the laser beam, opaque material (tape in this case) and confinement medium (water). To obtain the mechanical equivalent of the laser energy as a function of spot diameter, pulse width, and energy of the laser, a pressure pulse model proposed by Fabbro et al. [50] is implemented. From the given laser parameters, peak power density (PPD) is calculated, which is used to fit a short rise time (SRT) laser intensity profile. This profile is then used as the input for the pressure model to obtain the pressure pulse temporal profile. Spatial variation in the laser intensity can be further applied, however, in this study a uniform spatial distribution of the laser intensity is assumed. The combination of spatial and temporal pressure profiles are then applied to a finite element model. Figure 37 shows a sample pressure temporal profile for the given laser energy of 2 J, pulse width of 27 ns, and a 2 mm spot diameter.

3.2.3.2.2 Material Model. During LSP, materials are subjected to very high strain rates (on the order of $10^6/s$). At such high strain rates, materials show rate dependent strain hardening and thermal softening due to heat generated during plastic deformation. In the literature, various models have been proposed for modeling such high strain rate behavior of materials. These models include

Johnson-Cook (JC) [51,52], Zerilli-Armstrong (ZA) [53,54], modified ZA [55], mechanical threshold stress (MTS) [70], and Khan–Huang-Liang (KHL) [71]. Zhou et al. [39] applied the JC model for predicting the LSP induced residual stresses in Inconel 718. It was shown that a well-calibrated model can predict the residual stresses accurately. Amarchinta et al. [72] performed an optimization study to obtain the material parameters needed in JC, ZA and KHL models for accurate predictions of residual stresses in Ti-6Al-4V alloy and Inconel 718. The goal of this was to study the residual stress distributions and the effect of different shot sequences, with focus on the Ti-6242 alloy. Meyer et al. [55] discussed a few limitations of the JC model for modeling the nonlinear strain hardening behavior of the Ti-6Al-4V alloy. They recommended use of the ZA model for titanium alloys. However, the ZA model does not consider the dependence of shear modulus on pressure and temperature. Considering this, the ZA model combined with a pressure and temperature dependence model given by Steinberg et al [74] is used in this study (see equation (12)).

$$\bar{\sigma} = \left[A + B e^{-(\beta_0 - \beta_1 \ln \dot{\bar{\epsilon}}) \cdot T} + C \bar{\epsilon}^n \right] \frac{G(P, T)}{G_0} \quad (12)$$

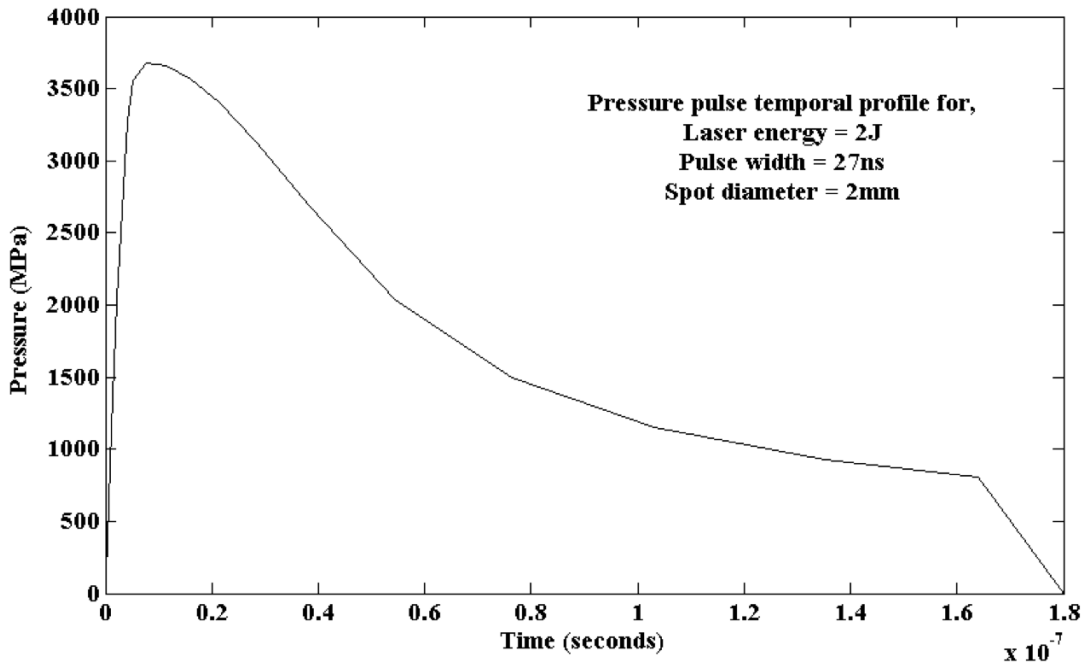


Figure 37: Temporal Profile of the Pressure Pulse Generated Using the Pressure Model

where $\bar{\sigma}$ is effective stress, $A, B, C, n, \beta_0, \beta_1$ are material parameters, T is Temperature, $\dot{\bar{\epsilon}}$ is Effective visco-plastic strain Rate, $\bar{\epsilon}$ is effective visco-plastic strain, G_0 is shear modulus at room temperature, and P is pressure. $\frac{G(P, T)}{G_0}$ gives the variation in shear modulus as a function of temperature and pressure. The ZA model is available in LS-DYNA. However, the available material model does not have pressure dependence on the shear modulus. Therefore, a user define code is written to implement the proposed model in LS-DYNA. Material parameters of $A = 810$ MPa,

$B=1800$ MPa, $C=250$ MPa, $\beta_0 = 0.009$, $\beta_1 = 0.0005$, and $n = 0.5$ are taken from [73]. The model parameters related to pressure are taken from [74], which are given as $G_0 = 43.4$ GPa, $\frac{G'_p}{G_0} = 11.5$ TPa⁻¹, and $\frac{G'_T}{G_0} = 0.62$ kK⁻¹.

3.2.3.2.3 Solution Procedure. The FE model of the coupon with applied pressure profile is then solved using the LS-DYNA explicit dynamics solver, which is linked to the user defined material model. LSP simulation is separated into two stages. In the first stage, the dynamic response of the material under the action of LSP-induced intensive shock pressure is obtained. Interaction of the shock waves is effectively captured by the explicit dynamics scheme. This stage is executed up to a point where additional load will not produce any plastic deformation. In the second stage, travelling elastic waves in a component are allowed to damp using the dynamic relaxation scheme. Artificial damping is introduced to obtain a steady state. After completion of this simulation, residual stresses are extracted at the desired location. For a multi-shot analysis, the two stages are repeated using the restart capability of the LS-DYNA software. The pressure pulse is effectively transferred onto the FE model as per the sequence of the LSP patch.

3.2.4 Simulation Results and Discussion

Different sequences of laser shots are explored to obtain the optimal distribution of the residual stresses. Also, the effect of different laser parameters on the residual stress distribution is studied. Results for the residual stresses in the component for each sequence are given below.

3.2.4.1 Patch of 12 mm by 10 mm Size.

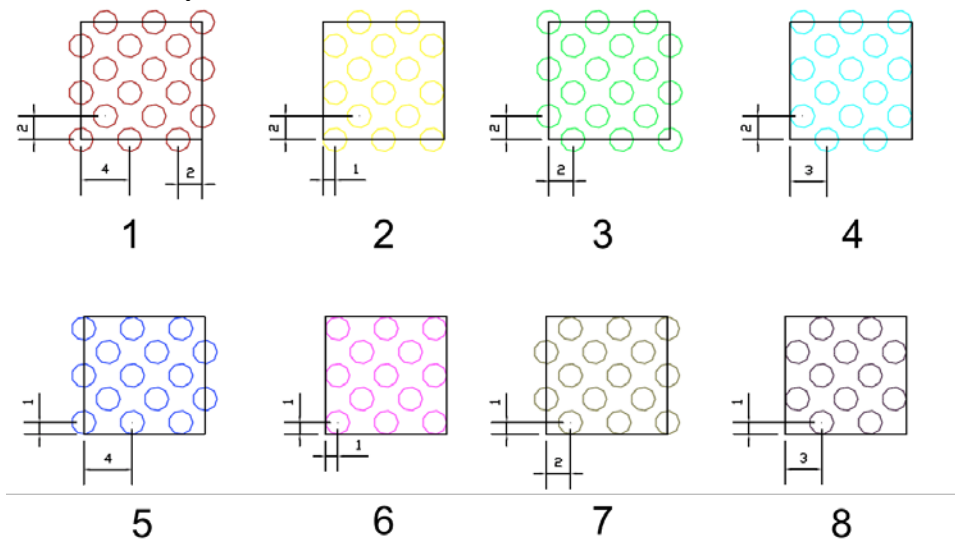


Figure 38: LSP Spot Sequence for 12mm x 10mm Patch in Ti6242 Coupon

A region of 12 mm by 10 mm was processed with LSP. This region is centered lengthwise at the location where the notch will be machined by EDM after the LSP treatment. Refer to Figure 34 for the notch location and LSP region. 50 % overlap between the adjacent laser shots in both length and

width directions was used. It is desired to have compressive residual stresses throughout the thickness of the coupon. To achieve this goal, dual side laser peening was used in the simulations. Considering the thickness of the coupon (2 mm), low energy values were used for these simulations. High-energy dual side processing on thin samples might produce center cracking. The first simulation was performed with laser energy of 2 J, pulse width of 27 ns and 2 mm spot diameter. Spot sequence was designed to have minimal tape changes during the LSP processing. Figure 38 shows the spot sequence used for this simulation. Single pass dual side LSP simulation was performed.

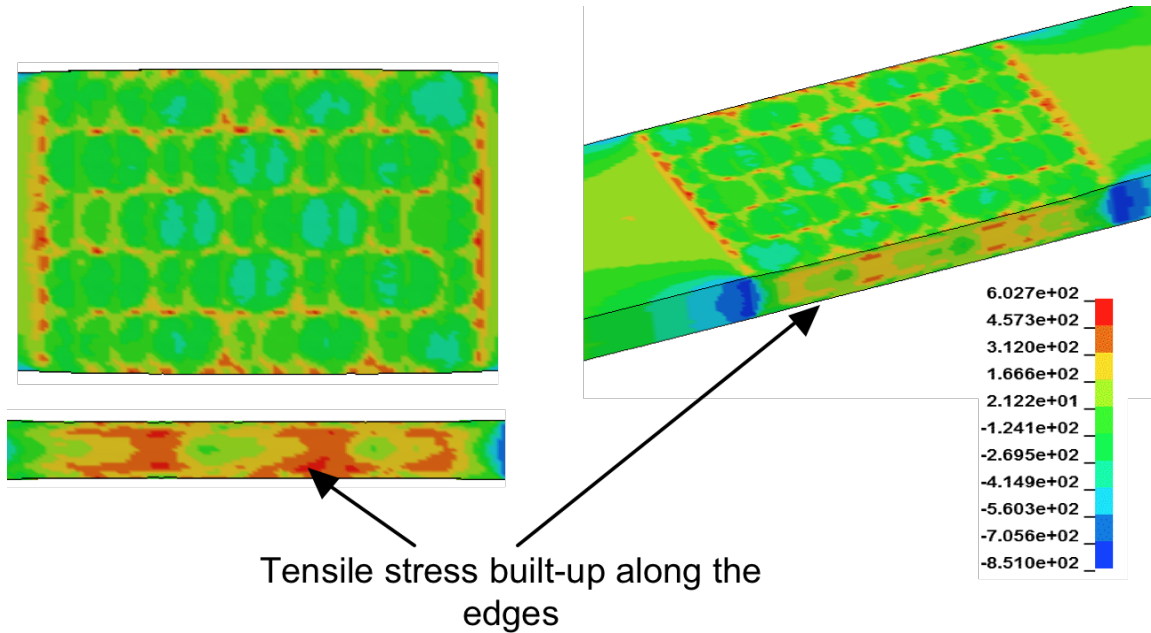


Figure 39: Contour Plot of the Axial Stresses. Note Build-Up of Tensile Residual Stresses Along the Edges of the Thin Ti6242 Coupon

Contour plots of the axial stresses (along the length of the coupon) as obtained after simulating this sequence are shown in Figure 39. To understand the residual distribution through the coupon thickness, residual stresses are extracted from the final solution at the two locations as indicated in Figure 40. The first measurement is averaged over the 2 mm by 2 mm area centered at the patch center. The second measurement is averaged over the 0.6 mm by 0.6 mm area covering the region in and ahead of the notch location.

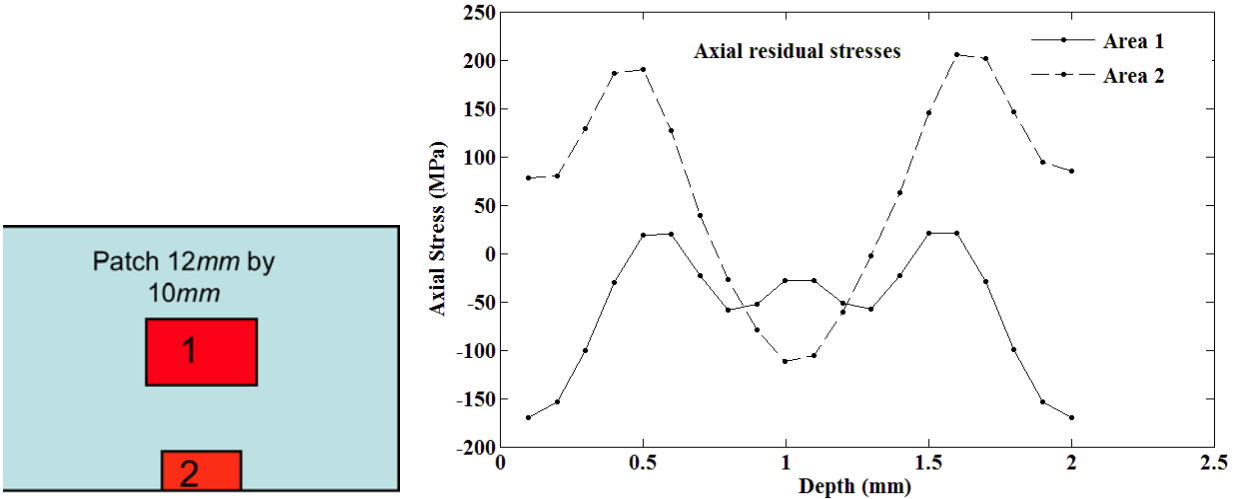


Figure 40: Residual Stress Profiles Obtained From LSP Simulation of 12mm x 10mm Patch in Ti6242 Coupon

It can be seen in Figure 40 that the 12 mm by 10 mm patch helps to generate through thickness compression at the patch center. However, the area near the edge of the patch, where the notch will be machined, has tensile stresses on the surface and through the thickness. This sequence would help crack initiation and propagation, which is not desired.

3.2.4.2 Patch of 8 mm x 5 mm Size. It is important to reduce the tensile stress build up along the edges of the patch, which can be realized by reducing the patch area and adjusting the shot sequence within the patch area. In the 3PB setup, the upper half of the coupon from the neutral axis will always experience compressive stresses, and thus need not be processed with LSP. Considering this, the patch area was reduced to 8 mm by 5 mm with the focus on the lower half, covering the region around the notch. Two types of sequences were simulated. Results are discussed below.

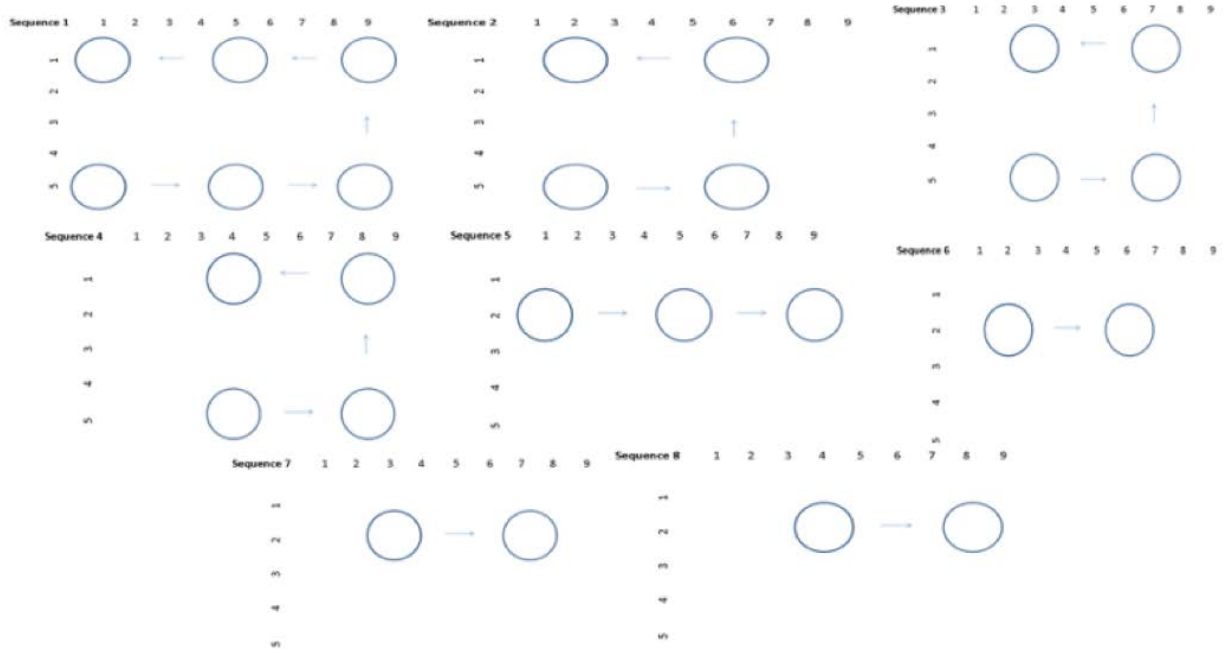


Figure 41: Spot Sequence I for 8mm x 5mm Patch in Ti6242 Coupon

3.2.4.2.1 Spot Sequence I. This spot sequence was similar to the one used for 12 mm by 10 mm patch. It was designed to have minimal tape changes. Figure 41 shows a schematic of different spot

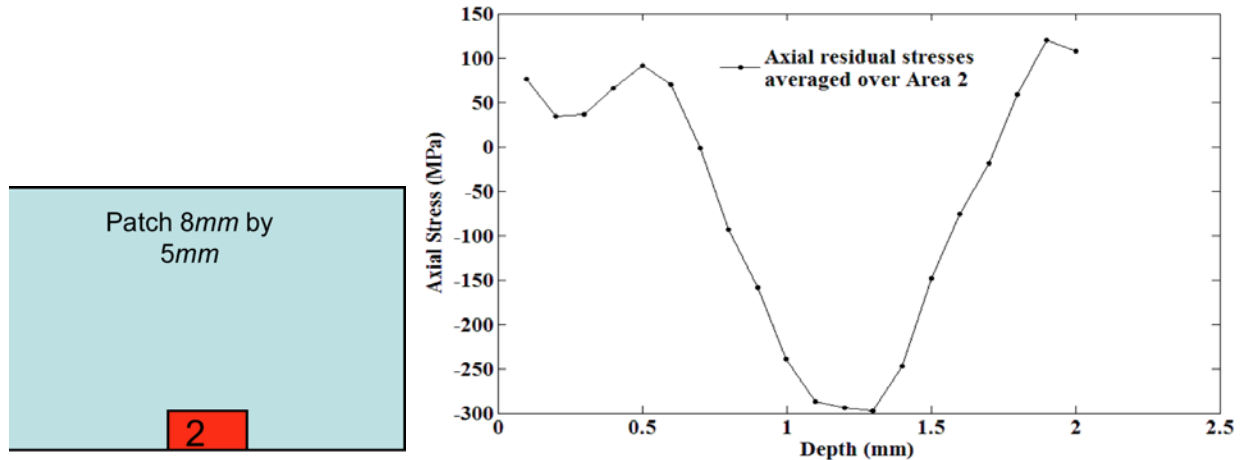


Figure 42: Residual Stress Profiles Obtained From LSP Simulation of 8mm x 5mm Patch

sequences. Laser parameters are the same as used in section 2.2.4.1. As mentioned earlier, the focus was on getting through compression in 'area 2', which is critical in terms of crack initiation and propagation from the notch. Figure 42 shows the residual stress profile averaged over area 2 (refer Figure 40 for area 2).

Relative to the residual stress profiles described for the 12 mm x 10 mm patch in section 3.2.4.1, the magnitude of the tensile stresses in area 2 is reduced. However, the short patch using this sequence is still not able to deliver through thickness compression near the notch area.

3.2.4.2.2 Spot Sequence II. Spot sequence I, used earlier for the smaller LSP patch, was modified so that the last shots in the sequence were along the lower edge of the coupon, which contains the notch. The LSP was performed row by row as shown in Figure 43, with the first row of shots starting inside the coupon and moving out towards the edge.

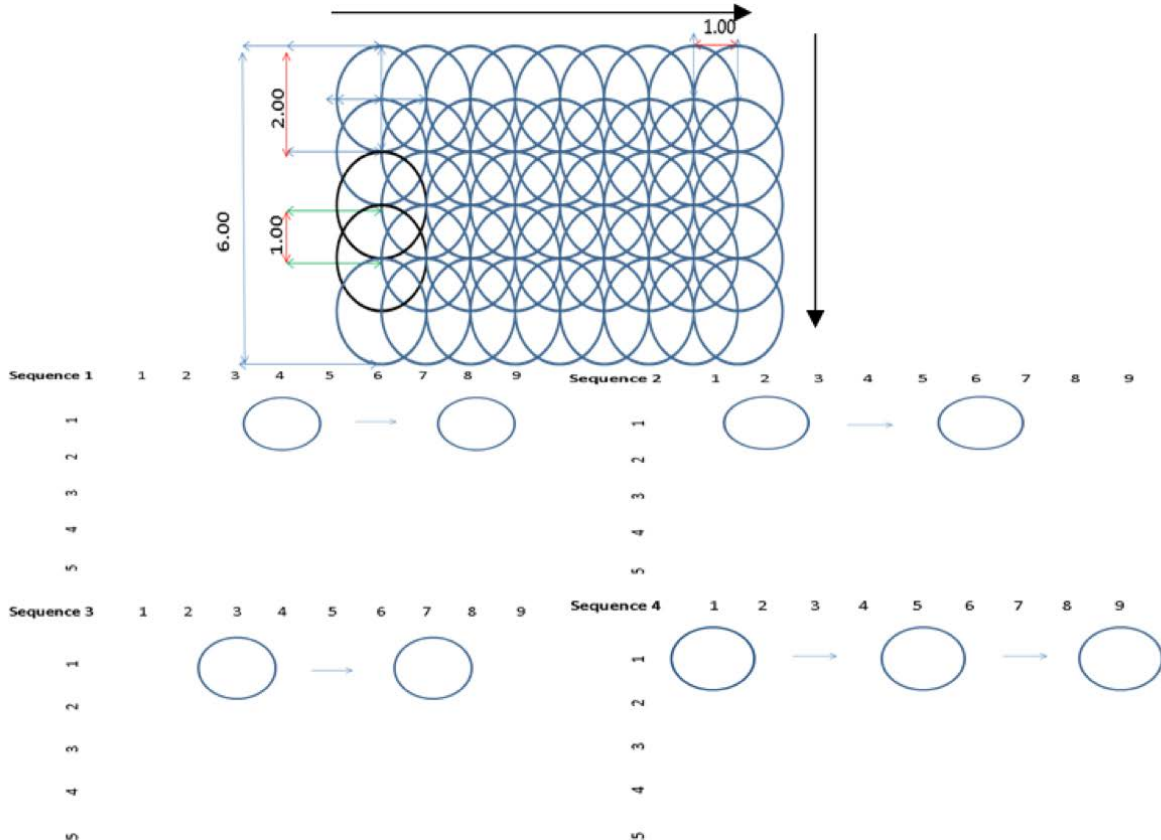


Figure 43: Spot Sequence II for 8mm x 5mm Patch in Ti6242 Coupon

Within each row, the sequence was designed to have the last shot at the center of the row. Two passes of LSP patches were simulated, keeping the laser parameters the same as earlier studies. Figure 44 shows the residual stress profiles averaged over three different areas along the potential crack growth path. Each of the areas 2, 3 and 4 (Figure 44) are 0.6 mm by 0.6 mm. As seen in Figure 44, the through thickness compression is obtained with the current sequence in area 2 and area 3. This should ideally help in forestalling fatigue crack initiation and propagation. However, in area 4, there are still tensile stresses at a few locations through the depth. To push these tensile stresses further away from the crack path, additional simulations were performed with the laser energy increased from 2 J to 3 J. The pulse width and spot diameter were kept the same. Two passes of LSP patches were simulated. Figure 45 shows the residual stress profiles obtained with the modified laser parameters. As expected, through thickness compression is obtained in areas 2, 3 and 4 with an

increase in the laser energy. Almost uniform surface stresses are obtained in all the areas with the current laser parameters. It is also important to note here that, the magnitude of the compressive stress on the surface in area 2 has not shown tremendous increase compared with the 2 J results. This suggests that further increase in the laser energy will not increase compressive residual stresses appreciably. Also, tensile cracking might be an issue with higher energies. Based on these results, the current sequence and laser parameters (energy 3 J, pulse width 27 ns, spot diameter 2 mm) were utilized for LSP processing of the fatigue test coupons.

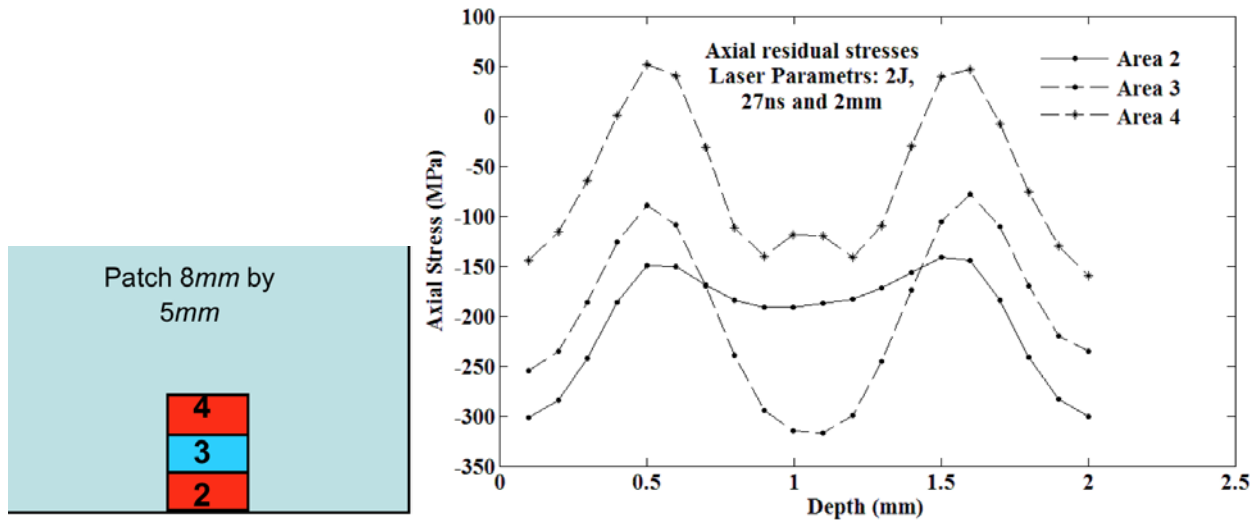


Figure 44: Residual Stress Profiles Obtained from LSP Simulation of 8 mm x 5 mm Patch With Modified Sequence and Laser Parameters of 2 J, 27 ns, 2 mm Spot Size

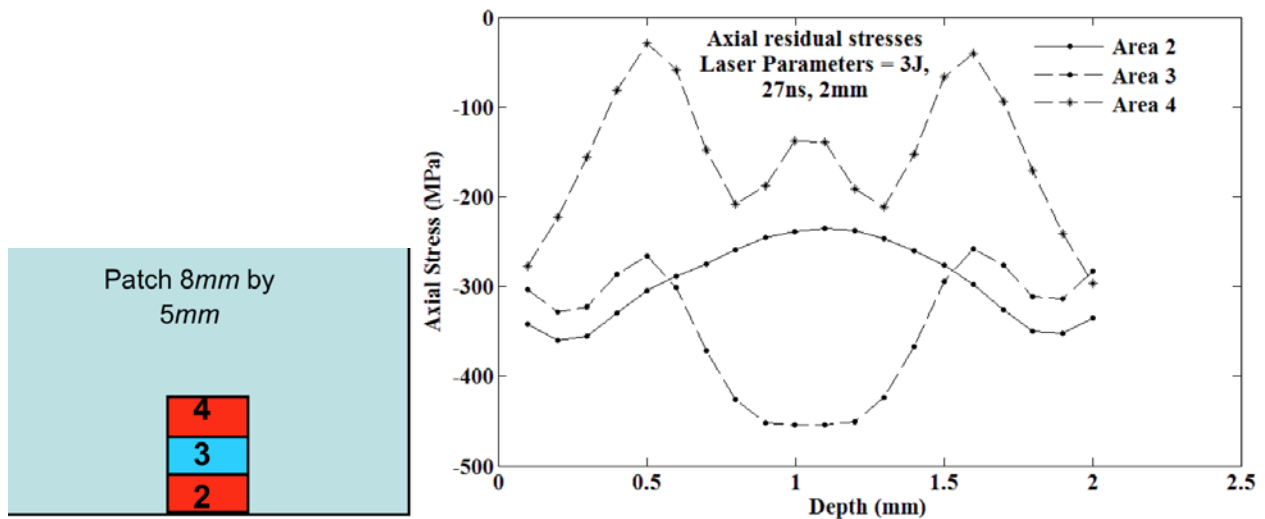


Figure 45: Residual Stress Profiles Obtained From LSP Simulation of 8 mm x 5mm Patch With Modified Sequence and Laser Parameters 3 J, 27 ns, 2 mm Spot Size

3.2.5 Static Tests and Properties

A specimen measuring 75 mm long x 10 mm wide x 4.2 mm thick and gage length of 25 mm was machined using EDM for tensile tests to determine the yield strength of the as-received Ti6242 material. Prior to the tests, a strain gage was affixed axially to the surface of the specimen. A typical load vs. strain plot is shown in Figure 46. From this data, the 0.2% yield strength was determined to be 952 MPa, which is close to the values reported for Ti6242 alloy in the literature. Static and fatigue tests on 3PB unpeened and laser peened coupons having dimensions of 60 mm length x 10 mm width x 2 mm thickness (Figures 33, 34) were also conducted to determine the yield load/stress, as

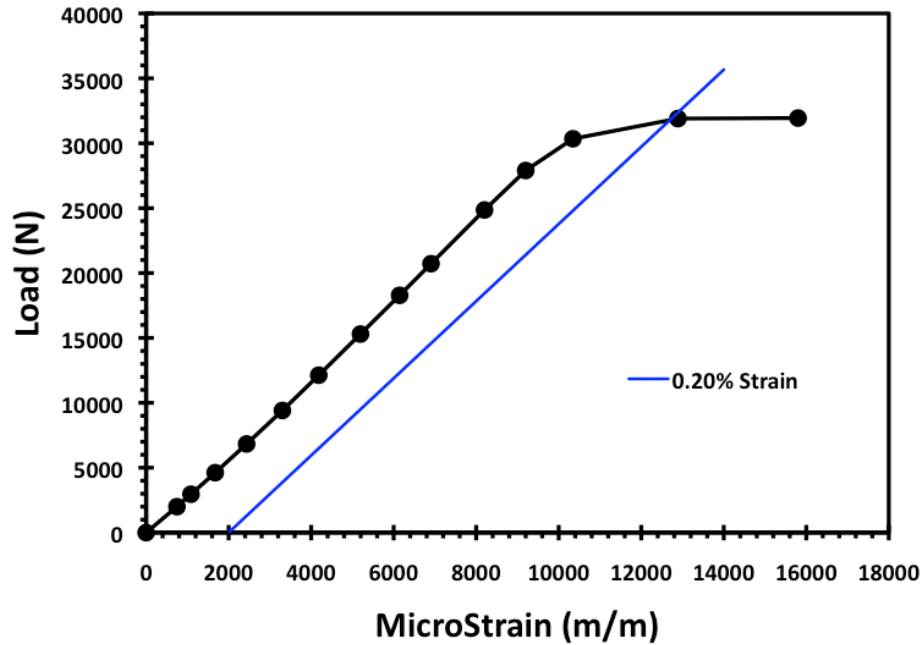


Figure 46: Load Versus Strain Data Recorded During a Tensile Test on As-Received Ti6242 Alloy Coupon

Well as to help decide the range of load/stress levels to use for the fatigue tests. Results of the FE simulations on these same coupons were presented in the previous section. A photograph of a typical coupon with the 8 mm x 5 mm LSP-treated patch, together with a higher magnification photograph showing the notch area are displayed in Figures 47(a) and 47(b), respectively.

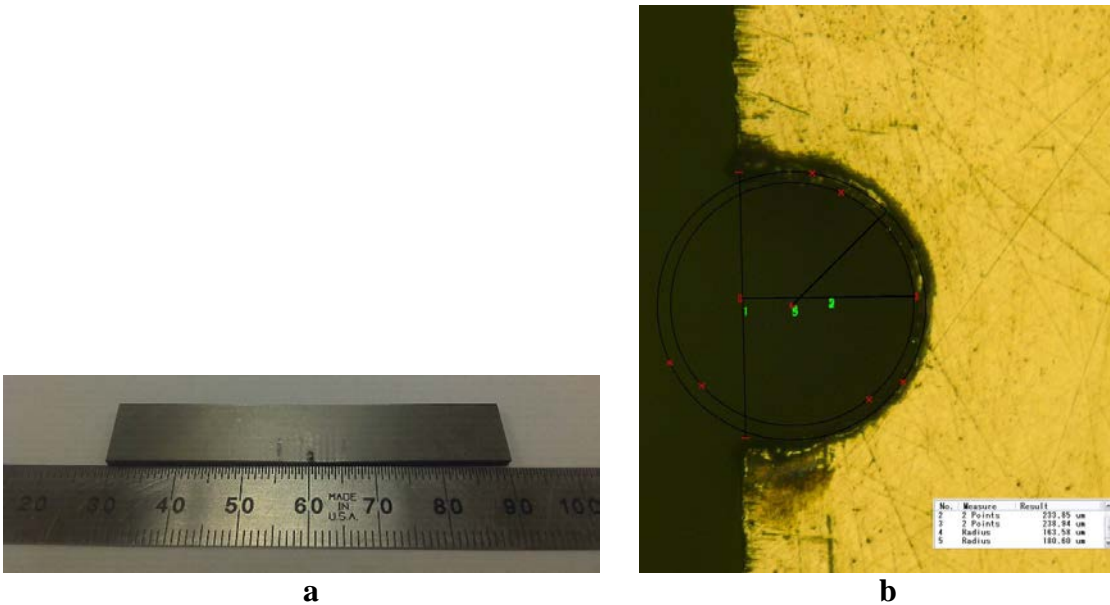


Figure 47: Photographs of the 3PB Static and Fatigue Test 60mm Long x 10mm Wide x 2mm Thick Showing the LSP-Treated Area and Details of the Notch

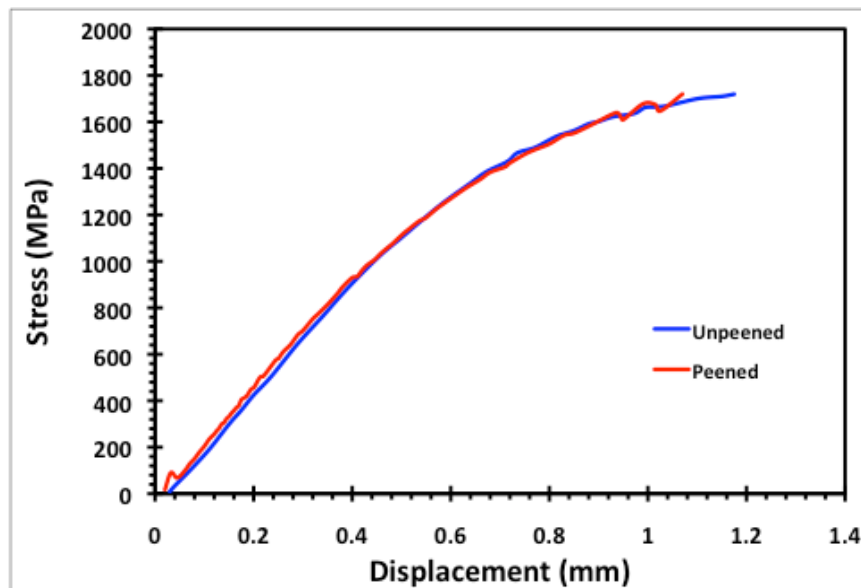


Figure 48: Load Versus Displacement Data Recorded During a Static 3PB Test on Unpeened and LSP-Treated Notched 60mm x 10mm x 2mm Thick Ti6242 Coupon

The notch was made by EDM using a 0.01 inch (25 mm) diameter wire after LSP-treatment and has a radius of $\sim 170 \mu\text{m}$ and depth of $\sim 250 \mu\text{m}$ (0.25 mm). The stress concentration factor for this notch calculated using FE analysis was in the range of 3.9 to 4.1. Stress versus displacement data for the unpeened and LSP-treated coupons is shown in Figure 48. It is evident that the curves from both overlap and the 0.2% yield stress is near 950-1000 MPa. It should be noted that the stress levels and strain at the notch would be far higher, so that one would expect yielding to occur near the notch at much lower nominally applied loads/stresses.

3.2.6 Fatigue Tests and Behavior

As mentioned in the previous sub-section, 3PB fatigue test specimens were prepared by EDM having the geometry and dimensions shown in Figures 33 and 34. These specimens were notched in the center of the bottom/tensile edge (middle of LSP patch) to a depth of 0.25 mm using a 0.01 inch (25.4 μm) diameter wire, as shown in Figure 47. The purpose of the notch was to assure that the crack will start at the same location (notch tip) in all specimens. The stress concentration factor for this notch was calculated, using finite element analysis to be in the range of 3.9 to 4.1. Three kinds of specimens were tested.

1. Unpeened (as machined) and Notched;

2. **Laser Shock Peened (LSP'd) and Notched.** As described in sections 3.2.3 and 3.2.4, FE simulations of the LSP process were conducted to determine the laser parameters that would generate through thickness compressive residual stresses. Based on these simulations we selected the conditions of 3 J laser energy, 27 ns pulse width, and two hits at the same location for all LSP processing (see simulation results in Figure 45 and typical specimen with 8 mm x 5mm LSP patch in Figure 47). The surface residual stress in these specimens was determined by CXRD to be around -425 MPa.

3. **Laser Shock Peened and Notched and aged @482°C (899.6°F).** The LSP treated (3 J, 27 ns, 2 hits) coupons were heat treated at 482°C for 24 hours in a vacuum furnace. This choice is based on the study of the thermal stability of the LSP induced residual stresses at several temperatures described in section 4.1.1.2 (Figure 18); the 482°C, 24h heat treatment was selected in order to evaluate the thermal stability of the fatigue life at an extreme condition, even though the normal operating temperature for this material is far below the 482°C. The surface residual stress in these specimens was reduced compared with the as-peened specimens to a value of about -250 MPa.

The specimens were tested using an MTS Bionix hydraulic test system in a three-point bending configuration. The tests were done at 15 Hz with an R value of 0.1 under load control, with the range of applied loads chosen to be in the elastic regime as per the static load-displacement data (Figure 46). The maximum bending stress was calculated from the maximum load (Newtons) during the test assuming the standard elastic stress formula for this specimen geometry, namely, $\sigma = 3PL/4bb^2$, where P = applied load, L = span length between outer two bottom rollers, b = thickness (2 mm) and h = height/width (10 mm). The fatigue results are tabulated in Table 5 below and the data of the applied maximum bending stress on the coupon versus number of cycles to failure, N_f , is shown plotted in Figure 47 for the three types of specimens. The stress concentration factor for the notch is between 3.9 and 4.1, which means that although the nominal bending stress on the entire specimen is in the elastic regime, those at the notch would be much higher and thus sufficient to cause local plastic deformation, depending on the magnitude of the applied load.

The unpeened specimens were tested at several stress conditions. The data is well behaved with a good polynomial fitted curve with an R^2 value of 0.992; thus we can calculate the fatigue lives for any stress value in the fitted range. The LSP'd specimens were tested at 175, 200, 225, and 250 MPa. These values were selected to evaluate the High Cycle Fatigue (HCF) behavior. The tests were terminated at 5 million cycles and are indicated with a horizontal arrow. The life is higher than 5 million cycles at 175 MPa (max stress). The calculated crack tip stress amplitude corresponding to

this applied stress was calculated to be 384 MPa, based on a stress concentration factor of 4. At higher stress values the LSP-treated specimens had an increased life between 2.3 to 9.6 times that of the unpeened specimens.

Table 5. Results of 3PB Fatigue Tests on Unpeened, LSP-Treated and LSP-Treated + Aged Ti6242 Alloy Coupons

Unpeened, Notched		LSP'd (3J, 27 ns, 2 Hits), Notched		LSP'd (3J, 27 ns, 2Hits), Notched and Aged @482°C/24hrs		LSP'd Life/ Unpeened Life	LSP'd and Aged Life/ LSP'd Life	LSP'd and Aged Life/ Unpeened Life
Stress (Mpa)	Cycles to Failure	Stress (Mpa)	Cycles to Failure	Stress (MPa)	Cycles to Failure			
150	1,270,000							
175	729,000	175	5,000,000	175	5,000,000	6.86		
200	410,000	200	939,304	200	437,457	2.29	0.47	1.07
200	410,000	200		200	903,995			
225	226,000	225	646,500	225	303,745	2.86	0.47	1.34
225	226,000	225	2,160,000	225	305,799	9.56	0.14	1.35
250	190,000	250	1,006,000			5.29		
270	123,000							
302	97,000							
337	65,000							
380	43,670							

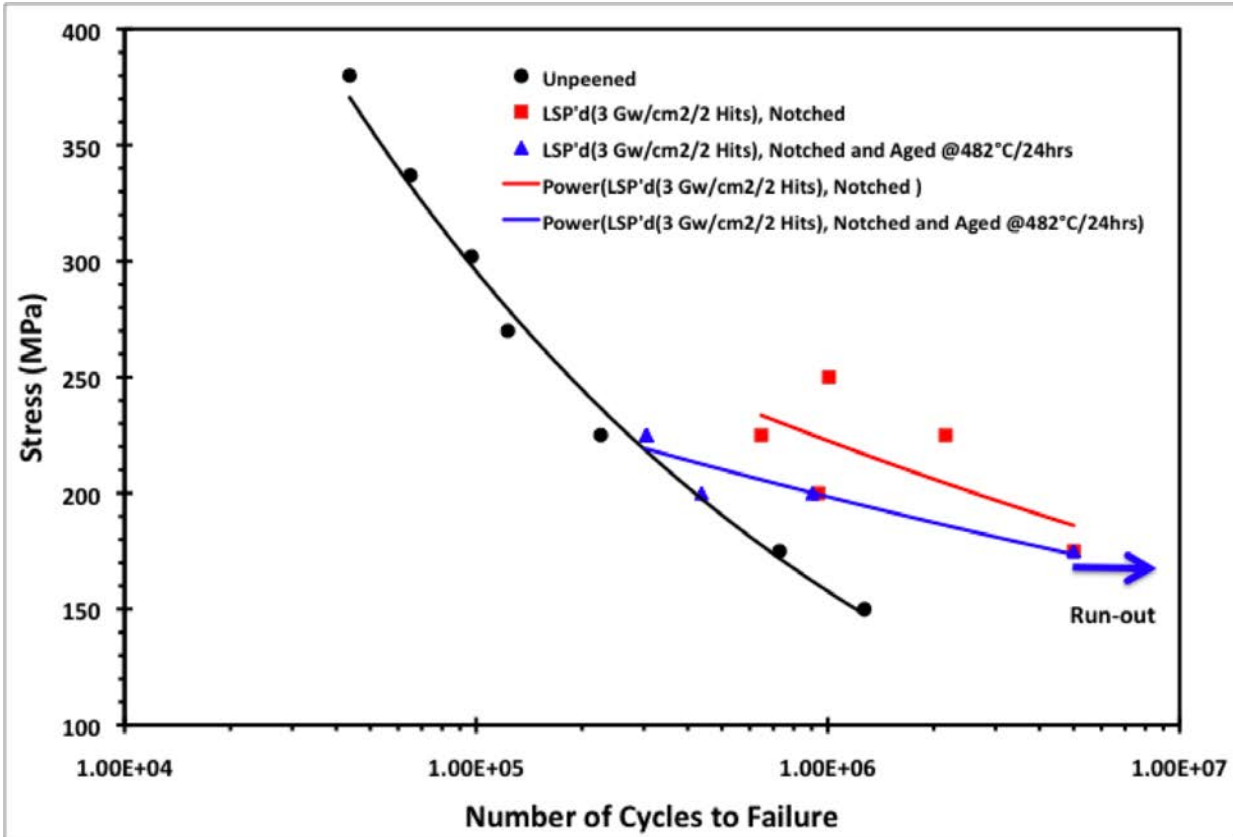


Figure 49: Plot of Applied Maximum Bending Stress Versus Number of Cycles to Failure From 3PB Fatigue Test on Unpeened, LSP-Treated and LSP-Treated + 482°C, 24b-Aged Ti6242 Alloy Coupons

The aged specimens were tested at 175, 200, and 225 MPa. Run-out (≥ 5 million cycles) was observed at the 175 MPa level. At 200 MPa the fatigue life was reduced to 46% of the as LSP'd specimen, but is still higher than the unpeened specimen by at least 7%. At 225 MPa the fatigue life was reduced from $\sim 14\%$ to 46% of as the LSP'd specimen, but is still higher than that of the unpeened specimen by at least 34%. These numbers are based on test results obtained from one or two specimens and will vary as more specimens are tested. The data indicate that even after even after aging at relatively high temperatures, the LSP-treated specimens seem to retain the fatigue life enhancement over unpeened specimens, thus demonstrating the thermal stability of the fatigue life.

3.2.7 Fractography of Failed Fatigue Specimens and Fatigue Crack Growth

The fracture surfaces of the three kinds of the fatigue-tested specimens were observed by SEM to shed light on fatigue crack initiation and subsequent growth. Observations suggested that initially multiple small cracks were initiated from the notch, which then joined into a single larger crack. Striations characteristic of Stage II fatigue crack growth could be seen only at a distance of ~ 2 mm from the notch and beyond. Representative high magnification SEM micrographs recorded from the fracture surface at a distance of ~ 2 mm and ~ 4 mm from the notch tip of a fatigued tested unpeened specimen are shown in Figures 48(a) and 48(b), respectively. Counterpart micrographs at approximately the same distances from the LSP-treated and LSP-treated + 482°C, 24 h-aged specimens are shown in Figures 49(a,b) and 50(a,b), respectively.

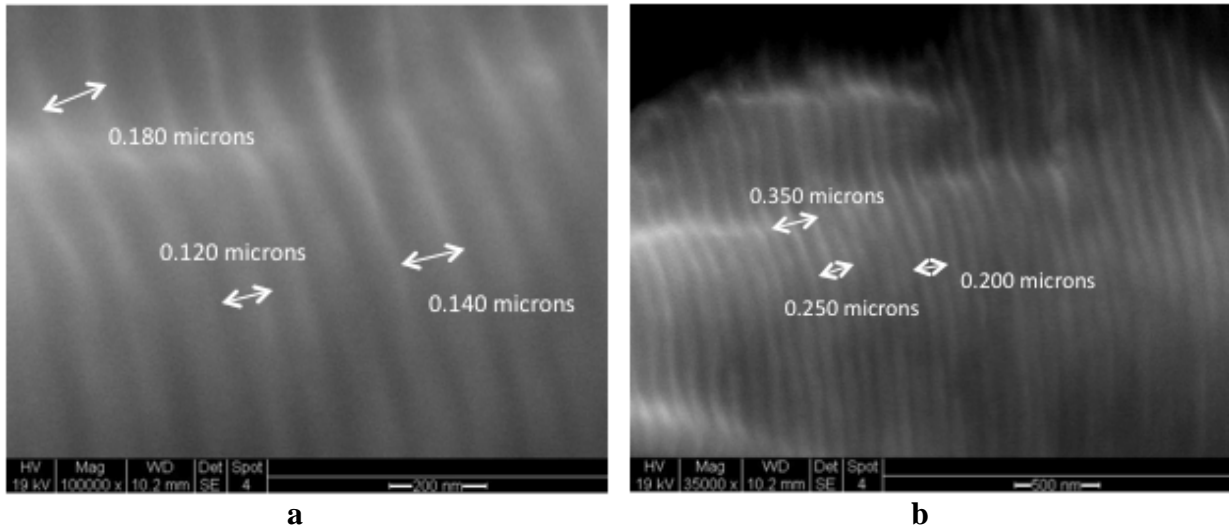


Figure 50: SEM Micrographs Recorded From the Fracture Surface of a Fatigue Tested Unpeened Ti6242 Specimens at a Distance of (a) ~2mm and (b) ~4mm From the Notch Tip Showing Striations Characteristic of Stage II Fatigue Crack Growth

In all cases, striations characteristic of Stage II fatigue crack growth can be seen. The spacing between adjacent striations, da , which represents the growth of the crack in one cycle, dN , were measured from the respective images and were found to increase as the crack grew. The spacings and hence the growth rates varied between the unpeened, LSP-treated and LSP-treated + aged specimens. Based on the applied stress range ($\Delta\sigma$), the crack length (a) and the 3PB specimen geometry (width w), the stress intensity range, ΔK , was calculated using the following equation:

$$\Delta K = f\left(\frac{a}{w}\right)\Delta\sigma$$

$$f\left(\frac{a}{w}\right) = 3 \cdot \left(\frac{a}{w}\right)^{0.5} \cdot \frac{\left[1.99 - \left(\frac{a}{w}\right) \cdot \left(1 - \frac{a}{w}\right) \cdot \left(2.15 - 3.93\frac{a}{w} + 2.7\left(\frac{a}{w}\right)^2\right)\right]}{2 \cdot \left[\left(1 + 2\frac{a}{w}\right) \cdot \left(1 - \frac{a}{w}\right)\right]^{1.5}}$$
(13)

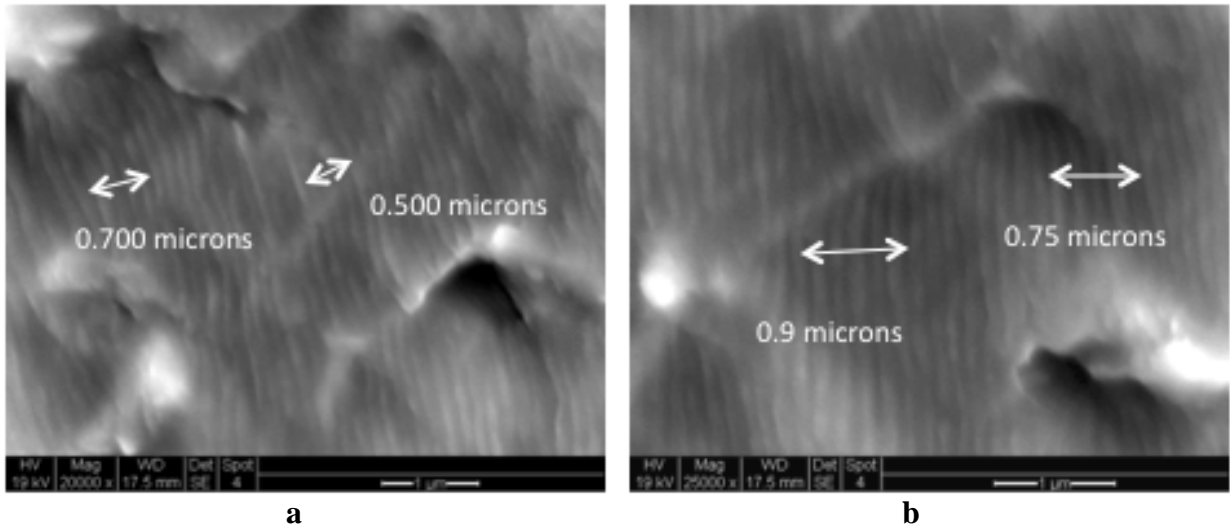


Figure 51: SEM Micrographs Recorded From the Fracture Surface of a Fatigue Tested LSP-Treated Ti6242 Specimens at a Distance of (a) ~2mm and (b) ~4mm From the Notch Tip Showing Striations Characteristic of Stage II Fatigue Crack Growth

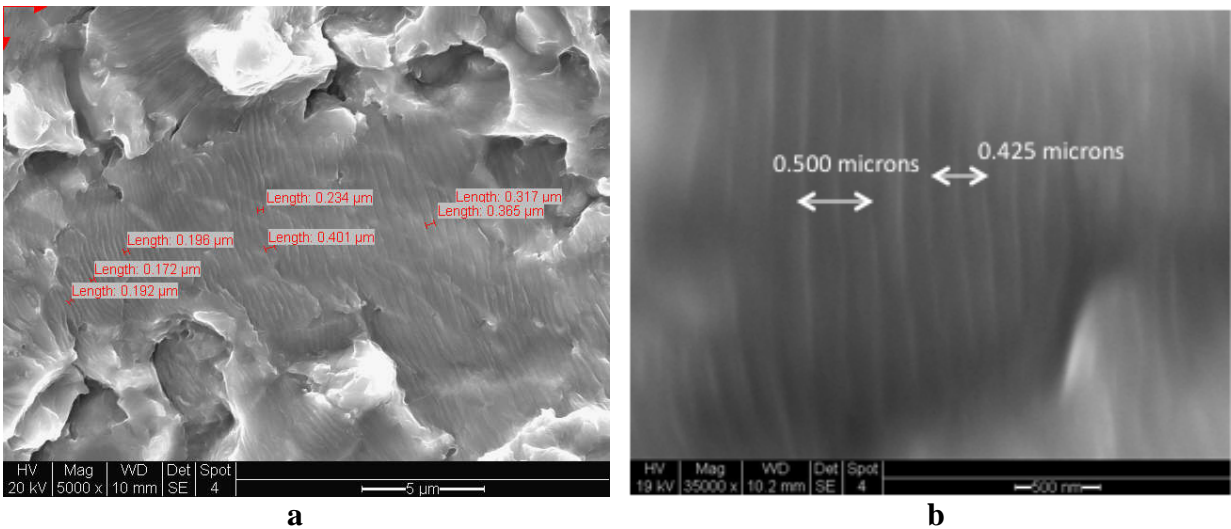


Figure 52: SEM Micrographs Recorded From the Fracture Surface of a Fatigue Tested LSP-Treated +482C, 24 h-Aged Ti6242 Specimens at a Distance of (a) ~2mm and (b) ~4mm From the Notch Tip Showing Striations Characteristic of Stage II Fatigue Crack Growth

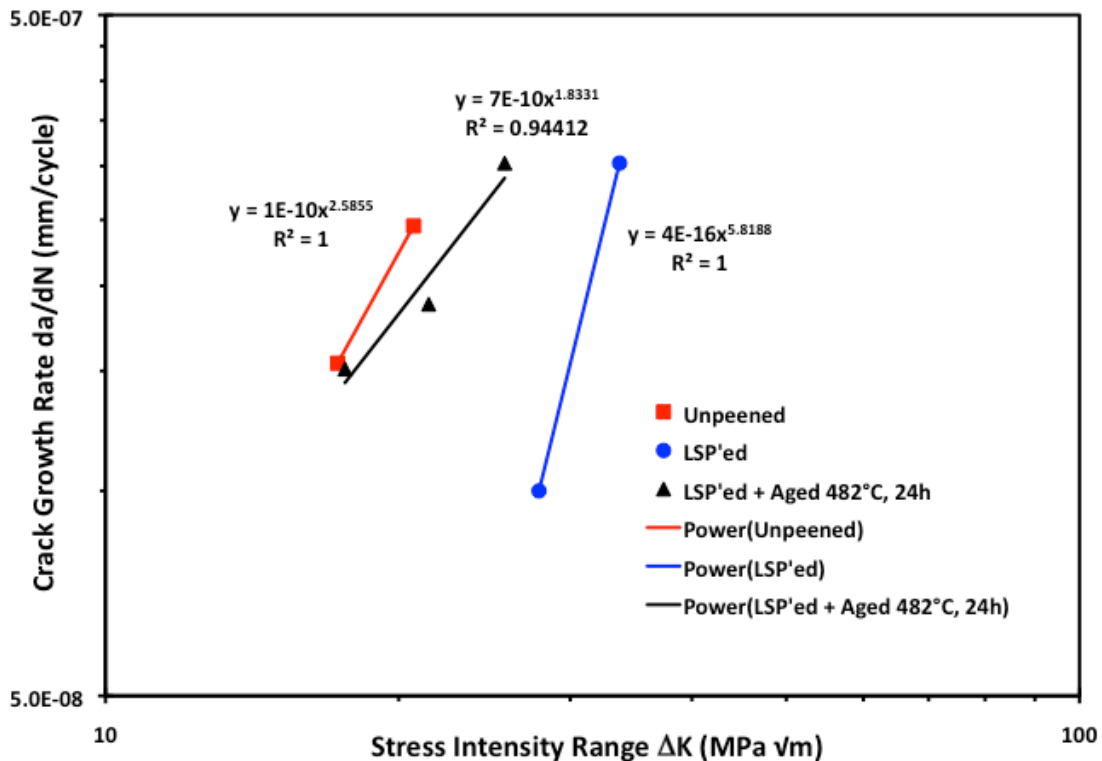


Figure 53: Plot of Crack Growth Rate, da/dN Versus Applied Stress Intensity Range, ΔK , Based on Measurement of Striation Spacings on Fracture Surfaces and Calculations for Unpeened, LSP-Treated and LSP-Treated +482°C, 24 h-Aged Ti6242 Alloy Coupons

The plot of the crack growth rate, da/dN , versus the applied stress intensity range, ΔK , thus obtained from the analysis of the SEM images and calculations is shown in Figure 53. Although the data are somewhat limited, it can be seen that the stress intensity range required to achieve a given crack growth rate is much higher in the LSP-treated samples than in the unpeened specimens, or, in other words, at a given stress intensity range, the crack growth rates are much lower in the LSP-treated specimens. These results again point to the beneficial effects of LSP in enhancing fatigue crack growth resistance. The values in the LSP-treated + aged specimens lie in between, but are higher than those in the unpeened case. This suggests that the enhancement of fatigue life following LSP is still retained at elevated temperatures, even above the expected service temperatures for the Ti6242 alloy. The data in Figure 53 suggest that the improvement in fatigue life and crack growth rates principally arises because of the presence of the compressive residual state in the near-surface regions brought about by LSP reduces the magnitude of the stress intensity at the crack tip at the same applied stress range compared with the unpeened material. It should be noted, that though the FCG data are limited, the exponent m in the relation $da/dN = C\Delta K^m$ for Stage II crack growth determined from the striation spacing data, is higher in the LSP-treated specimens compared with the unpeened specimens, but lowest in the LSP-treated + aged specimens. Additional, proper FCG tests are required to obtain data over a wider ΔK range to fully confirm these findings.

3.3 Results of LSP Effects on Residual Stress, Microstructure, Thermal Relaxation and Fatigue Behavior of IN718 Plus Alloy

Since the IN718 Plus alloy is strengthened by precipitation of γ' , it was felt that it was important to understand the effects of thermal aging on the precipitation behavior before studying the effects of LSP and post-thermal treatment effects on residual stress and microstructure evolution and the fatigue behavior. In the sub-sections that follow, the effects of thermal aging on microstructure evolution and hardening of non-LSP-treated alloy samples are first described, followed by those on the effects of LSP on residual stress evolution, thermal relaxation and fatigue behavior.

3.3.1 Thermal Aging Effects on Precipitation Behavior

The IN718 Plus material was obtained from ATI Allvac in the form of 250 mm x 250 mm square sheets of various thicknesses, namely 1.875 mm, 5 mm and 12.5 mm. These plates had been hot-rolled and then heat-treated at 953°C for 0.5h followed by air-cooling. Coupons were cut from the sheet, covered with sacrificial Ta-foil and vacuum sealed in Quartz tube with Ar back-fill. These samples were then aged at 650°C (923K), 700°C (973K), 750°C (1023K), 800°C (1073K) and 850°C (1123K) for times ranging from 5 to 1000 h. Hardening was characterized by micro/Knoop hardness measurements and microstructures were characterized by OM, SEM and TEM, with EDS.

3.3.1.1 Microstructure of As-received Material. Since the IN718 Plus plates were subjected to sub-solvus hot rolling, the microstructure based on reported TTT diagram [75] given in Figure 54 is expected to contain varying amounts of δ -Ni₃Nb phase particles at grain boundaries. Our OM observations of the as-received material (Figure 55(a)) revealed equiaxed grains. EBSD/OIM observations in Figure 55(b,c) confirm the material is isotropic and devoid of any rolling texture and has a grain size of ~25 microns. Both Vickers and Knoop hardness tests were conducted on as-received and thermally aged materials and were found to be in good agreement with each other. The plots for different aging conditions are shown in Figure 56. The as-received materials show low hardness due to the solutionizing treatment. Peak hardness occurs at 923K/500h and hardness reduction is seen at 1123K and 1023K/500h. Isothermal aging between 923K – 1023K leads to a sharp hardness increase initially for at least up to 50 h followed by progressive reduction once the peak is reached. Peak hardness magnitude and occurrence time of the peak are inversely related to aging temperature. The rate of hardness decrease after the peak is smaller than the rate of increase before the occurrence of peak. Based on hardness results, it can be estimated that the nucleation of γ' precipitates, the prime strengthening phase in IN718 Plus, takes place very quickly followed by rapid growth until achieving peak hardness. The subsequent hardness reduction could be attributed to conversion to stable phases like η at the expense of γ' .

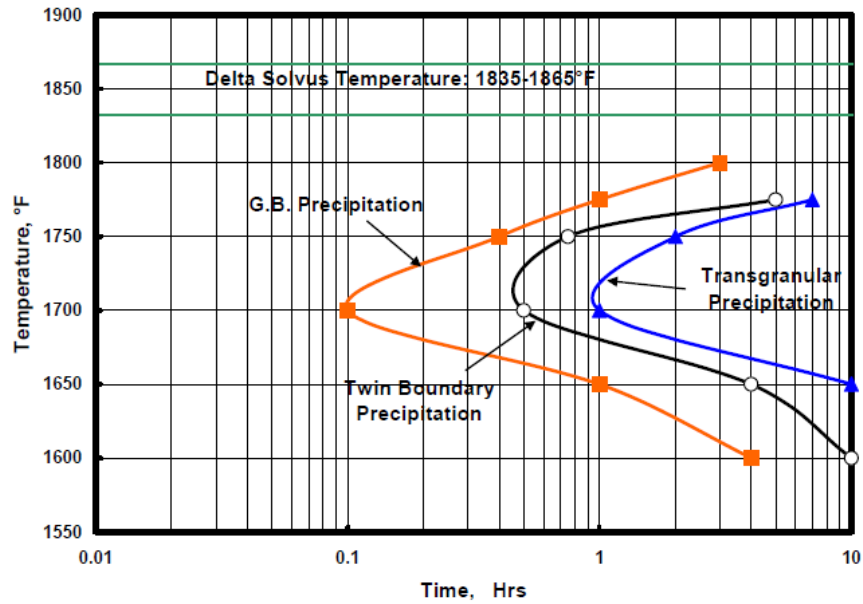


Figure 54: TTT Curve of δ Phase Precipitation in IN718 Plus [75]

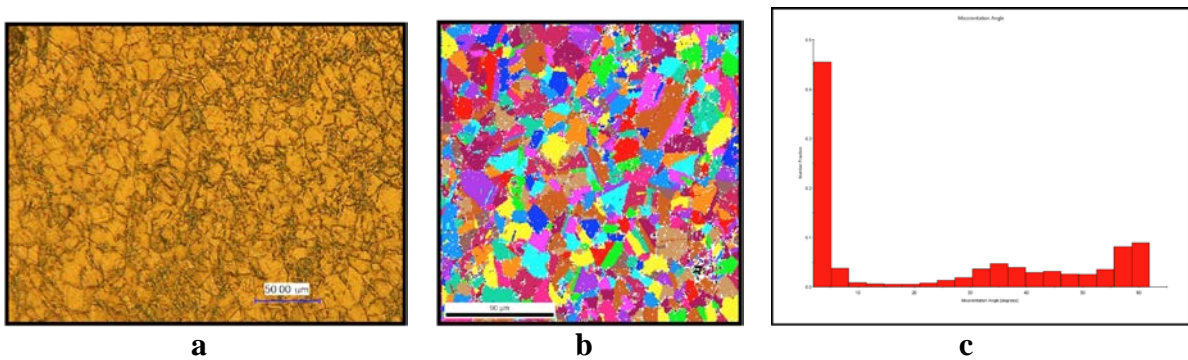


Figure 55: Microstructure of As-Received IN718 Plus Alloy: (a) OM, (b) EBSD/OIM Map and, (c) Grain Mis-orientation Map

Hardness behavior: Instrument: Leco – ½ kg, 25 second load time, room temperature.

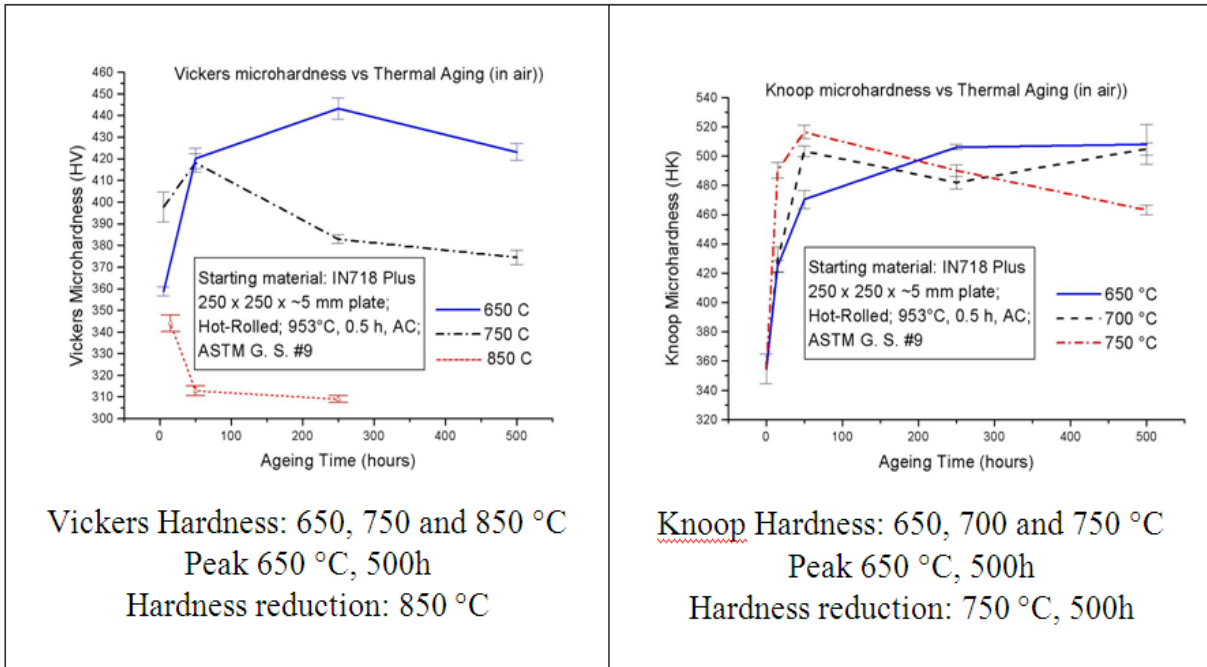


Figure 56: Vickers and Knoop Hardness Evolution of IN718+ With Aging Time at Different Temperatures

3.3.1.2 TEM Observations of Microstructure of As-Received and Aged Samples. Figure 57(a) shows a TEM micrograph from the as-received material, showing plate-shaped η -Ni₃Ti precipitates, which is confirmed by the SAD pattern in Figure 57(b) recorded from a region containing the plate and the γ matrix. The orientation relationship between the two phases determined from the SAD pattern is given by:

$$(-1-11) \gamma // (0001) \eta\text{-Ni}_3\text{Ti} \text{ and } [011] \gamma // [2-1-10] \eta\text{-Ni}_3\text{Ti} \quad (14)$$

No γ' precipitates were present in the γ matrix, which was also confirmed by the absence of expected superlattice reflections at the $\{100\}$ and $\{110\}$ positions from the former in the SAD patterns. A few δ -Ni₃Nb particles were also observed (Figure 57(c)).

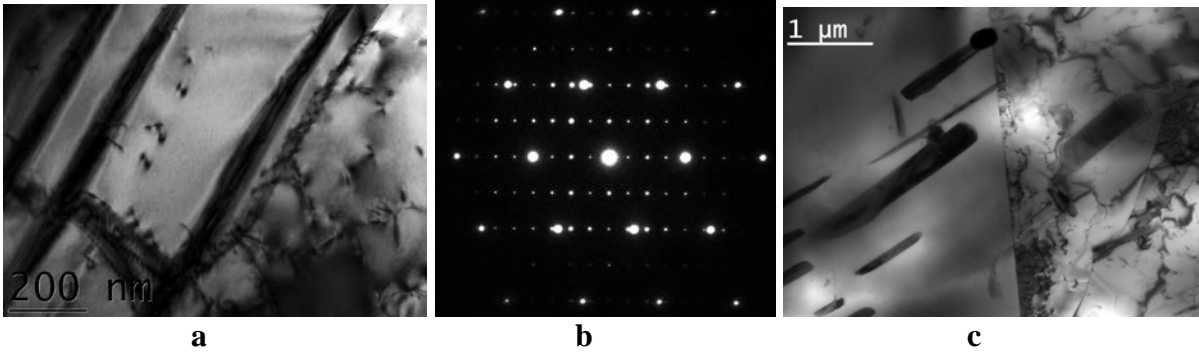


Figure 57: TEM Micrographs Showing the Microstructure of As-Received IN718+ Alloy. a) BF Micrograph Showing η -Ni₃Ti Precipitates b) SAD Pattern Recorded From Region Containing γ Matrix and η and c) BF Micrograph Showing δ -Ni₃Nb Precipitates

TEM micrographs recorded from the samples aged at different temperatures (650-850°C) for various times are shown in Figures 58-61. It can be seen from Figures 58 and 59 that the γ' size is very fine at short times, especially at the lower aging temperatures (650°C) and progressively increases with aging time and temperature. Also, longer times and particularly at higher temperatures, formation of plate shaped precipitates is observed which increase in thickness and number density at the expense of γ' . These precipitates were identified as η -Ni₃(Nb,Al,Ti) and δ -Ni₃(Nb,Ti) by SAD, EDAX analysis and comparison of their observed orientation relationship with the γ matrix with computer simulations of the SAD patterns (Figure 62). The δ -Ni₃Nb has been reported in earlier studies [75], and is found often at grain boundaries and is seen to have the following orientation relationship:

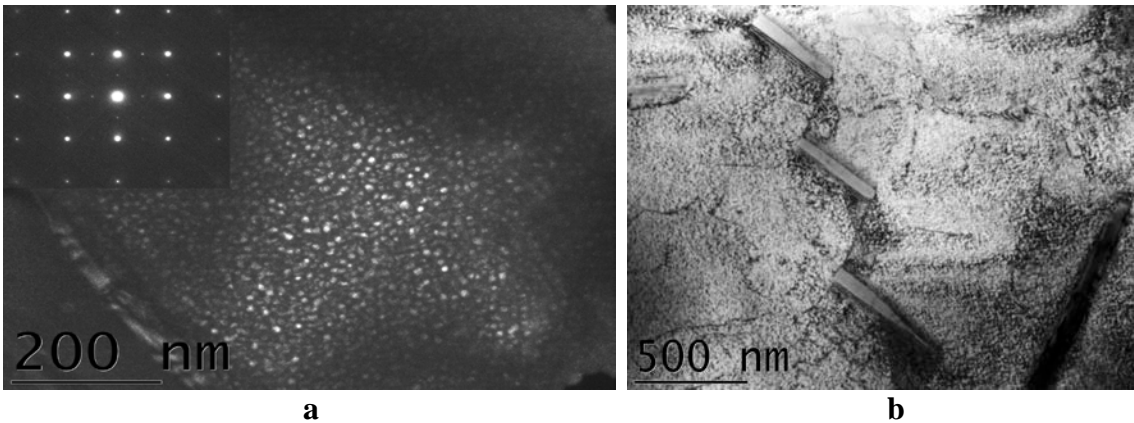


Figure 58: Microstructure of IN718+ Alloy Aged at 650°C, 250 b (a) DF TEM Micrograph Showing Ultrafine (5-10 nm) γ Precipitates (Inset [001] SAD Pattern) and b) BF Micrograph Showing η -Ni₃Ti Precipitates

$$(1-10) \gamma // (100) \delta\text{-Ni}_3\text{Nb}, [1-1-1] \gamma // [010] \delta\text{-Ni}_3\text{Nb} \quad (15)$$

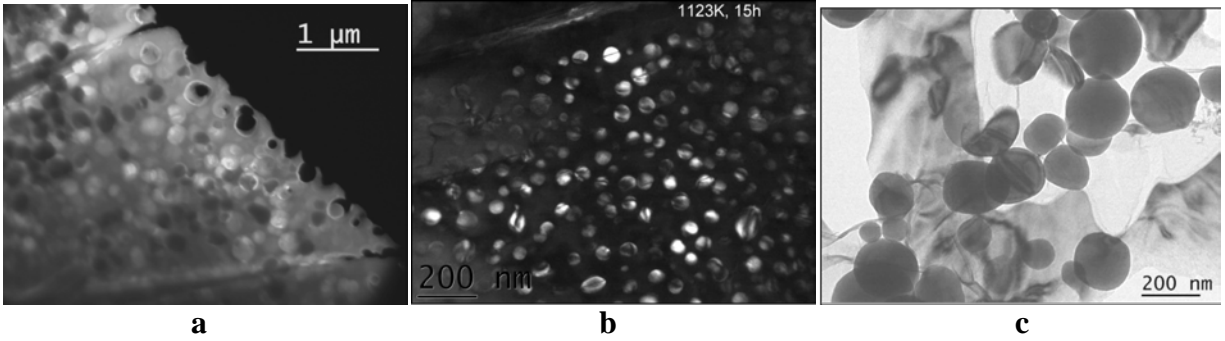


Figure 59: DF TEM Micrographs Recorded From IN718+ Alloy Aged at (a) 800C, 1000b, (b) 850°C, 15b and (c) 850°C, 200b Showing γ Precipitates

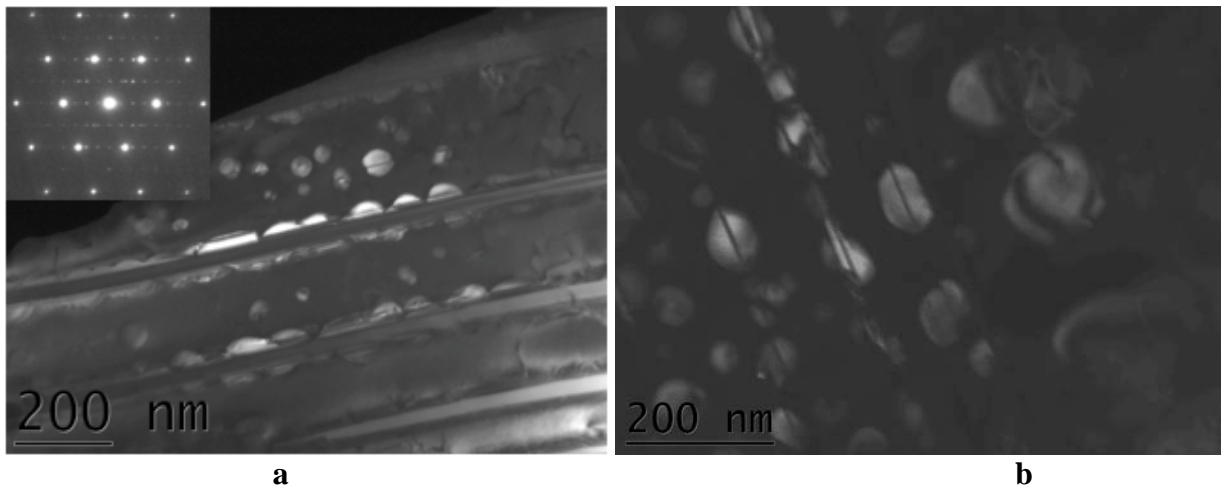


Figure 60: DF TEM Micrographs Recorded From IN718+ Alloy Aged at 750°C for (a) 250b (inset $[011] \gamma // [011] \gamma' // [11-20] \eta\text{-Ni}_3\text{Ti}$ SAD Pattern) and (b) 500 b Showing γ' Precipitates Containing Faults, as Well as $\eta\text{-Ni}_3\text{Ti}$ Plates Cutting Through the γ' (in "a")

$[0001]$ CBED patterns confirmed the hexagonal symmetry associated with the DO_{24} $\eta\text{-Ni}_3\text{Ti}$. This is the first confirmatory study for the occurrence of Ni_3Ti in this alloy.

3.3.1.3 γ' to $\eta\text{-Ni}_3\text{Ti}$ Transformation Through a Faulting Mechanism. The larger size γ' precipitates showed the presence of faults parallel to the $\{111\}$ planes (Figures 60,61), which appeared to be precursors for the formation of $\eta\text{-Ni}_3\text{Ti}$ from γ' . Kear et al. [76] had proposed that plate shaped particles of Ni_3Ti form through a faulting mechanism operative in the L_1_2 structure of γ' . The faults were proposed to be intrinsic and lie on the $[111] \gamma // [0001] \text{Ni}_3\text{Ti}$ planes and transform to stable precipitates through a superlattice faulting mechanism involving shear with Frank sessile along $\{111\}1/3\langle 112 \rangle$ or climb along $\{111\}1/3\langle 111 \rangle$ to give rise to abc/abc DO_{24} Ni_3Ti . The mechanism for creation of a stacking fault was thought to be segregation of solute atoms at the Frank sessile. Since the matrix is enhanced in Ti as Al migration takes place to γ' during coarsening based on the phase diagram, there exists a viable mechanism for η -transformation which is thermodynamically more stable compared to γ' at longer durations and higher temperatures. Since

the driving force for this transformation is lattice mismatch, we attempt to model the driving force for this transformation based on the same. For an $L1_2$ structure with lattice constant, a_{L1_2} , mismatch with the $D0_{24}$ lattice of constant, $a_{D0_{24}}$, is given by:

$$d = \left(\frac{a_{D0_{24}}}{2} - \frac{a_{L1_2}}{\sqrt{2}} \right) / \text{atom in slip direction } \langle 110 \rangle \quad (16)$$

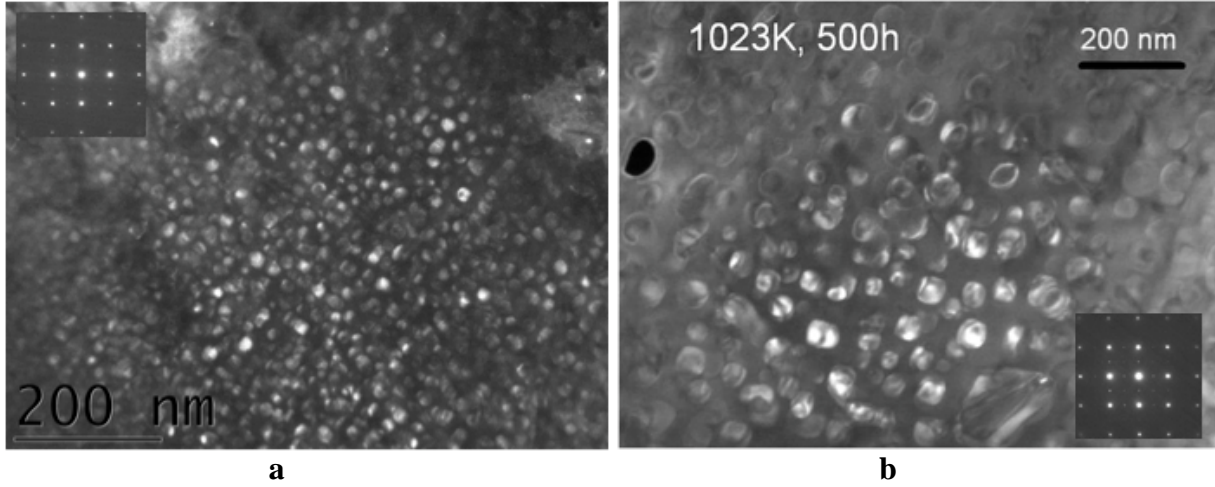


Figure 61: DF TEM Micrographs Recorded From IN718+ Alloy Aged at 700°C for (a) 250b and (b) 500b Showing γ' Precipitates Insets [001] SAD Pattern

The maximum size to which the precipitate can grow before a dislocation is geometrically necessary is:

$$D_{\max} = \left(\frac{a_{D0_{24}} a_{L1_2}}{a_{D0_{24}} - \sqrt{2} a_{L1_2}} \right) \quad (17)$$

Upon substituting for Ni_3Ti ($a = 5.12$ Å) and γ' ($a = 3.6$ Å) we get a value of 44 nm for the γ' size beyond which faulting is expected. This result matches with our TEM observations of faulting incidence in γ' particles as they grow in size as shown in Figure 59-61. Faulting was observed in γ' particles larger than 60 nm, whereas there is no faulting observed at smaller γ' sizes, which is a good confirmation of the mechanism.

3.3.1.4 γ' Coarsening Kinetics and Activation Energy Analysis. Precipitate coarsening is driven by reduction in surface energy as originally proposed by Ostwald and then formulated by Lifshitz, Sloyozov and Wagner (LSW). The driving force for coarsening was found using particle size measurements from TEM data and activation energy analysis. The LSW theory proposes that for dilute solutions the coarsening kinetics follows a law of the type:

$$D^3 - D_o^3 = Kt \quad (18)$$

Where: D_0 = initial particle diameter, D = particle diameter at aging time t , K = temperature dependent rate constant and t = aging time.

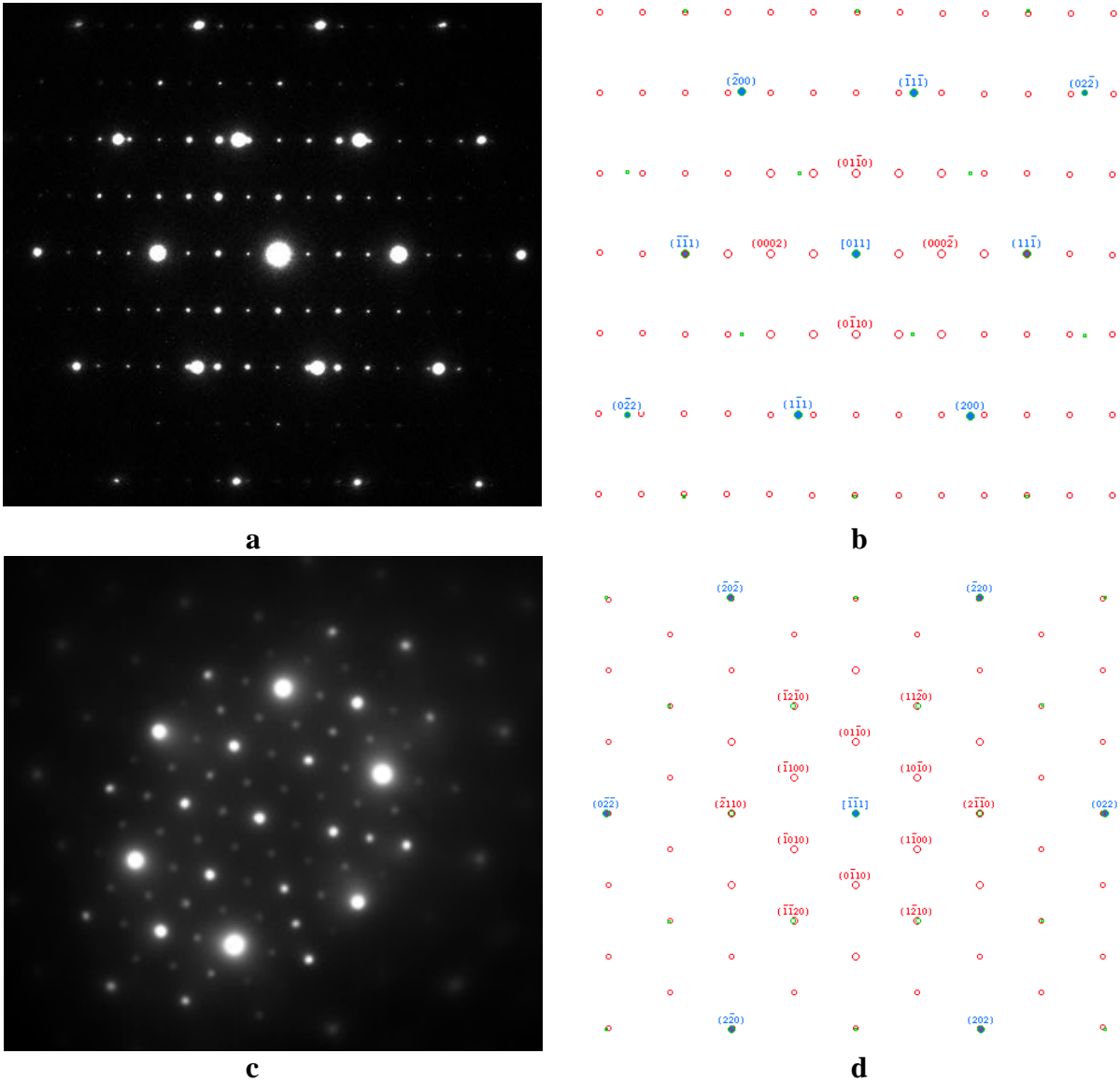


Figure 62: (a,c) Experimental and (b,d) Computer Simulated SAD Patterns Confirming the Plate-Shaped η -Ni₃Ti Precipitates. (a,b) $[011] \gamma // [11-20] \eta$ and (c,d) $[111] \gamma // [0001] \eta$

4.4. General Discussion

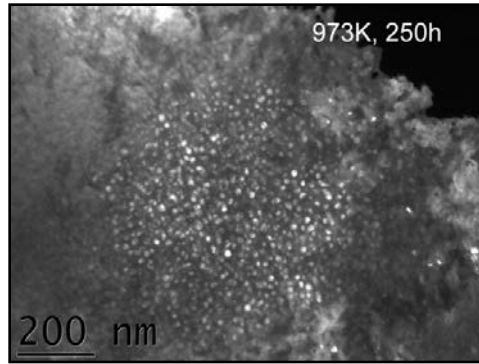
Based on observed particle data, we determined the activation energy for coarsening. Since particle size measurement is fundamental to ascertaining the rate law, two concurrent methods of particle size measurement were attempted in arriving at a reliable measure as follows:

(1) **Manual measurements with tracing:** While the basic aim was to remove human intervention and attempt measurement using image analysis, local variation in contrast conditions

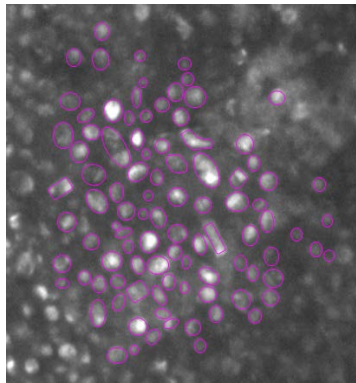
due to foil thickness, illumination or foil bending rendered it ineffective and introduced scatter, thus manual measurements were required. Tracing of particle contours was done carefully using MS-Office suite and the images created were analyzed with the WPIC ImageJ software version of the image processing program IMAGEJ, developed by National Institute of Health (NIH) and freely available for academics and research. Particle sizes are based on direct measurements of γ' -precipitates from dark field TEM images taken on the Philips CM20 TEM with Gatan CCD based image acquisition. Regions of good contrast in the images with at least 10 to 100 distinct γ' -precipitates for each aging time and temperature condition were identified for image analysis. Tracing of the individual precipitates was done manually using MS-Office 2007 software, and the dimensions of traced particles were determined utilizing the WPIC ImageJ software. Since the particles were generally spherical for all aging conditions investigated, with a few cuboidal shapes arising at longer aging times, the particle diameter, D , required for coarsening kinetics was estimated from the measured area based on circular equivalence, i. e. $D^2 = \text{area}/\pi$. Typical results are shown in Figure 63.

(2) **Image analysis by segmentation:** A computer algorithm based on maximizing entropy has been found to have good success in TEM image analysis [78] for nanoparticles, in comparison with other methods. This plug-in is built into the WPIC-ImageJ software. Hence, for smaller particles that occur at lower temperatures and are very small and not well-defined, and where manual methods were subject to personal bias, image analysis using this technique was employed. The key to such measurements is to reduce the area to be analyzed to a very small part of the image where local variations in background contrast are minimal. The image histogram is then normalized and a background-subtracted binary image generated. This image is used for thresholding, i.e., determining a cut-off range in the intensity profile between which particle contrast variations are identified as a boundary using the WPIC ImageJ software. In all images, pixels were calibrated to the length scale for each image magnification to arrive at the final dimensions. An example thresholded image and a normal image are shown in Figure 64.

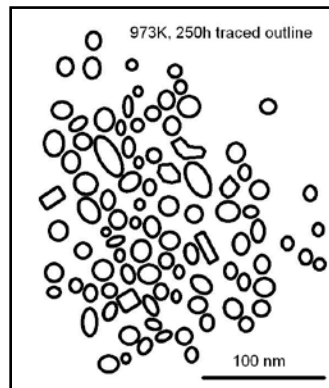
The profiling was done manually using MS Office Suite and elliptical, spherical and rounded rectangular particle shapes were identified and closely fitted to the TEM images. Particles were often found to touch each other. In such cases small nudging of particles was allowed to prevent boundary overlap, which creates problems in ImageJ. The difference in particle counting due to overlap between raw and corrected images for the same set of particles is presented in Figure 65 (a) and (b), respectively. It can be seen that overlap leads to improper thresholding of the image, which in turn, makes the software contour two or more particles together and count them as a single particle. This leads to an incorrect estimate of particle number, and more importantly of area, which is used to arrive at the particle diameter and would give false results on coarsening. While the total count is 95 with an average size of 950 pixel² for the corrected case, the original overlapped image gives a total count of 21 and an average size of 2475 pixel², which is unreasonably high and incorrect.



a: Untreated Image

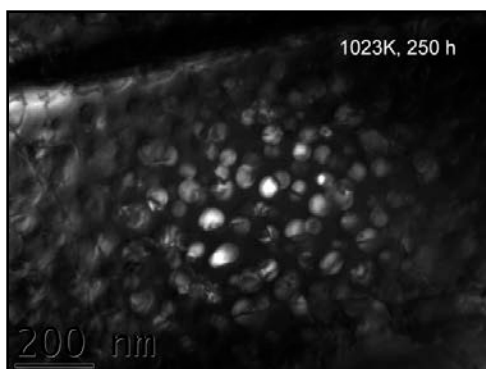


b: Region of Interest Selected

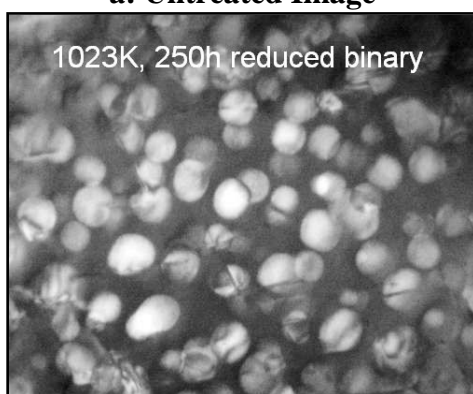


c: Traced Image

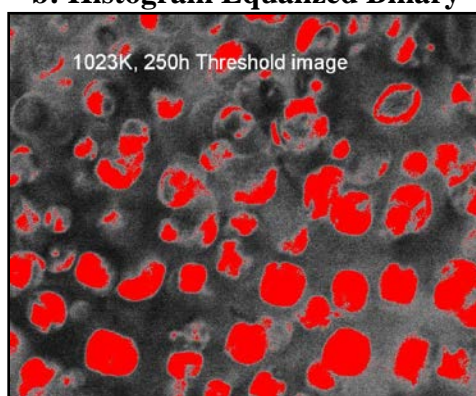
Figure 63: Manual Tracing for γ' Size Measurement



a: Untreated Image



b: Histogram Equalized Binary



c: Maximum Entropy Threshold

Figure 64: Maximum Entropy Thresholding For γ' Size Measurement

Initial activation energy analysis for γ' coarsening was performed on the overlap corrected data using procedures explained earlier based on image analysis of coarsening data and manual measurements. However, since the particles grow very slowly at low temperatures and shorter aging durations, the estimate is subject to manual bias while tracing. Hence for the 5h data used, image analysis was performed to estimate particle size and the rate constant was determined. Even though the particle size following 5 hours of aging is very small, the difference between measured sizes at 5h and longer times is large. Hence, the error is significantly reduced for rate law estimation. The γ' particle size for different aging conditions were measured from TEM micrographs of the kind

shown in Figures 59-61, coupled with the procedures described above (Figures 63-65). The cube of the γ' particle diameter as a function of time is plotted and the slopes are used to determine K. The derived K values are used to plot $\ln(K)$ vs. $1/T$ data as in Figure 66 and a good straight line for the data is obtained, whose slope gives an activation energy value of 327.60 kJ/mole; the latter are compared with literature data in Table 6

The determined activation energy value compares well with those reported for coarsening of γ' in nickel based literature, as well as the value of 303 kJ/mole reported in a recent study on IN718 Plus alloy [78], though the test temperature range is slightly higher. The value is also close to the activation energy for Ni self diffusion (293 kJ/mole) and that of Al in Ni (346 to 373kJ/mole) reported in the literature [79].

It was observed during analysis that the activation energy for coarsening at small particle sizes is high while that for higher temperatures follows LSW kinetics. This is expected and is in line with the C- curve kinetics observed in the TTT diagram for γ' precipitation shown in Figure 67 (from [80]). The kinetics of coarsening of γ' at lower temperatures is slow, and also diminishes at higher temperatures due to thermodynamic instability and start of dissolution. In our measurements, the temperature range is close to the nose of the C-curve, which lays around 1188K (for the experimental curve) and suggests a probable cause explaining the higher activation energy and lower rate constant. Small time and low temperature data is not available for IN718 Plus in literature even though early kinetics at these temperatures, which lie close to the service temperature of this alloys are important for residual stress relaxation.

While there had been earlier reports of volume dependence of Ni_3Ti coarsening kinetics [81] where it was shown that increased volume fraction tends to decrease the coarsening kinetics, it was recently suggested [82] based on simulations that diffusion does not take place across a sharp interface but rather a rough evolving γ - γ' coherent interface in Ni-base alloys. This new approach predicts a square dependence on the time of the particle radius as:

$$\langle r \rangle^2 - \langle r_o \rangle^2 = k_1 t \quad (19)$$

From plots of r^2 vs t , the rate constants K at each temperature were determined, based on which activation energy at small particle sizes was determined for the above model. A good linear fit to the $\ln K$ vs. $1/T$ data, Figure 68, was obtained and the slope yielded an activation energy of 305.274 kJ/mole which is in good agreement with the values reported for γ' coarsening in this alloy as well as others (Table 4.1), validating the goodness of fit analysis and Ardell's proposition that the LSW theory is not applicable for small sizes and the corrected radius square dependence has to be considered.

a: Overlapping



Uncorrected

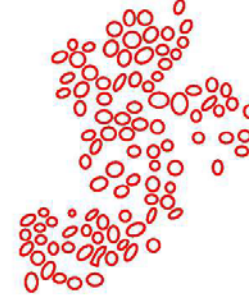
b: Separated



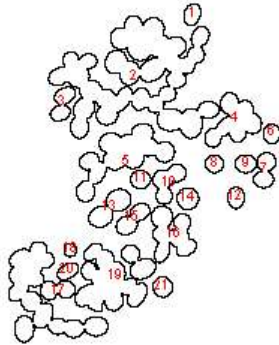
Overlap Corrected



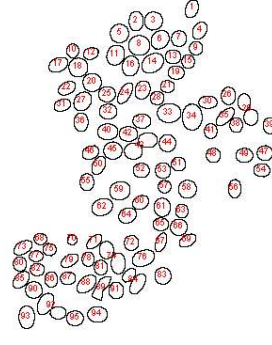
Threshold Applied



Threshold Applied



Poor Particle Count Estimate



Better Particle Count Estimate

Figure 65: Difference in particle counting due to overlap between raw and corrected images for the same set of particles: (a) Overlapped and (b) separated

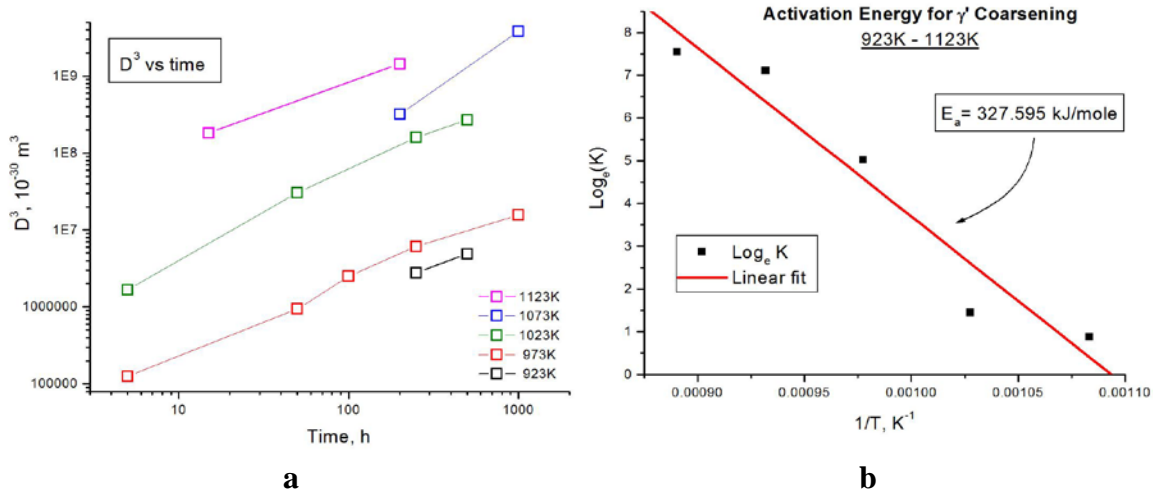


Figure 66: Variation of Cube of Diameter of γ' Precipitates With Aging Temperature and Time and (b) Plot of $\ln K$ Versus $1/T$ for Determining the Activation Energy for Coarsening

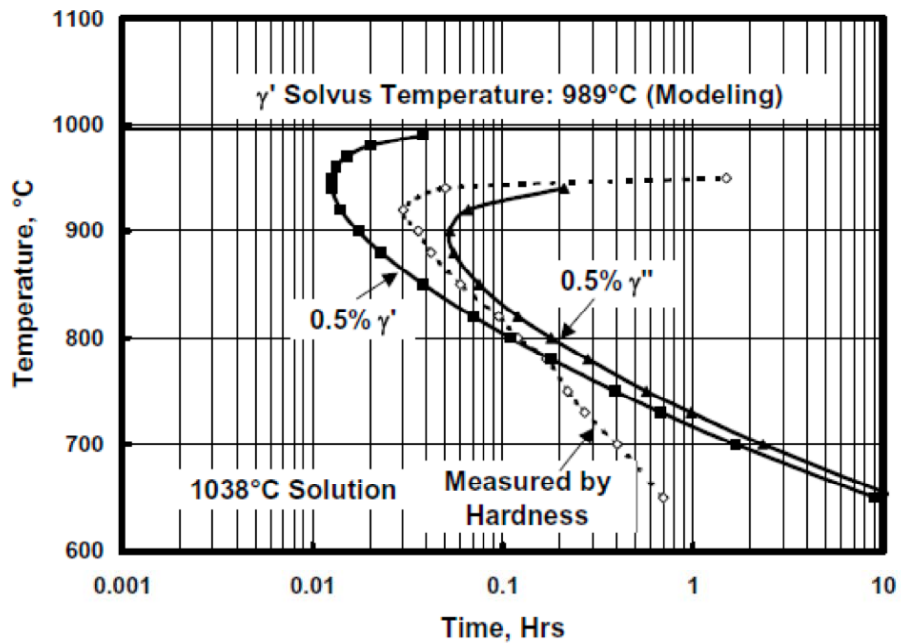


Figure 67: TTT Diagram for γ' Precipitation in IN718 by [75] With Simulated (solid) and Experimental (Dashed) Line

Table 6. Activation energy for γ' coarsening from present study compared with literature [78]

Alloy	Temperature Range [K]	Experimental techniques	Activation energy Q [kJ mol ⁻¹]	Reference
ATI Allvac [®] 718Plus [™]	973-1123	TEM	327.6	[Present study]
ATI Allvac [®] 718Plus [™]	1048-1223	SANS	303	[80]
Ni-13.5 at.% Al	898-1048	TEM	270	[83]
Ni-12.3 at.% Al	943-968	TEM	374 ^a	[84]
Ni-12.5 at.% Al	823-973	XRD	160 ^a	[85]
Alloy PE 16	973-1123	TEM	280	[86]
Alloy PE 16	900-1313	SANS	342	[87]
Alloy PE 16	973-1113	TEM, SANS	339 ^a	[88]
Alloy PE 16	943-1113	TEM	331 ^a	[89]
Alloy 80a	1023-1203	TEM	274.1	[90]
Alloy 80a	973-1123	TEM	392 ^a	[89]
Alloy IN 738	1023-1123	TEM	269	[91]
Alloy IN 738	1023-1223	TEM	269	[92]
Alloy IN 738	1123-1373	TEM	330	[93]
Alloy SC 16	1123-1373	TEM	340	[93]
Alloy 700	1144-1366	TEM	270	[94]
Alloy Mar-M247	1143-1293	TEM	272	[95]
Alloy TM-321	1143-1293	TEM	277	[95]

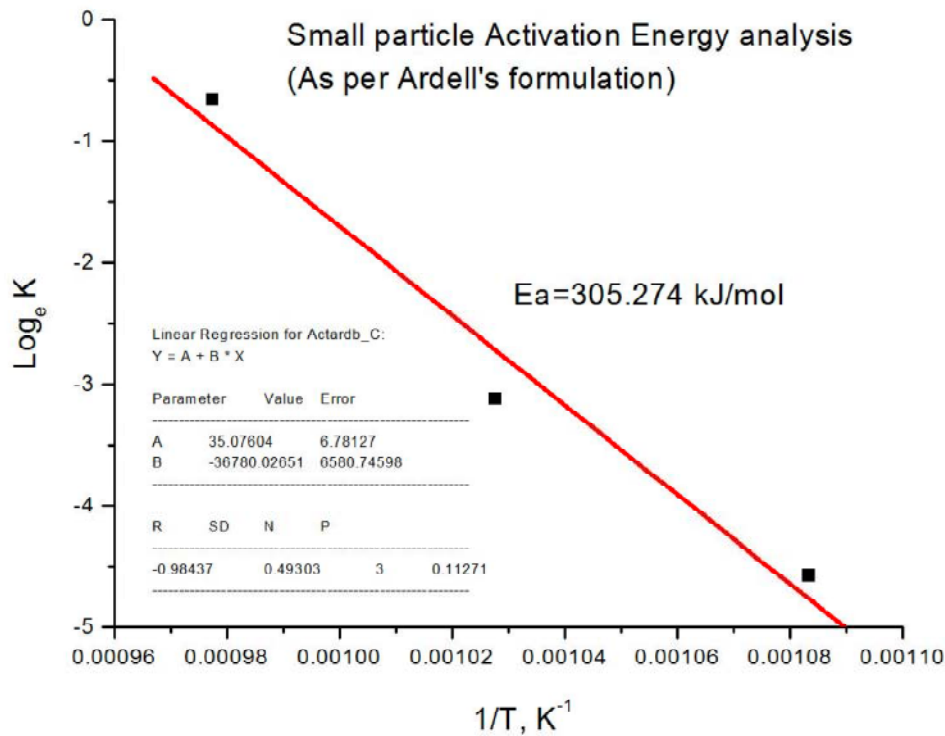


Figure 68: Plot $\ln K$ vs. $1/T$ for Determining Activation Energy for γ' as Per Ardell's [82] Square Law Formulation

3.3.2 LSP Effects on Residual Stress and Thermal Relaxation

LSP is found to introduce lower cold work and deeper compressive residual stress compared with conventional shot peening [2]. Surface residual stress has been reported to relax to less than

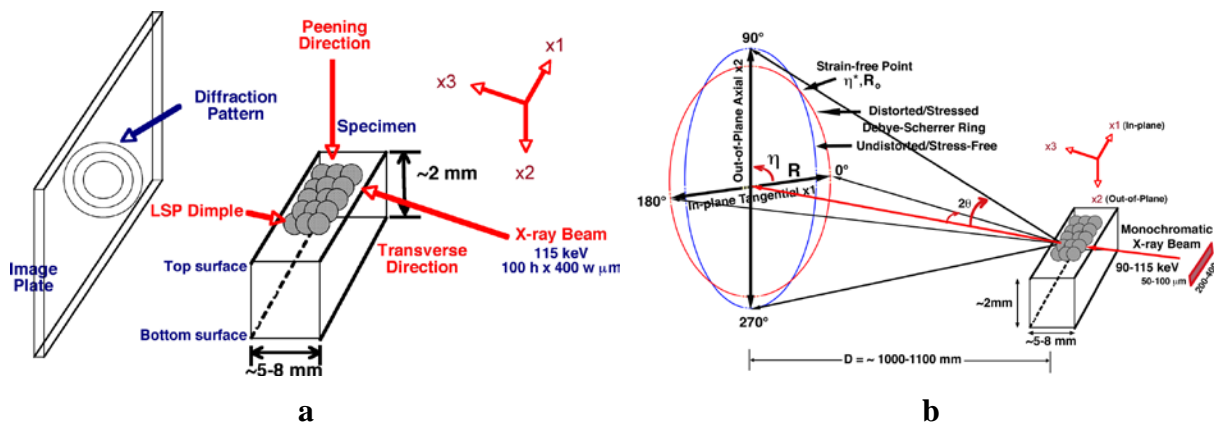


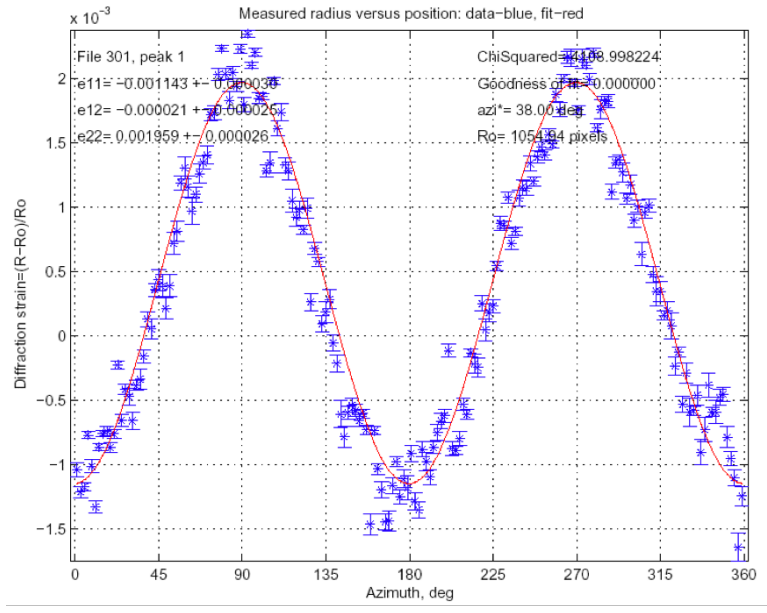
Figure 69: (a) LSP Specimen Dimensions, Geometry and Experimental Setup and (b) Information Relating to Analysis of In-Plane and Out-Of-Plane Strains in the Peened Samples From the Diffraction Pattern

40% of the as-treated value after 1 h heat treatment at 943K for a conventional shot peened alloy, but in our results up to 1 h at 1023K heat treatment, the residual compressive lattice strains in LSP remains about 45% in IN718 Plus alloy based on synchrotron XRD measurements. High energy Synchrotron XRD (SXRD) maps the deeper through thickness compressive residual stresses in the material, without the need for layer removal. The SXRD experimental setup and measurement methodology is discussed below and shown in Figure 69, and residual strain results are presented in Figures 70 and 71. Analysis of angle-resolved x-ray data, especially changes in peak positions, width and shape, provide depth-resolved 3-D structural, strain, stress and cold work information from individual phases in multiphase materials at high spatial resolution. Figure 69 (a,b) shows the SXRD setup. A 115 keV X-ray beam (100 μm high x 400 μm wide on 11-ID-C) was incident on the treated area of a rectangular sample in the transverse direction and the diffraction pattern recorded on an image plate sequentially from the top to the bottom specimen surfaces at 50-100 μm steps. Calibration (CeO₂ standard) and sample data were resolved with data conversion (Fit2D) and fitting the routines (MatLab) of Dr. John Almer and Dr. Uhlrich Leinert at APS, Argonne.

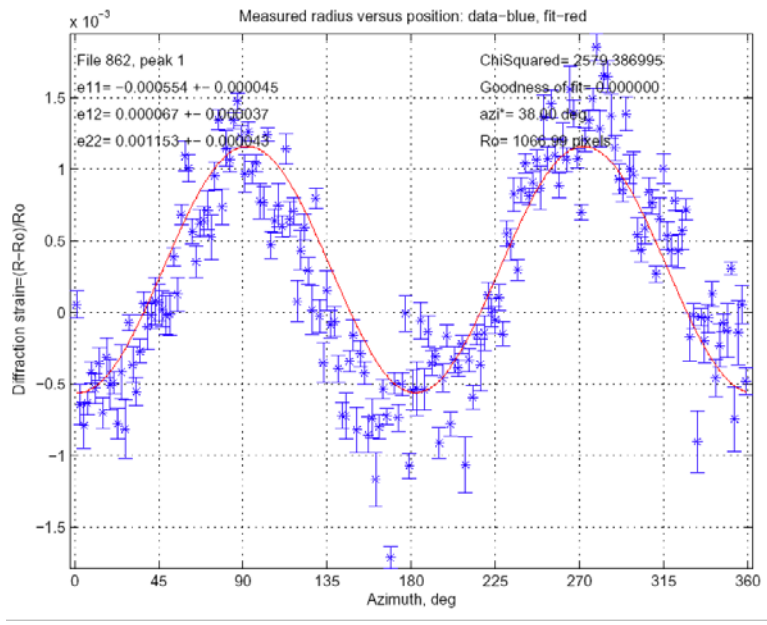
LSP introduces compressive in-plane strains/stresses ($X1$, $X3$ direction) and out-of-plane tensile strains/stresses (in the peening direction $X2$) to some depth in the material, resulting in elliptical diffraction rings: the radii of circular rings shrink (i.e. increase in d) in the out-of-plane peening direction $X2$ (azimuthal angles $h=90^\circ$ and 270°), but expand (i.e. decrease in d) in the in-plane direction $X1$ normal to peening (azimuthal angles $h = 0$ and 180°). Quantifying ring distortion is the basis for diffraction strain measurement and stress by calculation [96]. Examples from an LSP-treated IN718 Plus sample are shown in Figure 70. From the measurements and plots of the radius (and hence the Bragg angle and d-spacing) the in-plane ($0/180^\circ \epsilon_{11}$) and out-of-plane ($90, 270^\circ \epsilon_{22}$) strains are obtained from a pseudo-Voigt fit to the data, and the following equations:

$$\epsilon_\eta = \frac{R_\eta - R_o}{R_o} = \frac{d_\eta - d_o}{d_o}; \quad \epsilon_{11} = \frac{R_{0,180^\circ} - R_o}{R_o} = \frac{d_{0,180^\circ} - d_o}{d_o}; \quad \epsilon_{22} = \frac{R_{90,270^\circ} - R_o}{R_o} = \frac{d_{90,270^\circ} - d_o}{d_o} \quad (20)$$

As can be seen in the plot of diffraction strain versus azimuth, the near-surface region shows compressive (negative at $0^\circ, 180^\circ$) in-plane residuals strains and tensile (positive $90^\circ, 270^\circ$) out-of-plane strains, where as the opposite occurs in the regions farther into the depth from the peened surface.



a



b

Figure 70: Plots of Diffraction Strain Versus Asimuth (a) as LSP-Treated In718 Plus and (b) LSP-Treated + Aged 700°C, 1b/750°C, 1b

The residual stress is then determined by employing the 3-D Hooke's Law assuming equal bi-axial in-plane strains as follows [97]:

$$\sigma_{ij} = \frac{1}{\frac{1}{2}s_2} \left[\varepsilon_{ij} - \delta_{ij} \frac{s_1}{s_2 + 3s_1} (\varepsilon_{11} + \varepsilon_{22} + \varepsilon_{33}) \right] \quad (21)$$

where $\delta_{ij} = \begin{cases} 1 & \text{if } i = j \\ 0 & \text{if } i \neq j \end{cases}$ and

$$s_1^{hkl} = \left(-\frac{\nu}{E} \right)^{hkl} \frac{1}{2} s_2^{hkl} = \left(\frac{1+\nu}{E} \right)^{hkl} \quad (22)$$

The in-plane residual strains as a function of depth from the top to the bottom surfaces are shown in Figure 71. The in-plane strains/stresses are compressive in the near-surface regions to a

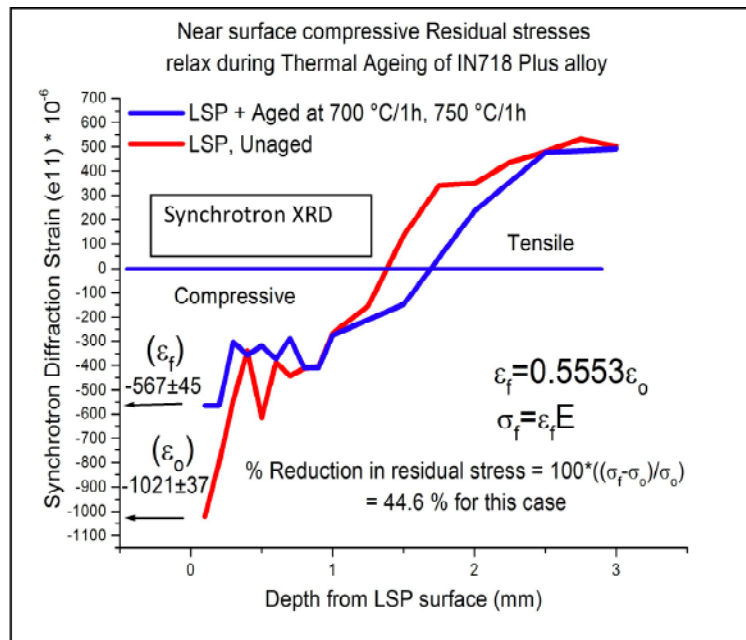


Figure 71: In-Plane Residual Strains as a Function of Distance From the Surface of In718 Plus Alloy (a) As LSP-Treated and (b) LSP-Treated + Aged 700C, 1h/750C, 1h

depth of $\sim 500 \mu\text{m}$, then become tensile further in the depth while diminishing in magnitude. Synchrotron LSP results were generated to estimate the volumetric strain profile for the samples. As can be seen in the SXRD results in Figures 70 and 71, there is a reduction in residual diffraction strain to around 50% of the as-peened value in the sample aged after peening. This is in agreement with data reported in literature where a similar reduction in residual stress is reported within the first hour of higher temperature exposure [2].

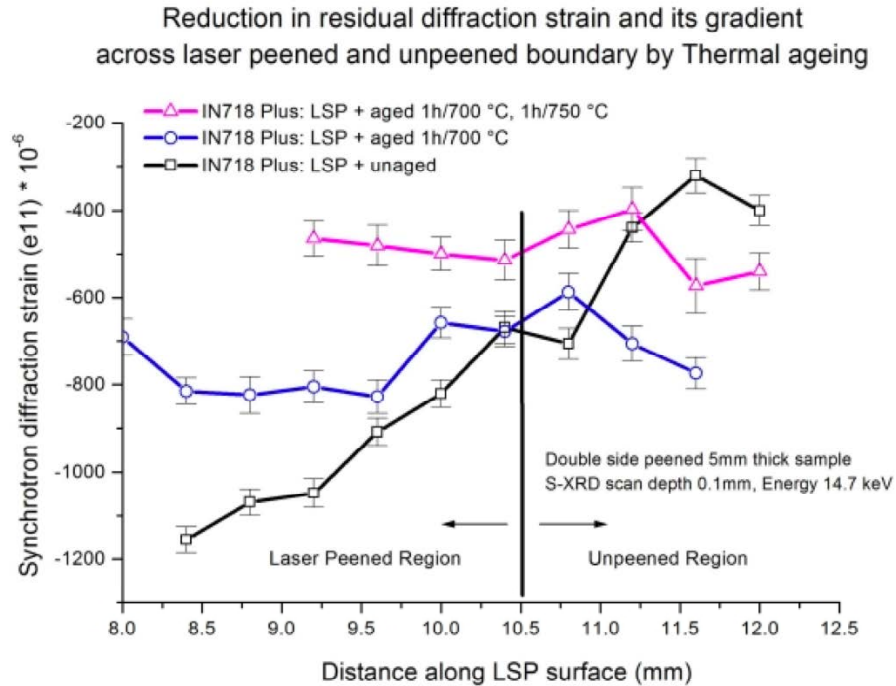


Figure 72: In-Plane Residual Strains as a Function of Distance Across the LSP-Treated Surface of IN718 Plus Alloy Before and After Aging

Figure 72 shows the evolution of the residual stress profile at the edge of the region treated by laser shock. Under the peened condition, the region outside the patch shows strong gradients from compressive towards tensile residual stresses, which is expected from the overall force balance consideration. As the material is progressively aged the compressive residual stresses relax below the shock treated region. The compressive to tensile gradient is also found to decrease. Hence, while thermal treatment relaxes residual compressive stresses in the material, it also decreases the compensating tensile stresses in the region adjacent to the shock boundary. Thus during in-service thermal aging of LSP-treated alloys, a different precipitation tendency should be expected at this interface for coherently strengthened alloys like IN718 Plus.

Industrial LSP practice involves multiple overlap patterns and it is important to be able to determine the effect of different overlap designs on the resultant residual stresses. Figure 73 shows a lateral scan across the sample using SXR to reconstruct the peening scheme of a multiple overlap LSP sample. Residual strains are observed to follow the LSP chronology in the case of multiple overlap samples, and by using 2 directions of beam orientation in SXR, the history of peening can be determined. It also implies that the order in which the dimple overlaps are placed during LSP will result in different residual stress profiles with different locations of local maxima and minima, hence it needs to be looked into before comparing two overlapped samples which may look identical in pattern from visual inspection.

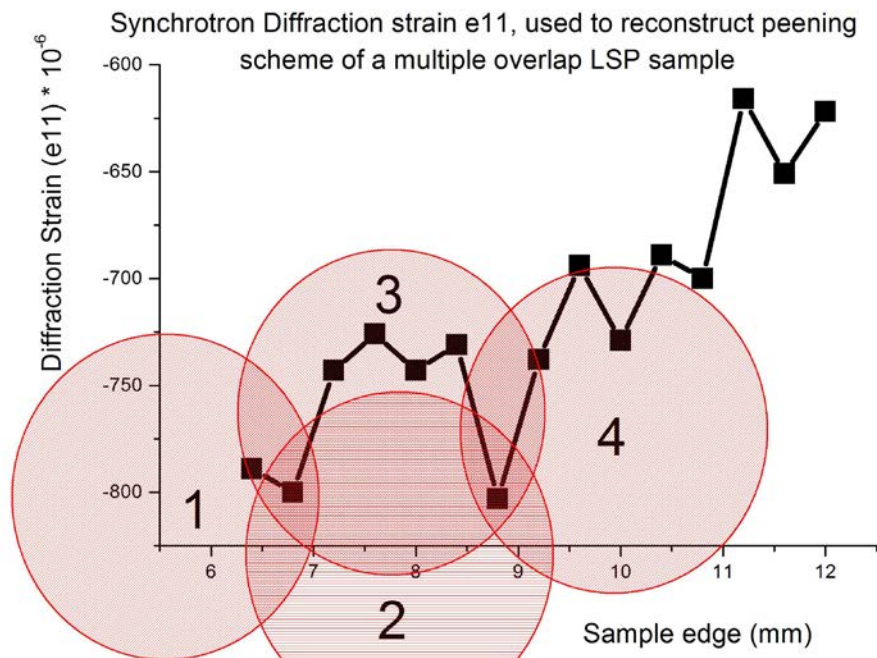


Figure 73: In-Plane Residual Strains as a Function of Distance From the Surface of IN718 Plus Alloy (a) As LSP-Treated and (b) LSP-Treated + AGed 700C, 1b/750C, 1b

Conventional XRD measurements were performed using a dedicated residual stress measurement LXRd by Proto Manufacturing Systems. The LSP coupons were heat treated as per the details given earlier at 973K for 1 and 24 h. Since the LSP treatment and sample size used for these coupons was different from those used in SXRD, the stress values measured are different. To eliminate the effect of variations in measurements due to precipitation behavior, the heat treatment temperature was kept identical in both cases. After the surface measurements, the samples were ground under water flow to uniformly remove material layer from the peened and unpeened surface. After grinding, samples were electrochemically polished in a 10% H_2SO_4 - 90% Methanol solution to remove 30 -100 microns of surface layer to remove the effects of grinding and the XRD measurement was conducted again. This process was incrementally repeated to obtain depth profile for the measurement. The results are given below in Table 7 and Figure 74. Residual stress is found to decrease to around 50% of the original value upon thermal aging, which is in agreement with our SXRD results. Accompanying this change is a drop on the microhardness across the LSP-treated surface from the levels prior to aging and to values close to those in the unpeened area. The sample dimensions and LSP treatment were different in the two cases, suggesting that residual stress relaxation is dependent strongly on temperature and a master curve for residual stress relaxation can be generated based on multiple measurements to arrive at a prediction methodology for engineering structures subject to LSP treatment. Such an approach will need systematic XRD data generation and calibration of the same using independent high accuracy measurements like SXRD, and would be the focus of future research.

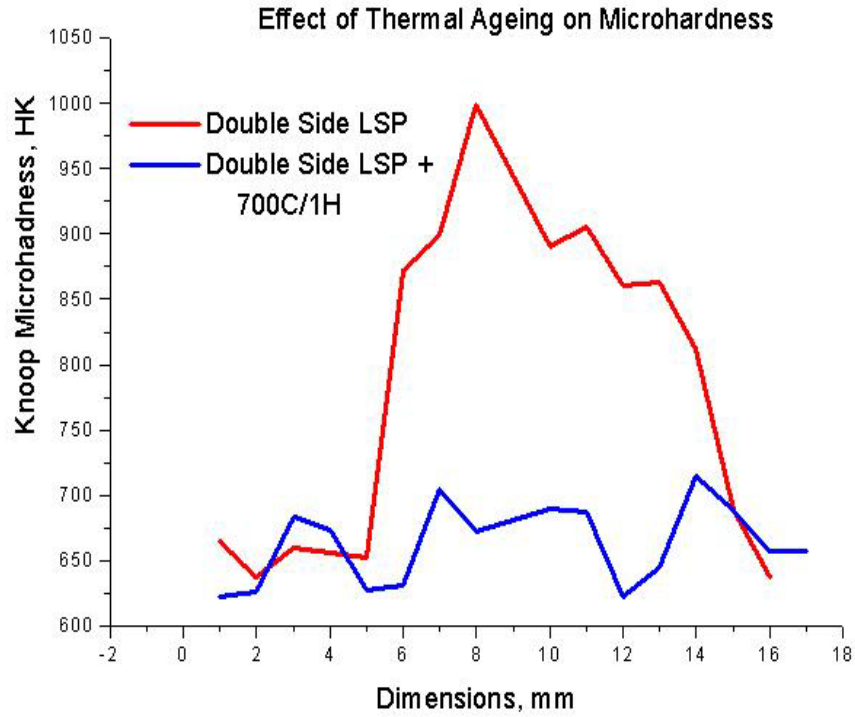


Figure 74: Hardness Across LSP-Treated Surface of IN718 Plus Alloy Before and After Aging

Table 7. Residual Stress Versus Depth in LSP-treated IN718 Plus Before and After Aging

Depth (Microns)	As-LSP-Treated (MPa)	LSP-Treated + 700°C, 1h (MPa)
0 (Surface)	-830	-
50	-633	-433
100	-330	-282
150	-230	-115
300	-50	-
600	-0.55	-

3.3.3 Mechanical Properties of Unpeened Alloy

Tensile tests were carried out on IN718 Plus at room temperature after the age hardening treatment recommended by the manufacturer. The stress-strain curve is presented below (Figure 75) and is found to be in agreement with that reported for this material. Monotonic 3PB compression tests were carried out on IN718 Plus at room temperature prior to 3PB fatigue testing. The stress-strain curve is presented in Figure 76 below. This data was used to estimate percent yield strength values for selecting the loads/stress levels for the 3PB fatigue testing towards the S-N curve determination.

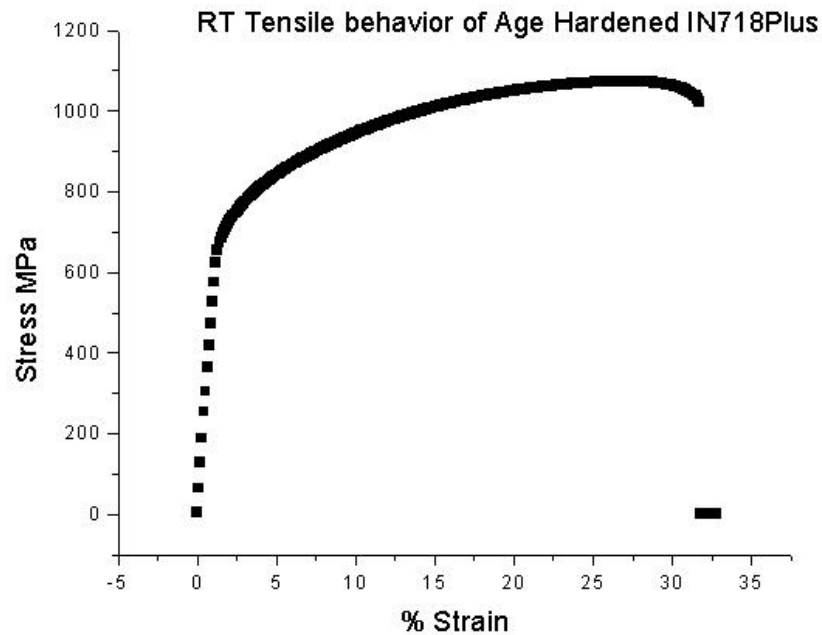


Figure 75: Tensile Stress-Strain Curve for As-Received + Standard Aged IN718 Plus Alloy

The S-N curve for IN718 Plus material in 3PB compression fatigue is presented in Figure 77. The tests were carried out at 30Hz under sine waveform with R=0.1. The curve is plotted with peak stress to correlate with 3PB monotonic compression data reported earlier. The 3PB fatigue tests on the LSP-treated samples gave highly variable results, which could be due to surface roughness, brittle phases or hot spots and additional tests are required to get more reliable data.

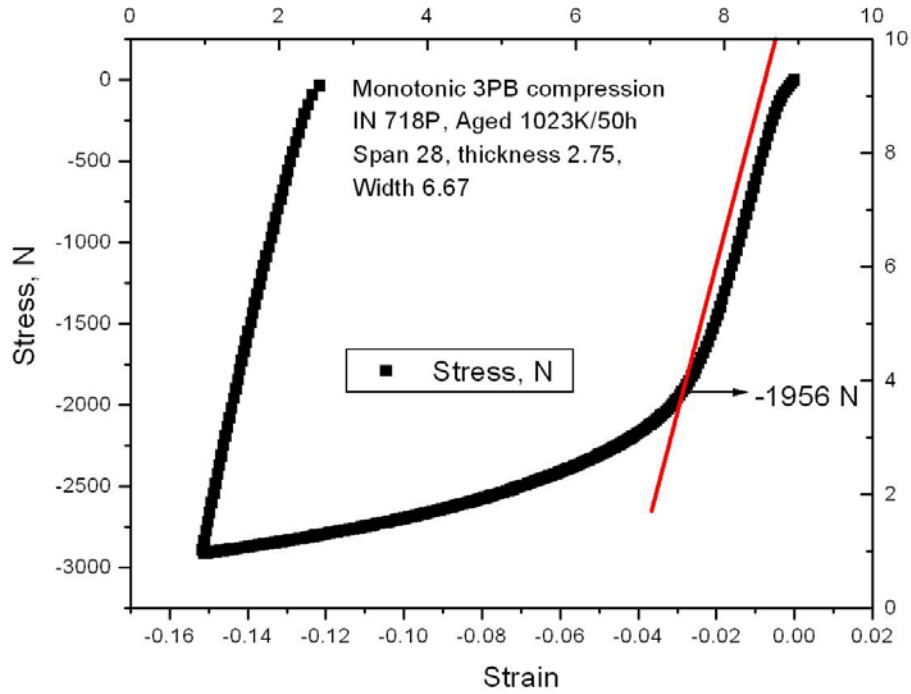


Figure 76: 3PB Compression Stress-Strain Curve for As-Received + Standard Aged IN718 Plus Alloy

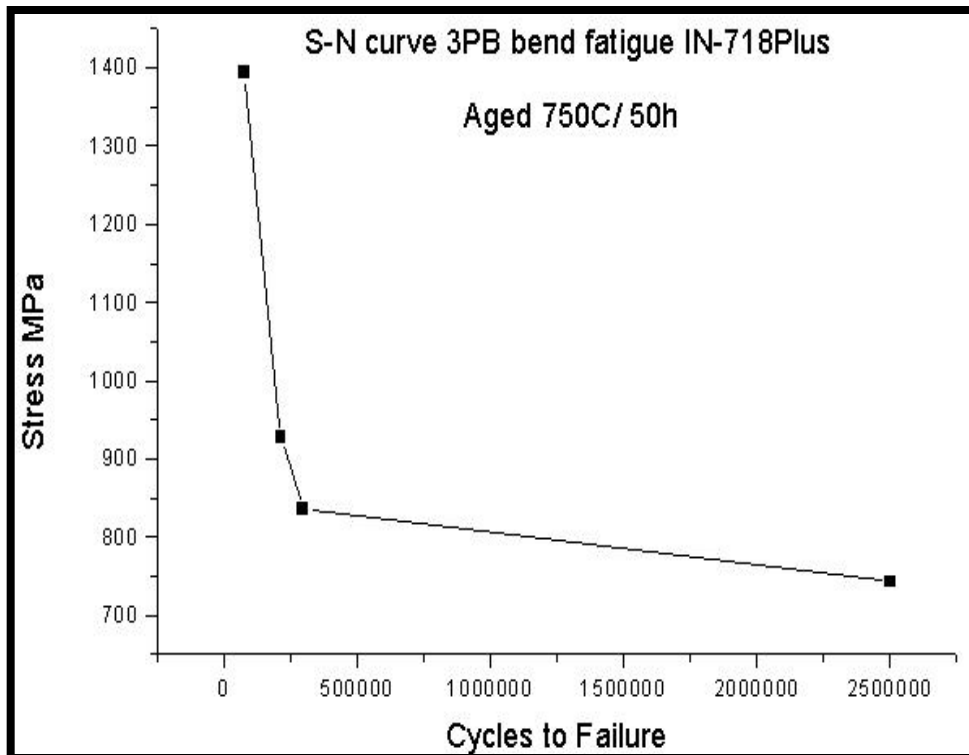


Figure 77: 3PB Fatigue S-N Curve for As-Received + Standard Aged IN718 Plus Alloy

3.3.4 LSP Effects on Fatigue Behavior

3.3.4.1 Fatigue Crack Growth. Fatigue crack growth rate was measured using a lock in amplifier based ACPD system. The SR530 Lock in Amplifier and SIM 983 scaling amplifier based 4 probe-ACPD crack length measurement system with dynamic resolution up to 0.1mm and optical crack length calibration all along with additional elastic compliance calibration for first samples. One side of the sample surfaces was etched prior to fatigue to identify the transgranular mode of failure (Figure 78(a)) while the other was polished to observe crack growth (Figure 78(b)). For ACPD calibration a mean value for both sides of the crack faces was used. A typical long crack composite image is shown in Figure 78(c). Crack closure was measured using a COD gage and corroborated with ACPD.

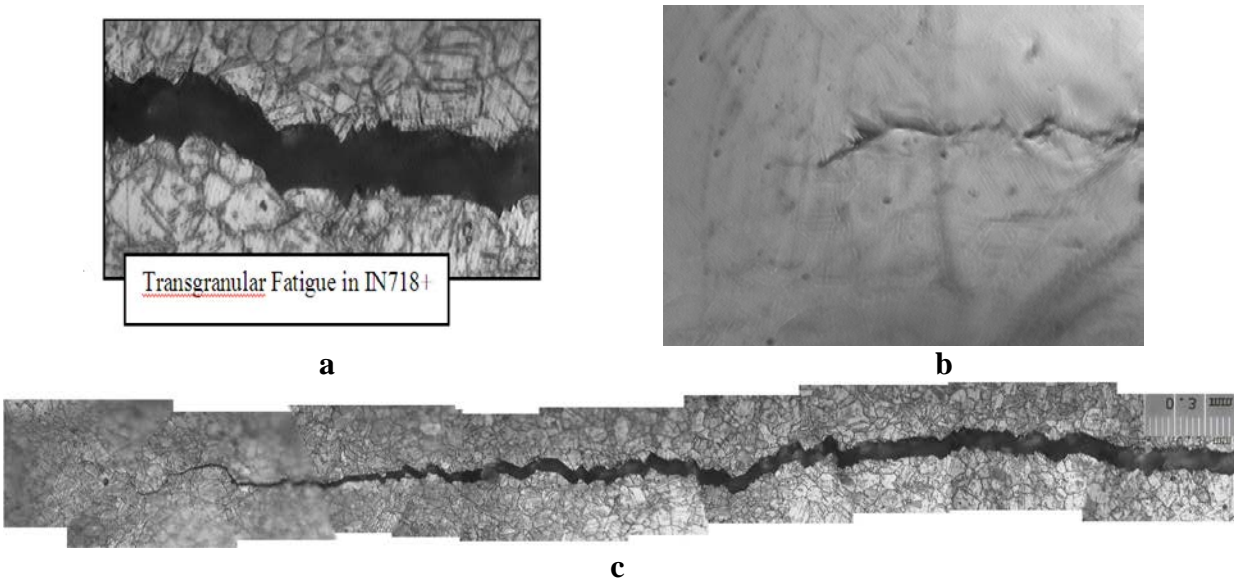


Figure 78: Optical Micrographs of Transgranular Fatigue Crack Growth in IN718 Plus (a) One Surface, (b) Opposite Surface, (c) Montage

After the IN718 Plus material was subjected to double side laser peening with 6J, 25 ns, 2mm spot size Nd-glass laser multiple overlay patch with 50% overlap using adhesive tape overlay and water confinement, the crack was allowed to grow further in the material under fatigue as mentioned below. Upon entering the LSP patch, the crack exhibits a deflection in one direction (Figure 79(a,b)), which indicates it is not due to plane stress effects. This is resolved in Figure 80 from profilometry observations of the crack tip in the LSP treated sample. A Veeco interferometric profilometer with 0.1micron depth resolution is used for profilometry, which indicates the surface topology around the crack tip is inhomogeneous with peaks in one direction and valleys on the other (Figure 80). This suggests the crack tip residual stress field is inhomogeneous and results in the crack deflection observed above when the crack enters the LSP patch.

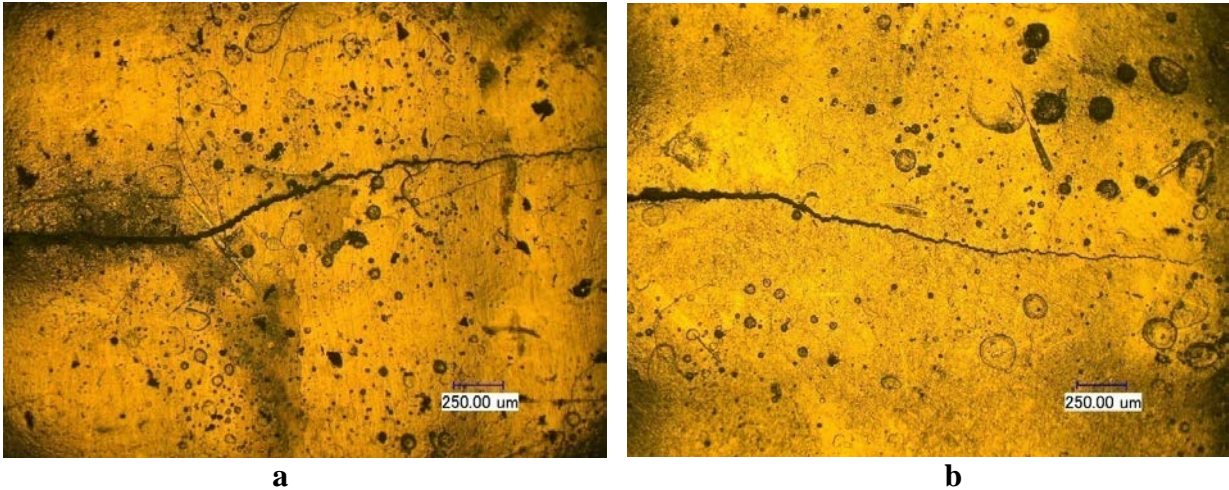


Figure 79: Crack Deflection During Fatigue Crack Growth Upon Entering the LSP-Treated Single Dimple (center) in IN718 Plus (a) Side 1 and (b) Side 2 Surface of Test Coupon

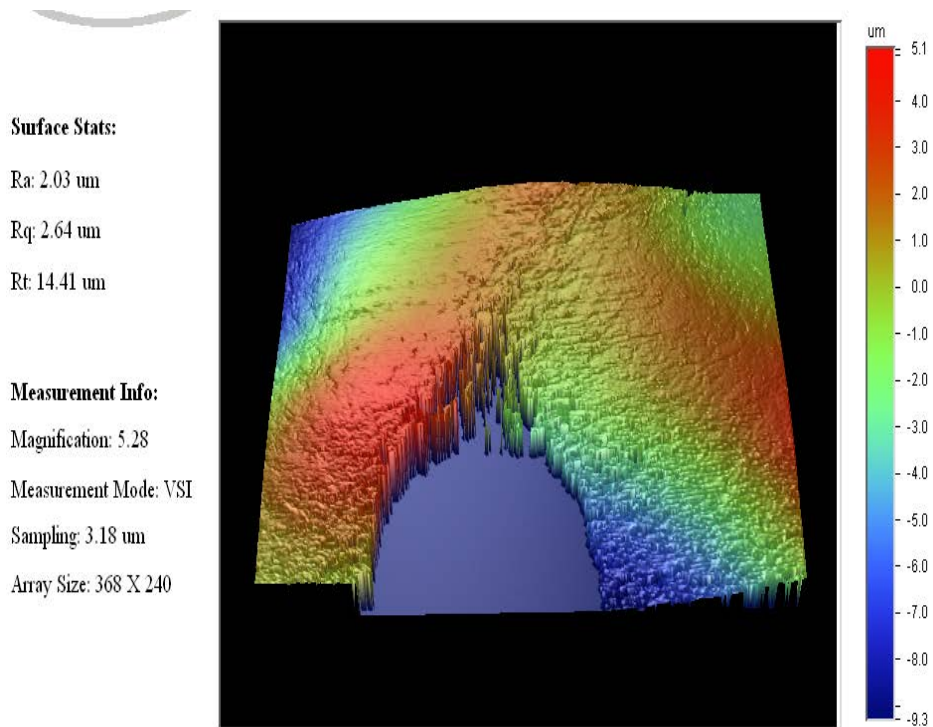


Figure 80: 3-D Profile of Crack Tip in LSP-Treated IN718 Plus

The results of constant amplitude fatigue crack growth tests on the unpeened IN718 Plus material are presented below in Figure 81. Crack opening displacement increase with number of cycles, indicative of progressive damage in agreement with theory, is shown in Figure 81(a). In another sample, the crack length measurement from ACPD data (Figure 81(b)) showed typical accumulating damage with number of cycles more also. Figure 81(c) shows a pre-LSP COD displacement, which appeared to follow elastic behavior without much deviation due to crack closure. Figure 81(d) is the FCG curve da/dN vs ΔK . The curve lies predominantly in the Paris regime.

Constant amplitude FCG tests were also conducted to study the effect of LSP on FCG rates in IN718 Plus. The results are presented in Figure 82. The crack length increase with the number of cycles, indicative of progressive damage in agreement with theory as before, is shown in Figure 82(a). In another sample the crack growth rate measurement from ACPD data (Figure 82(b)) also showed typical accumulating damage with number of cycles. Figure 82(c) shows a post LSP COD displacement, which appeared to follow elastic behavior but with steady increases, indicating increased crack growth rates without much indication of crack closure. Figure 82(d) shows the FCG da/dN vs ΔK curve. The curve lies predominantly in the Paris regime and the slope is compared with non-LSP treated sample and found to be higher in agreement with the crack opening displacement deviations.

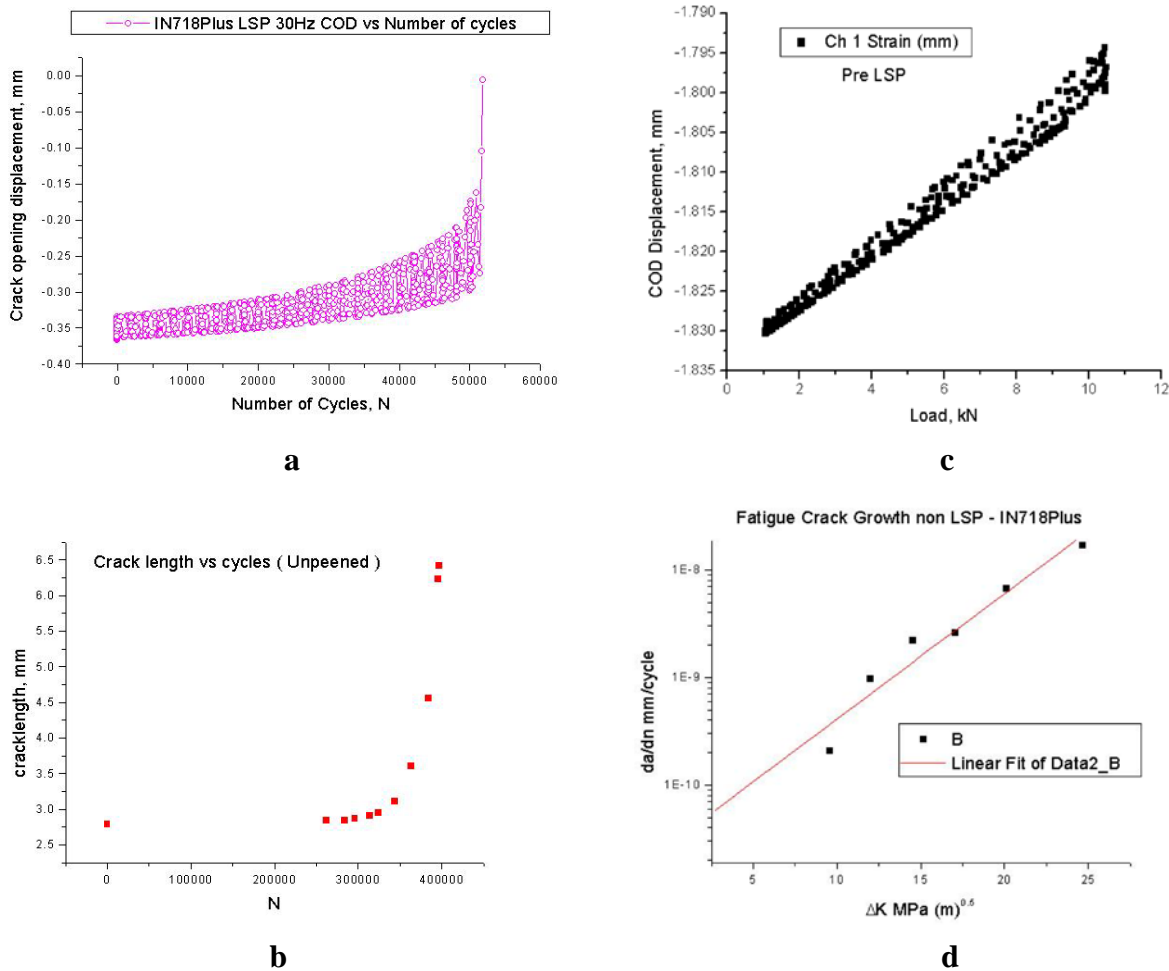


Figure 81: Fatigue Crack Growth Data for Non-LSP-Treated IN718+ Alloy. (a,b) COD Data, (c) Crack Length vs. Number of Cycles From ACPD Measurements and (d) da/dN vs. ΔK Curve From ACOD Data

Fractographic observations were conducted on representative fatigue fractured samples. A transition band is observed close to the peening edge, about 0.6 – 0.7 mm wide as shown in Figure 83(a). Incidence of secondary cracking in the centre of the LSP treated regions could also be seen (Figure 83(b)).

3.3.4.2 Tensile Fatigue S-N Curves and Room and High Temperatures. In addition to the 3PB fatigue and FCG tests, a number of tensile fatigue tests were also conducted on unpeened and LSP-treated IN718 Plus alloy to generated S-N curves at room temperature and at 650°C. The samples for this purpose were ~75 mm (3") long with the

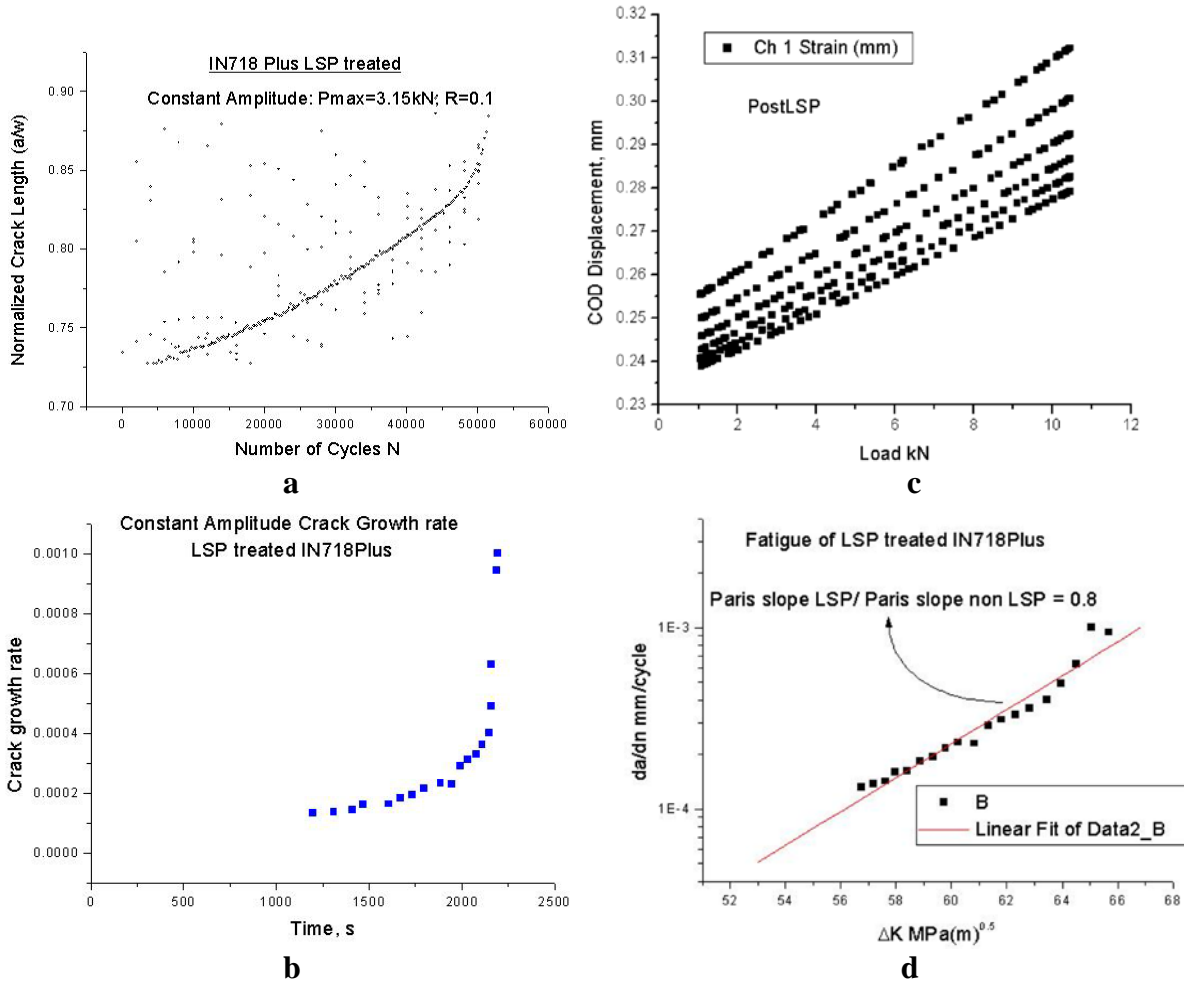
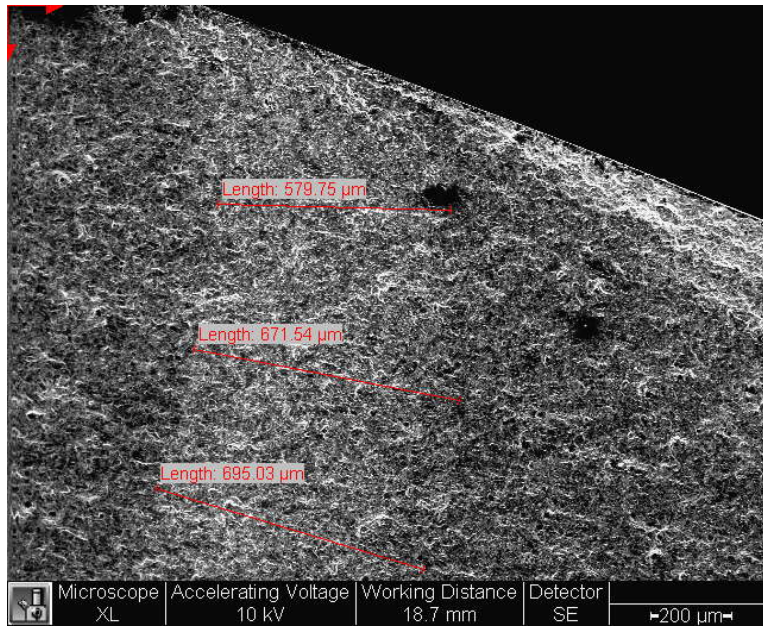
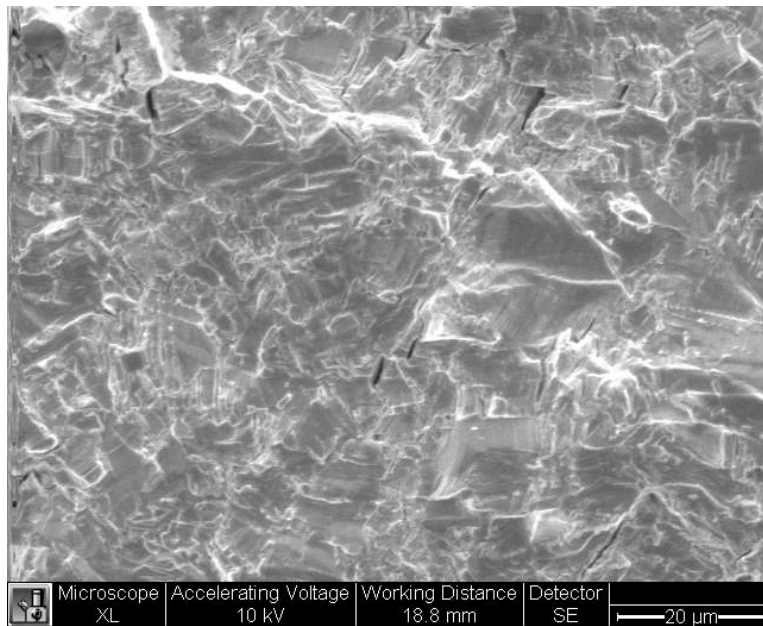


Figure 82: Fatigue Crack Growth Data for LSP-Treated IN718+ Alloy (a,b) Crack Length and Crack Growth Rate vs. Number of Cycles From ACPD Measurements, (c) COD vs. Load and (d) da/dN vs. ΔK Curve From ACPD Data



a



b

Figure 83: (a) Low Magnification and (b) High Magnification SEM Micrographs of Fracture Surface of Failed LSP-Treated FCG Sample. Note Transition Band as the Crack Enters the LSP-Treated Region

dimensions of the gage portion being 25 mm long x 2 mm wide x 2 mm thick. The entire gage section of these samples was LSP-treated simultaneously on both sides with tape using beam energy of 2J and pulse width of 25 ns. XRD measurements revealed a surface compressive residual stress with a magnitude of -150 to -200 MPa. The fatigue tests were conducted under load control at an R-ratio of 0.1 and frequency of 25 Hz.

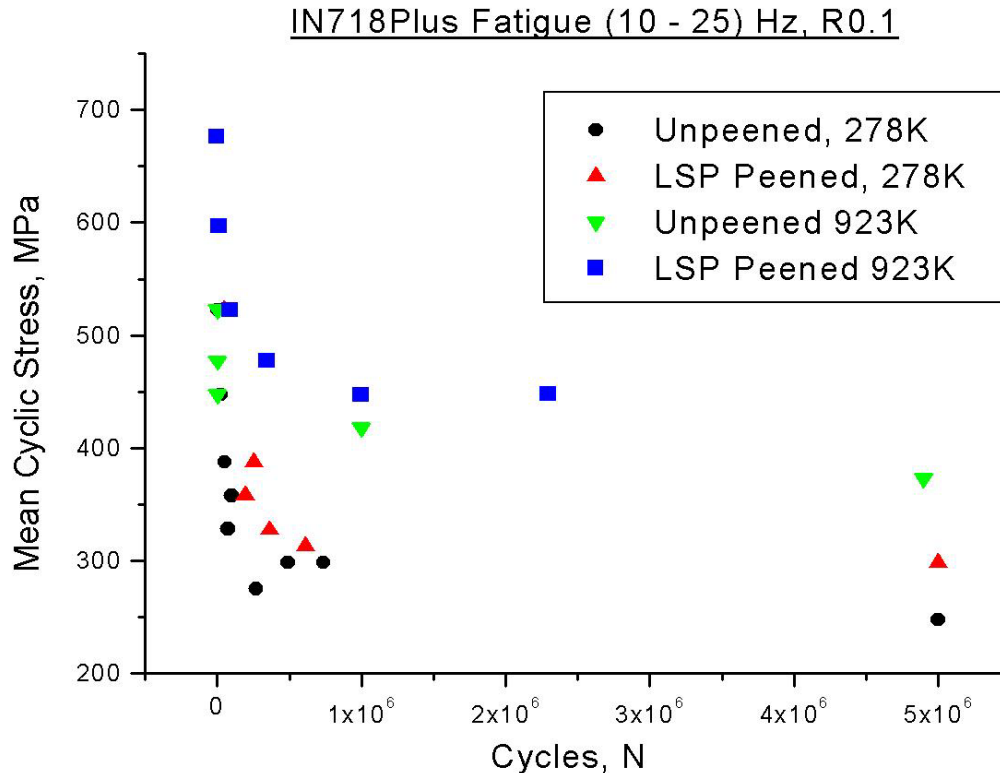


Figure 84: Tensile Fatigue S-N Curve for Unpeened and LSP-Treated IN718 Plus Alloys at Room Temperature and at 650°C

The S-N curves obtained from unpeened and LSP-treated samples at both room temperature (278K) and at 650°C (923K) are shown compared in Figure 84. As can be seen from the data at room temperature, the number of cycles to failure at the same stress are higher in the LSP-treated samples at both low and high stress levels, pointing to the beneficial effect of LSP in improving fatigue life. This improvement amounts to ~10-20% depending on stress level compared with the unpeened material. The results also indicate that the fatigue strength is higher at 650°C in both the unpeened and LSP-treated samples compared with those at room temperature. This feature has been reported before and may be associated with additional age hardening that occurs at the elevated temperature during the tests. In addition, as in the case of the room temperature-tested samples, the LSP-treated samples show higher fatigue lives at equivalent stress levels compared with the untreated samples. This result reveals that the beneficial effects of LSP in improving fatigue life are retained at elevated temperatures also, which is an important finding from the standpoint of extending the use of advanced surface treatments like LSP for improving the performance of structural components operating at high temperatures.

4.0 CONCLUSIONS

The results of this research have led to a number of new findings relating to the effects of LSP on residual stress generation, microstructure evolution, thermal stability and relaxation behavior, modeling aspects, and the fatigue behavior of high-temperature structural alloys, including Ti64, Ti6242, IN718 and IN718 Plus alloys. These are summarized below.

The LSP process parameters for Ti6242, IN718 and IN718 Plus alloys were developed and optimized using finite element simulations. Residual stresses and thermal relaxation thereof at temperatures relevant for each alloy were characterized experimentally using conventional and high energy synchrotron x-ray diffraction. Residual stresses were also modeled and simulated using three-dimensional nonlinear finite element method using LS-DYNA. From the FE analysis of residual stress evolution and relaxation at elevated temperatures, the following conclusions can be drawn.

- A new set of Johnson-Cook material model parameters for IN718 [98] and IN718 SPF [99] alloys was proposed based on comparison with experimentally measured residual stresses following LSP, and the numerical simulation of LSP-induced residual stress was found to be in good agreement with the experimental results.
- For IN718 with initial residual stress lower than 400 MPa, nearly no thermal relaxation takes place at temperatures lower than 700°C. At higher temperatures, the maximum relaxation occurs at the depth of maximum compressive residual stress, and a significant decrease of the residual stress is observed during the initial exposure period (between 1 min and 3 min in this study), followed by a stabilization of the stress relaxation at longer exposure times [98].
- The thermal relaxation amplitude increases with the increase in temperature, and the effect of temperature is more significant at longer exposure times. The Zener–Wert–Avrami function was adopted to describe the thermal residual stress relaxation, and the associated parameters for laser shock peened IN718 were determined [98] as $m=0.77$, $\Delta H = 3.45 \text{ eV}$ and $B = 2.18 \times 10^{12} \text{ min}^{-1}$.
- The magnitude of thermal relaxation depends on the degree of plastic deformation developed during the LSP process. It was found the larger the initial plastic strain, the greater the stress relaxation.
- Single shot LSP treatments and experimental measurements of residual stress in IN718 SPF alloy were used to successfully calibrate the Johnson-Cook parameters for finite element simulations of LSP-induced residual stress. Good agreement between experimental and simulation results was obtained with these parameters for both single dimple and overlapped dimple samples [99].
- The thermal relaxation of residual stress over the 550-650°C temperature range in IN718 SPF alloy was characterized experimentally and by finite element simulations for both single dimple and overlapped dimple samples. Good agreement was obtained between the experimental and simulation results. A Zener-Wert-Avrami analysis of the kinetics of relaxation of residual stress yielded an activation enthalpy ΔH of around 270 kJ/mole, which is close to the values for volume diffusion of Al and Ti in Ni-base alloys. These results suggest that the residual stress relaxation is caused by a creep-like mechanism involving rearrangement and annihilation of dislocations by climb [99].

Based on a 3-D nonlinear finite element method framework, laser shock peening induced residual stress in Titanium-base alloys (Ti-6Al-4V and Ti-6Al-2Sn-4Zr-2Mo), and the associated thermal relaxation behavior of residual stress due to short-term exposure at elevated temperatures, were investigated [100,101]. A nonlinear constitutive model in the form of Johnson-Cook was developed by validating against both high strain rate and thermal relaxation experiments. Based on the FE analysis of thermal relaxation, the following conclusions can be made.

- The magnitude of thermal relaxation is influenced by the combined effects of the test temperature and the order of magnitude of the LSP-induced residual stress. Maximal relaxation occurs at the depth of maximum compressive residual stress, and lower initial stress is subjected to less stress relaxation. Residual stress distribution becomes more uniform after thermal relaxation. Stress relaxation mainly occurs during the initial exposure period (between 10 min to 20 min in this work).
- An analytical model based on the Zener–Wert–Avrami formalism has been developed to describe the thermal relaxation of residual stress. The activation enthalpy of the relaxation process in LSP-treated Ti-6Al-4V is calculated as $\Delta H = 1.47$ eV [100], which is close to the values reported for other titanium alloys.
- Good agreement between the experimental and simulation results of thermal relaxation of residual stress between 316 to 538°C (600-1000°F) was obtained for Ti-6Al-2Sn-4Zr-2Mo LSP-treated overlap samples [101]. A Zener-Wert-Avrami kinetic analysis of the experimental residual stress data yielded an activation enthalpy ΔH of ~ 114 kJ/mole, which is close to the values reported for self-diffusion of Ti in Ti-base alloys. These results suggest that the residual stress relaxation in the LSP-treated Ti6242 alloy is caused by a creep-like mechanism involving rearrangement and annihilation of dislocations by climb [101].
- The proposed modeling methodology for thermal relaxation analysis can be further applied to other high-temperature materials, giving a fundamental understanding of thermal stability of residuals stress and hence better prediction of service life.

Finite element simulations were used to study the effects of sequencing of the LSP spots on residual stress distributions [102] and effects on the fatigue behavior [103] in the Ti6242 alloy. Based on these results, coupons were LSP-treated and the fatigue behavior studied in three-point bending. The following conclusions were made.

- The FE simulations were successfully used for optimizing the LSP process parameters for obtaining through thickness compressive residual stresses in the Ti6242 alloy coupons [102].
- Three-point bend fatigue tests on coupons LSP-treated with the optimized parameters revealed that LSP leads to a marked improvement in the high cycle fatigue life of the Ti6242 alloy at room temperature. The results also indicated that even after aging at relatively high temperatures the LSP-treated specimens seemed to retain the fatigue life enhancement over unpeened specimens, thus demonstrating the thermal stability of fatigue life [103].
- Fatigue crack growth rates were assessed based on measurement of striation spacings in SEM images of the fracture surface of failed specimens. The results indicated that the crack growth

rates at a given stress intensity range were much lower in the LSP-treated samples compared with the unpeened samples, pointing to the beneficial effects of LSP. This enhancement of fatigue life following LSP was still retained at elevated temperatures, even above the expected service temperatures for the Ti6242 alloy [103].

LSP effects on residual stress generation, near-surface microstructure, thermal stability of both and on the fatigue behavior in IN718 Plus Ni-base superalloy were studied. The results led to following findings.

- Kinetics of precipitation and coarsening of γ' precipitates in IN718 Plus alloy were studied over the temperature range of 650K – 850°C [104]. γ' coarsening was found to follow LSW kinetics in general. The average activation energy for coarsening was found to be 327.6 kJ/mol, which is close to the value of 303 kJ/mol for IN718 Plus reported previously using SANS measurements [78] and to those for volume diffusion of Al and Ti in Ni-base alloys.
- Coarsening of γ' precipitates in IN718 Plus alloy at low temperatures was observed to deviate from LSW kinetics and follow a radius square dependence proposed by Ardell and O.Vidvuds [82] with an activation energy of 303 kJ/mole [104].
- Plate-shaped η -Ni₃Ti (hexagonal, DO₂₄ structure) precipitates were identified in both as-received and aged samples through experimental and computer-simulated electron diffraction patterns and convergent beam electron diffraction.
- The γ' precipitates above a certain size were observed to transform to η -Ni₃Ti through a faulting mechanism.
- Rapid relaxation of the LSP-induced residual stress takes place within 1 h of heat treatment of the sample to about half the original value at temperatures of 700 and 750°C in agreement with previous reports. Despite the relaxation, depth profile of the stress field is retained to a good extent and the residual stresses are present in materials to original depth but at reduced values. Also stress gradients observed across the shocked treated region boundary are reduced with thermal aging [105].
- LSP is observed to lead to a reduction in the fatigue crack growth rates. The results are, however, subject to variation, and seem to be highly dependent on the peening pattern and sequence, specimen geometry, edge effects, consistency in laser energy, and surface conditions. Further combined FE simulation and experimental work is required to optimize the LSP parameters for adequate levels of compressive residual stress and improved fatigue life [106].
- LSP is found to lead to a 10-20% improvement in fatigue life over unpeened material, depending on the stress level. This improvement is particularly seen in the high cycle regime [106].
- The beneficial effects of LSP in improving fatigue life are retained at elevated temperatures also, which is an important finding from the standpoint of extending the use of advanced surface treatments such as LSP for improving the performance of structural components operating at high temperatures [106].

5.0 REFERENCES

1. W. Zhuang and B. Wicks, "Mechanical Surface Treatment Technologies for Gas Turbine Engines," *J. Engr Gas Turbines & Power*, **125**, 1021-1025 (2003).
2. A. H. Clauer and D. F. Lahrman, "Laser Shock Processing as a Surface Enhancement Process," *Key Engr. Mater.*, **197**, 121-144 (2001).
3. C. S. Montross, T. Wei, L. Ye, G. Clark and Y-W. Mai, "Laser Shock Processing and Its Effects on Microstructure and Properties of Metal Alloys: A Review," *Int. J. of Fatigue*, **24**, 1021-1036 (2002).
4. P. Peyre and R. Fabbro, "Laser Shock Processing: a Review of the Physics and Applications," *Optical & Quantum Electronics*, **27**, 1213-1229 (1995).
5. P. S. Prevey, "Burnishing Method and Apparatus for Providing a Layer of Compressive Residual Stress in the Surface of a Workpiece," *U. S. Patent*, **No. 5,826,453** (1998).
6. P. S. Prevey, M. J. Shepard and P. R. Smith, "The Effect of Low Plasticity Burnishing (LPB) on the HCF Performance and FOD Resistance of Ti-6Al-4V," in *Procs. 6th International National Turbine Engine High Cycle Fatigue (HCF) Conference, Jacksonville, FL, March (2001)*.
7. P. S. Prevey, E. F. Loftus and D. J. Hornbach, "Application of Low Plasticity Burnishing (LPB) to Improve the Fatigue Performance of Ti-6Al-4V Femoral Hip Stems," *J. ASTM Internl*, **3(5)**, May (2006).
8. B. P. Fairhand, A. H. Clauer, R. G. Jung and B. A. Wilcox, "Quantitative Assessment of Laser-Induced Stress Waves Generated at Confined Surfaces," *Appl. Phys. Lett.*, **25**, 431-433 (1974).
9. B. P. Fairhand and A. H. Clauer, "Use of Laser Generated Shocks to Improve the Properties of Metals and Alloys," *Industrial Applications of High Power Laser Technology*, **86**, 112-119 (1976).
10. B. P. Fairhand, A. H. Clauer and B. A. Wilcox, "Pulsed Laser Induced Deformation in an Fe-3 Wt Pct Si Alloy," *Metall. Trans.*, **8A**, 119-125 (1977).
11. B. P. Fairhand, A. H. Clauer and B. A. Wilcox, "Laser Shock Hardening of Weld Zones in Aluminum Alloys," *Metall. Trans.*, **8A**, 1871-1876 (1977).
12. A. H. Clauer, in: *Surface Performance of Titanium*, J. K. Gregory, H. J. Rack and D. Eylon (eds.), TMS, Warrendale, PA pp. 217-230 (1996).
13. J. J. Ruschau, R. John, S. R. Thompson and T. Nicholas, "Fatigue Crack Nucleation and Growth Rate Behavior of Laser Shock Peened Titanium," *Int. J. of Fatigue*, **21**, S199-S209 (1999).
14. R. K. Nalla, I. Altenberger, U. Noster, G. Y. Liu, B. Scholtes and R. O. Ritchie, "On the Influence of Mechanical Surface Treatments—Deep Rolling and Laser-Shock Peening—on the Fatigue Behavior of Ti-6Al-4V at Ambient and Elevated Temperatures," *Mater. Sci. Engng.*, **A355**, 216-230 (2003).
15. I. Altenberger, E. A. Stach, G. Liu, R. K. Nalla and R. O. Ritchie, "An In Situ Transmission Electron Microscope Study of the Thermal Stability of Near-Surface Microstructures Induced by Deep Rolling and Laser-Shock Peening," *Scripta Mater.*, **48**, 1593-1598 (2003).
16. C. Rubi-Gonzalez *et al.*, "Effect of Laser Shock Processing on Fatigue Crack Growth and

- Fracture Toughness of 6061-T6 Aluminum Alloy,” *Mater. Sci. Engrg.*, **A386**, 291-295 (2004).
17. S.R. Mannava and T. J. Rockstroh, “Fourth Generation of Laser Shock Peening to Enhance Damage Tolerance of Aircraft Engine Components,” Invited Lecture, ASME/JSME PVP Conference, Laser Peening Session and Panel Discussions (2004); S. R. Mannava, *Private communication*, University of Cincinnati, Cincinnati, OH, April (2005).
 18. J. N. Johnson and R. W. Rhode, “Dynamic Deformation Twinning in Shock Loaded Iron,” *J. Appl. Phys.*, **42**, 4171-4182 (1971).
 19. Y. Sano, M. Kimura, N. Mukai, M. Yoda, M. Obata and T. Ogisu, *in: High Power Lasers in Manufacturing*, Proc. SPIE, **3888**, 294-306 (2000).
 20. K. Okazaki, A. Ito, Y. Sano, N. Mukai, N. Aoke, C. Konagai and M. Kikunaga, *U. S. Patent, No. 5,790,620*, August 4 (1998).
 21. P. S. Prevey, “X-ray Diffraction Residual Stress Techniques,” Company Pamphlet, Lambda Research, Cincinnati, OH (1986).
 22. I. C. Noyan and J. B. Cohen, “Residual Stress: Measurement by Diffraction and Interpretation,” Springer-Verlag, New York, pp. 120-126 (1987).
 23. V. Hauk, “Structural and Residual Stress Analysis by Nondestructive Methods,” Elsevier, Amsterdam, pp. 139-152 (1997).
 24. P. Prevey, D. Hornbach and P. Mason, “Thermal Induced Stress Relaxation and Distortion in Surface Enhanced Gas Turbine Engine Components,” *in: Procs. of the 17th Heat Treating Society Conference and Exposition and the 1st Induction Heat Treating Symposium*, D. L. Milam et al. (eds.), ASM, Materials Park, OH, pp. 3-12 (1998).
 25. P. Prevey, “The Effect of Cold Work on the Thermal Stability of Residual Compression in Surface Enhanced IN 718,” *in: Procs. of the 20th ASM Materials Solutions Conference and Exposition*, ASM, Materials Park, OH, pp. 1-9 (2000).
 26. R.C. McClung, “A literature survey on the stability and significance of residual stresses during fatigue,” *Fatigue & Fracture Of Engineering Materials & Structures*, **30**, 173-205 (2007).
 27. H. Holzappel, V. Schulze, O. Vohringer and
 28. E. Macherauch, “Residual stress relaxation in an AISI 4140 steel due to quasistatic and cyclic loading at higher temperatures,” *Mater. Sci. Engrg.*, **A248**, 9-18 (1998).
 29. H. Lee and S. Mall, “Stress relaxation behavior of shot-peened Ti-6Al-4V under fretting fatigue at elevated temperature,” *Mater. Sci. Engrg.*, **A366**, 412-420 (2004).
 30. W. Cao, M. Khadhraoui, B. Brenier, J.Y. Guedou and L. Castex, “Thermomechanical relaxation of residual-stress in shot peened nickel-base superalloy,” *Materials Science And Technology*, **10**, 947-954 (1994).
 31. O. Vohringer, T. Hirsch and E. Macherauch, “Relaxation of shot peening induced residual stresses of Ti6Al4V by annealing or mechanical treatment,” *in: Proceedings of the 5th International Conference on Titanium*, Munich, FRG, pp. 2203-2210 (1984).
 32. M. Khadhraoui, W. Cao, L. Castex and J.Y. Guedou, “Experimental investigations and modelling of relaxation behaviour of shot peening residual stresses at high temperature for nickel base superalloys,” *Materials Science And Technology*, **13**, 360-367 (1997).

33. N. Masmoudi, L. Castex and A. Bertoli, "Influence of temperature and time on the stress relaxation process of shot peened IN100 superalloys," *Materiaux et Techniques (Paris)*, **77**, 29-36 (1989).
34. A. Evans, S.B. Kim, J. Shackleton, G. Bruno, M. Preuss and P.J. Withers, "Relaxation of residual stress in shot peened Udimet 720Li under high temperature isothermal fatigue," *International Journal Of Fatigue*, **27**, 1530-1534 (2005).
35. B.X. Feng, X.N. Mao, G.J. Yang, L.L. Yu and X.D.Wu, "Residual stress field and thermal relaxation behavior of shot-peened TC4-DT titanium alloy," *Mater. Sci. Engr.*, **A512**, 105-108 (2009).
36. D.J. Buchanan, R. John, R.A. Brockman and A.H. Rosenberger, "A coupled creep plasticity model for residual stress relaxation of a shot peened nickel-base superalloy," in: *Superalloys 2008*, 965-974 (2008).
37. A.B. Aghdam, T.N. Chakherlou and K. Saeedi, "An FE analysis for assessing the effect of short-term exposure to elevated temperature on residual stresses around cold expanded fastener holes in aluminum alloy 7075-T6," *Materials & Design*, **31**, 500-507 (2010).
38. D.J. Buchanan, R. John and R.A. Brockman, "Relaxation of shot-peened residual stresses under creep loading," *Journal of Engineering Materials and Technology*, **131**, 031008 (2009).
39. Z. Zhou, A.S. Gill, D. Qian, S.R. Mannava, K. Langer, Y. Wen and V.K. Vasudevan, "A finite element study of thermal relaxation of residual stress in laser shock peened IN718 superalloy," *International Journal of Impact Engineering*, **38**, 590-596 (2011).
40. D. Lohe and O. Vohringer, "Thermal Stability of Residual Stress," in: *Handbook of Residual Stress and Deformation in Steel*, G. Totten, M. Howes and T. Inoue (eds.), ASM International, Materials Park, OH pp. 54-69 (2002).
41. M. E. Fine, *Introduction of Phase Transformations in Condensed Systems*, Macmillan, New York (1965).
42. J. Hoffmeister, V. Schulze, and R. Hessert, "Thermal Relaxation Of Residual Stresses Induced By Shot Peening In IN718," *Conference Proceedings of ICSP10*, Tokyo, Japan (2008).
43. I. Kaur, and W. Gust, *Handbook of grain and interphase boundary diffusion data*, Ziegler Press Stuttgart, Germany (1989).
44. W. Braisted and R. Brockman, "Finite element simulation of laser shock peening," *International Journal of Fatigue*, **21**, 719-724 (1999).
45. K. Ding and L. Ye, "Three-dimensional dynamic finite element analysis of multiple laser shock peening processes," *Surface Engineering*, **19**, 351-358 (2003).
46. K. Ding and L. Ye, "FEM simulation of two sided laser shock peening of thin sections of Ti-6Al-4V alloy," *Surface Engineering*, **19**, 127-133 (2003).
47. Y. Hu, Z. Yao and J. Hu, "3-D FEM simulation of laser shock processing," *Surface & Coatings Technology*, **201**, 1426-1435 (2006).
48. P. Peyre, I. Chaieb and C. Braham, "EM calculation of residual stresses induced by laser shock processing in stainless steels," *Modelling and Simulation in Materials Science and Engineering*, **15**, 205-221 (2007).

49. A.W. Warren, Y.B. Guo and S.C. Chen, "Massive parallel laser shock peening: Simulation, analysis, and validation," *International Journal of Fatigue*, **30**, 188-197 (2008).
50. R. Fabbro, J. Fournier, P. Ballard, D. Devaux and J. Virmont, "Physical study of laser-produced plasma in confined geometry," *Journal of Applied Physics*, **68**, 775-784 (1990).
51. G.R. Johnson and W.H. Cook, "A constitutive model and data for metals subjected to large strains, high strain rates and high temperatures," in: *7th International Symposium on Ballistics*, The Hague, The Netherlands, pp. 541-547 (1983).
52. D.R. Lesuer, "Experimental investigations of material models for Ti-6Al-4V titanium and 2024-T3 aluminum," in: *D.o. Transportation* (Ed.), 2000.
53. F.J. Zerilli and R.W. Armstrong, "Dislocation-mechanics-based constitutive relations for material dynamics calculations," *Journal of Applied Physics*, **61** (1987) 1816-1825.
54. F.J. Zerilli, "Dislocation mechanics-based constitutive equations," *Metall. Mater. Trans.*, **35A**, 2547-2555 (2004).
55. H.W. Meyer, "A modified Zerilli-Armstrong constitutive model describing the strength and localizing behavior of Ti-6Al-4V," in: *Army Research Laboratory Report* (Ed.), 2006.
56. A.S. Khan, Y.S. Suh and R. Kazmi, "Quasi-static and dynamic loading responses and constitutive modeling of titanium alloys," *International Journal of Plasticity*, **20**, 2233-2248 (2004).
57. P.S. Follansbee and G.T. Gray, "An analysis of the low-temperature, low and high strain-rate deformation of Ti-6Al-4V," *Metall. Trans.*, **20**, 863-874 (1989).
58. H.W. Meyer and D.S. Kleponis, "Modeling the high strain rate behavior of titanium undergoing ballistic impact and penetration," *International Journal of Impact Engineering*, **26**, 509-521 (2001).
59. N. Ahmed, A.V. Mitrofanov, V.I. Babitsky and V.V. Silberschmidt, "Analysis of material response to ultrasonic vibration loading in turning Inconel 718," *Mater. Sci. Engrg.*, **A424**, 318-325 (2006).
60. A. Thomas, A. El-Wahabi, J.M. Cabrera and J.M. Prado, "High temperature deformation of Inconel 718," *Journal of Materials Processing Technology*, **177**, 469-472 (2006).
61. [H. Yuan and W.C. Liu, "Effect of the delta phase on the hot deformation behavior of Inconel 718," *Mater. Sci. Engrg.*, **408**, 281-289 (2005).
62. P. Juijerm and I. Altenberger, "Effect of temperature on cyclic deformation behavior and residual stress relaxation of deep rolled under-aged aluminium alloy AA6110," *Mater. Sci. Engrg.*, **A452**, 475-482 (2007).
63. D.Y. Cai, P.L. Nie, J.P. Shan, W.C. Liu, Y.K. Gao and M. Yao, "Precipitation and residual stress relaxation kinetics in shot-peened Inconel 718," *Journal of Materials Engineering And Performance*, **15**, 614-617 (2006).
64. M.-C. Berger and J.K. Gregory, "Residual stress relaxation in shot peened Timetal 21S," *Mater. Sci. Engrg.*, **A263**, 200-204 (1999) 200-204.
65. A.F.M Arif, "Numerical prediction of plastic deformation and residual stresses induced by laser shock processing," *Journal of Materials Processing Technology*, **136**(1-3), 120-138 (2003)

66. C. Yang et al., "Geometrical effects on residual stresses in 7050-T7451 aluminum alloy rods subject to laser shock peening," *Journal of Materials Processing Technology*, **201**(1-3), 303-309 (2008).
67. *ABAQUS Analysis User's Manual*. 2005: ABAQUS, Inc. Pawtucket.
68. G. Singh, G., R. Grandhi and D. Stargel, "Modified particle swarm optimization for a multimodal mixed-variable laser peening process," *Structural and Multidisciplinary Optimization*, **42**(5), 769-782 (2010).
69. Y. Hu and Z. Yao, "Overlapping rate effect on laser shock processing of 1045 steel by small spots with Nd:YAG pulsed laser," *Surface and Coatings Technology*, **202**(8), 1517-1525 (2008).
70. P. S. Follansbee and U.F. Kocks, "A Constitutive Description Of The Deformation Of Copper Based On The Use Of The Mechanical Threshold Stress As An Internal State Variable," *Acta Metallurgica*, **36**(1), 81-93 (1988).
71. A. S. Khan, A.S., Y.S. Suh and R. Kazmi, "Quasi-static and dynamic loading responses and constitutive modeling of titanium alloys," *International Journal of Plasticity*, **20**(12), 2233-2248 (2004).
72. H. K. Amarchinta et al., "Simulation of residual stress induced by a laser peening process through inverse optimization of material models," *Journal of Materials Processing Technology*, **210**(14), 1997-2006 (2010).
73. D. J. Steinberg, S.G. Cochran, and M.W. Guinan, "A constitutive model for metals applicable at high-strain rate," *Journal of Applied Physics*, **51**(3), 1498-1504 (1979).
74. M. Boustie and F. Cottet, "Experimental And Numerical Study Of Laser-Induced Spallation Into Aluminum And Copper Targets," *Journal of Applied Physics*, **69**(11), 7533-7538 (1991).
75. W. D. Cao and R. L. Kennedy, "Recommendations for heat treating Allvac 718Plus alloy parts," *Allvac Technical Report* (2006).
76. B. H. Kear, J. M. Oblak and A. F. Giamie A, *Metall. & Met. Trans.*, **1B**, 2477-86 (1970)
77. J. De Ja Ponte, *Proc. Of SPIE, Intl. Soc. Optical Engng.*, 6575, (2007).
78. G. A. Zickler, R. Schnitzer, R. Radis, R. Hochfellner, R. Schweins, M Stockinger and H. Leitner, *Materials Science and Engineering*, **A523**(1-2), 295-303 (2009)
79. J. Cermak, A. Gazda and V. Rothova, *Intermetallics*, **11**, 939-946 (2003).
80. W. D. Cao, in: *Superalloys 718, 625, 706 and their derivatives* Ed. E. A. Loria, TMS (2005)
81. D. M. Kim and A. J. Ardell, *Scripta Mater.* **43**, 381-384 (2000)
82. A. J. Ardell and O. Vidvuds, *Nature Materials*, **4**, 309-316 (2005).
83. A. J. Ardell and R. B. Nicholson, *Acta Metall.* **14**, pp. 1295-1309, (1966)
84. T. Hirata and D. H. Kirkwood, *Acta Metall.* **25**, 1425-1434 (1977).
85. C. Marsh C. and H. Chen, *Acta Metall. Mater.* **38**, 2287-2298, (1990).

86. K. B. S. Rao, V. Seetharaman, S. L. Mannan and P. Rodriguez, *Mater. Sci. Eng.* **58**, 93–106, (1983).
87. K. Ali, S. Messoloras and R. J. Stewart, *J. Phys. F. Met. Phys.* **15**, 487–505 (1985).
88. H. P. Degischer, W. Hein, H. Strecker, W. Wagner and R. P. Wahi, *Z. Metallkd.* **78**, 237–249, (1987).
89. B. Reppich and G. Schumann, *Mater. Sci. Eng. A* **101**, 171–182, (1988).
90. P. K. Footner and B. P. Richards, *J. Mater. Sci.* **17**, 2141–2153, (1982).
91. R. A. Stevens R.A. and P. E. J. Flewitt, *Mater. Sci. Eng.* **37**, 237–247 (1979).
92. P. J. Henderson and M. McLean, *Acta Metall.* **31**, 1203–1219 (1983).
93. T. Malow, J. Zhu and R. P. Wahi, *Z. Metallkd.* **85**, 9–19 (1994).
94. E. H. van der Molen, J. M. Oblak and O. H. Kriege, *Metall. Trans.* **2**, 1627–1633 (1971).
95. H. T. Kim, S. S. Chun, X. X. Yao, Y. Fang and J. Choi, *J. Mater. Sci.* **32**, 4917–4923 (1997).
96. J. Almer, U. Lienert, R. L. Peng, C. Schlauer and M. Oden, *J. Appl. Phys.*, **94**, 697-702 (2003).
97. V. Hauk, *Structural and Residual Stress Analysis by Nondestructive Methods*, Elsevier, NY (1997).
98. Z. Zhou, A. S. Gill, D. Qian, S. R. Mannava, K. Langer, Y. Wen and V.K. Vasudevan, “A Finite Element Study of Thermal Relaxation of Residual Stress in Laser Shock Peened IN718 Superalloy,” *International Journal of Impact Engineering*, **38**, pp. 590-596 (2011).
99. A. S. Gill, Z. Zhou, A. Telang, S.R. Mannava, K. Langer, D. Qian and V. K. Vasudevan, “Thermal Relaxation of Residual Stress in Laser Shock Peened IN718 SPF Superalloy: Experiments and Finite Element Modeling,” *Acta Materialia*, to be submitted (2012).
100. Z. Zhou, S. Bhamare, G. Ramakrishnan, S. R. Mannava, K. Langer, D. Qian and V.K. Vasudevan, “A Study of Thermal Relaxation of Residual Stress in Laser Shock Peened Ti6Al-4V Alloy by 3D Nonlinear Finite Element Method,” *Surfaces & Coatings*, submitted (2011).
101. G. Ramakrishnan, S. Bhamare, Z. Zhou, J. Guenes, S. R. Mannava, K. Langer, D. Qian and V.K. Vasudevan, “Thermal Relaxation of Residual Stress in Ti-6Al-2Sn-4Zr-2Mo Alloy: Experiments and Finite Element Modeling,” *Modeling and Simulation in Materials Science and Engineering*, In Preparation for Submission (2012).
102. S. Bhamare, G. Ramakrishnan, S. R. Mannava, K. Langer, D. Qian and V.K. Vasudevan, “Finite Element Simulations for Optimization of Laser Shock Peening Parameters for Ti-6Al-2Sn-4Zr-2Mo Alloy,” *Computational Materials Science and Engineering*, In Preparation for Submission (2012).
103. G. Ramakrishnan, S. Bhamare, S. R. Mannava, K. Langer, D. Qian and V.K. Vasudevan, “Fatigue Behavior of Laser Shock Peened Ti-6Al-2Sn-4Zr-2Mo Alloy,” *International Journal of Fatigue*, In Preparation for Submission (2012).

104. V. Chaswal, S. R. Mannava, D. Qian, K. F. Langer and V. K. Vasudevan "Precipitation Behavior During Aging in IN718 Plus Alloy," *Acta Mater*, In Preparation for Submission (2012).
105. V. Chaswal, S. R. Mannava, D. Qian, K. F. Langer and V. K. Vasudevan "Thermal Relaxation of Residual Stress in Laser Shock Peened IN718 Plus Alloy," *Scripta Mater*, In Preparation for Submission (2012).
106. V. Chaswal, S. R. Mannava, D. Qian, K. F. Langer and V. K. Vasudevan "Effects of Laser Shock Peening on Fatigue Behavior of IN718 Plus Alloy," *Acta Mater*, In Preparation for Submission (2012).